CHAPTER 3

Density, irregularity, and instability

Chapter Outline

Cross-Scale Coupling and Energy Transfer in the Magnetosphere-Ionosphere-Thermosphere System
https://doi.org/10.1016/B978-0-12-821366-7.00001-9

3.1 High-latitude F-region plasma irregularities

Gareth W. Perry[a] *and Lindsay V. Goodwin*[a,b]

[a]Center for Solar-Terrestrial Research, New Jersey Institute of Technology, Newark, NJ, United States
[b]Cooperative Programs for the Advancement of Earth System Science, University Corporation for Atmospheric Research, Boulder, CO, United States

3.1.1 Introduction

Some of the most striking evidence of the complex, cross-scale interactions and interconnections present and underway in the terrestrial magnetosphere-ionosphere-thermosphere (M-I-T) system can be found at high latitudes. The region is home to density irregularities, auroral dynamics, and extremely fast plasma flows that set it apart from any other geomagnetic regions in terms of scale size and intensity. In the high-latitude ionosphere, the geomagnetic field lines are nearly vertical, with a magnetic dip angle $I \gtrsim 80$ degrees. Furthermore, the magnetic topology can be either "open" or "closed" (although the former is more likely), that is, the magnetic field lines are either connected to the interplanetary magnetic field (IMF)—"open" field lines, or they are connected to the opposite geomagnetic pole, located in the opposite hemisphere—"closed" field lines.

The first radio instruments used to study the ionosphere in detail were ionosondes. Also known as a "vertical sounder," an ionosonde provides a vertical plasma density profile of the bottomside ionosphere up to the altitude, *hmF*2, of the ionosphere's critical frequency, *foF*2. This is accomplished by increasing the ionosonde's operating frequency in successively transmitted pulses. The pulses are reflected from the altitude where the ionosphere's plasma frequency matches the frequency of the transmitted ionosonde pulse; higher frequencies continue to propagate vertically. A vertical profile of the ionosphere's plasma density below *hmF*2, a region commonly referred to as the "bottomside" ionosphere, can be deduced from the reflected transmissions. The ionosonde technique cannot measure the "topside" ionosphere, above *hmF*2, where the plasma density decreases with increasing altitude. This is because the ionosonde pulses that would have been reflected in the topside cannot reach those altitudes as they would have been already reflected (back to the ground) in the bottomside.

The high-latitude ionosphere's extreme variability in terms of ionospheric plasma density and dynamics was readily apparent early in the history of the studyed region. Ionosonde measurements of the region were peculiar; they frequently showed vertical plasma density profile traces with ionospheric peak densities at altitudes that were several factors higher than what was normally expected for the F region. The traces were also dynamic; they were seen to quickly descend before settling to an altitude that was more

consistent with an F-region profile. It was quickly realized that, in fact, an anomalously high altitude F-region ionosphere was not responsible for the signature. Rather, "ionized clouds," localized enhancements in ionospheric plasma density, traveling horizontally at 300–400 m/s were responsible for the curious traces (Meek, 1949). In general, ionosondes transmit toward the local zenith. But, like all radio systems, their transmitted power also leaks in all directions, albeit at a lower intensity, which is how the clouds were detected. The apparent vertical movement of the plasma profile was a manifestation of clouds' horizontal motion with respect to the ionosonde.

These ionosonde measurements gave the first glimpse of the highly dynamic and variable high-latitude ionosphere, and among the first reports of a phenomenon that would come to be known as a "polar cap patch" (see also Section 2.3). In this chapter, we will pay particularly close attention to this phenomenon as it has garnered a great deal of attention in the decades since it was first detected. We will also examine its counterpart, the plasma density depletion, sometimes referred to as a "trough" or "hole."

Before we proceed any further, we would like to point out that the terms "patch," "trough," "hole," etc. are colloquial. For a more meticulous treatment and description of these phenomena, we will avoid using such terminology. It is our hope that our colleagues will follow suit in the future. The first term, "patch" is operationally defined by Crowley (1996) as a plasma density enhancement of a magnitude that is at least twice that of the background ionosphere, with a scale size that is of the order of 100 km, i.e., a mesoscale density structure. However, this definition is several decades old and is awkward because (1) it requires one to define the "background" plasma density, which is variable in space and time on both short-term and long-term scales in the high-latitude region, (2) it is arbitrary and excludes enhancements slightly less dense than twice the background, and (3) it is too general and does not reflect the diversity of plasma density enhancement generators present at high latitudes. In the light of new measurements and analysis of the high-latitude ionosphere that have taken place since its inception, it should be revisited, if not discontinued altogether. We do not want to develop or propagate terminology that may become redundant or ambiguous in the long term. Accordingly, we choose to classify the aforementioned phenomena simply as "plasma density irregularities," or "irregularities" for brevity.

3.1.1.1 The continuity equation

Even during the winter, when the region is completely devoid of photoionization, the high-latitude F region is swarming with plasma density irregularities of a variety of scale sizes. The irregularities include density enhancements with magnitudes that are close to that of the lower-latitude dayside ionosphere. How can this be if the main source of ionization, solar EUV flux, is absent, and even if another source of ionization, particle precipitation, is also absent? Such unique conditions are what set the high-latitude

ionosphere apart from other geographic regions. As it turns out, the irregularities are a byproduct of complex and multiscale M-I-T coupling processes. To gain better insight into the sources and sinks of these irregularities, let us first consider the continuity equation.

The continuity equation is expressed as (Schunk and Nagy, 2000):

$$\frac{\partial n_i}{\partial t} + n_i \nabla \cdot \vec{v}_i + \vec{v}_i \cdot \nabla n_i = P_i - L_i, \tag{3.1}$$

where n_i is the plasma density, v_i is the ion plasma flow, P_i is the production term, and L_i is the loss term. While irregularities spread over a wide-scale range between 100 km and <1 m (the kinetic scale), we pay particular attention to Eq. (3.1) at spatial scales $\lambda > 10$ km and temporal scales $60 \leq t \leq 3600$ s. These scales are largely determined and limited by our ability to measure and study polar F-region phenomena.

Let us first deal with the second term on the left-hand side of Eq. (3.1). In the polar F region, plasma flows at the convection velocity, $\vec{v}_i = (\vec{E} \times \vec{B})/B^2$, in which $\vec{E}$ is the electric field and $\vec{B}$ is the local magnetic field. Thus, according to Rishbeth and Hanson,

$$\nabla \cdot \vec{v}_i = \nabla \cdot (\vec{E} \times \vec{B}), \tag{3.2}$$

which, after some algebraic manipulations, can be rewritten as

$$\nabla \cdot \vec{v}_i = \frac{\vec{B} \cdot (\nabla \times \vec{E}) - \vec{E} \cdot (\nabla \times \vec{B})}{B^2} + \vec{E} \times \vec{B} \cdot \nabla \frac{1}{B^2}. \tag{3.3}$$

The first two terms are zero because $\nabla \times \vec{E} = \nabla \times (-\nabla \phi) = 0$, where ϕ is an electric potential, and the F region is nearly void of strong electric currents. Furthermore, at the scales we are interested in, gradients in the magnetic field are considered to be negligible. Therefore, the F-region plasma is considered to be incompressible; $n_i \nabla \cdot \vec{v}_i \simeq 0$ (Rishbeth and Hanson, 1974).

F-region plasma production is dominated by the ionization of O via solar photons or collisions with energetic particles. However, we will consider Eq. (3.1) in the case of the F-region polar ionosphere during winter. Here we can assume that $n_i \simeq [O^+]$ (square brackets denote concentration), and $P_i \simeq 0$ (or the equivalent scenario in which protoproduction is balanced by chemical recombination). For the moment, we are also assuming that plasma production by precipitation, a second-order effect, is also negligible.

Plasma loss, L_i, is governed by chemistry, i.e., the chemical recombination of O^+, and diffusion. The two rate determining reactions in the depletion of O^+ are

$$O^+ + O_2 \xrightarrow{k_1(T)} O_2^+ + O \tag{3.4}$$

and

$$O^+ + N_2 \xrightarrow{k_2(T)} NO^+ + N \tag{3.5}$$

in which $k_1(T)$ and $k_2(T)$ are the temperature-dependent reaction rates. Note that the resulting molecular ions are much more quickly recombined with the ambient molecular neutrals than O^+. The reduction in $[O^+]$ in a reference frame moving with the plasma can be expressed as (Perry et al., 2013):

$$\frac{\partial[O^+]}{\partial t} = -[O^+](k_1(T)[O_2] + k_2(T)[N_2]). \tag{3.6}$$

Eq. (3.6) shows the sensitivity of the temperature of the plasma and the neutrals. The reaction rates can increase substantially with temperature (St.-Maurice and Torr, 1978). For example, if the effective temperature of the gas doubles from 1700 to 3400 K, $k_1(T)$ doubles and $k_2(T)$ increases eightfold. Such temperature spikes are not unheard of in the high-latitude region (Goodwin et al., 2014; Perry et al., 2015) and are predominately a byproduct of frictional heating between fast flowing ions and the neutral gas.

Under typical conditions, the reaction rates are, $k_1 = 1.5 \times 10^{-5}\text{m}^3\,\text{s}^{-1}$ and $k_2 = 6.5 \times 10^{-7}\text{m}^3\,\text{s}^{-1}$. Therefore, a volume of plasma of the order of $2 \times 10^{11}\text{m}^{-3}$ takes approximately 2 h to recombine and decrease by a factor of e at 300 km altitude. Under these conditions, a F-region irregularity, such as a plasma density enhancement, can be transported over large distances of the high-latitude ionosphere via $\vec{E} \times \vec{B}$ plasma convection, before it is chemically recombined.

Diffusion perpendicular to the magnetic field (i.e., "cross-field" diffusion) is strongly dependent on spatial scales. The cross-field diffusion coefficient for ions can be expressed as $D_{i\perp} = r_g^2 \nu_{in}$ (Kelley, 2009), where r_g is the ion gyroradius and ν_{in} is the ion-neutral collision frequency. For typical F-region values and scale sizes of interest here ($\lambda > 10\text{km}$), it can be shown that the contribution of diffusion to L_i is orders of magnitudes lower than chemical recombination (Tsunoda, 1988). At smaller spatial scales, cross-scale diffusion does become more important and must be considered when interpreting the presence of irregularities.

We have now dealt with most of the terms in Eq. (3.1). In the wintertime polar ionosphere (or when photoproduction and chemical recombination are balanced), the equation can be reduced to one that describes temporal variations in plasma density as a function of the transport of plasma density gradients and plasma loss (Eq. 3.6), that is:

$$\frac{\partial n_i}{\partial t} = -\vec{v}_i \cdot \nabla n_i \tag{3.7}$$

It is important to note that this equation is in the local rest frame (the Eulerian frame). That is, Eq. (3.7) describes what a ground-based instrument would measure in the presence of a plasma density irregularity. In the case of a density enhancement moving toward the instrument, $\partial n_i/\partial t > 0$ on the leading edge of the enhancement since $\vec{v}_i \cdot \nabla n_i < 0$ there, and vice versa for its trailing edge.

3.1.2 Plasma density enhancements

High-latitude F-region plasma density irregularities can be separated into two categories: enhancements and depletions. Plasma density enhancements are, simply put, structures with an enhanced plasma density relative to the ambient ionosphere. In this section, we will focus on the detection of these density enhancements and their source.

3.1.2.1 Detecting plasma density enhancements

In situ techniques

Arguably the most straightforward way of detecting plasma density enhancements is through in situ rocket or spacecraft observations. Rockets provide flexibility and high spatiotemporal resolution, making it easier to view a given region at a specific time, or perform common volume measurements with other instruments. Rocket missions (Moen et al., 2012) were able to identify enhancements which contained small scale ($\lambda < 10$ km)—decameter—variations as well. They used Langmuir probes to do so, a popular technique given its relative simplicity. Satellite missions use a variety of techniques (e.g., Langmuir probe measurements, retarding potential analyzers) and have contributed significantly to the study of plasma density enhancements and other plasma density structuring at high latitudes (Basu et al., 1990; Goodwin et al., 2015; Kivanç and Heelis, 1997; Zhang et al., 2017a). Rocket measurements can detect density variations down to the decameter scale, but only for several minutes over a confined geographic region, whereas spacecraft measurements can rarely achieve such a fine resolution, but they can collect data continuously over large swaths of the high-latitude ionosphere (Goodwin et al., 2015).

Radio techniques

Ionospheric plasma density enhancements can also be detected from the ground using remote sensing techniques. In Section 3.1.1, we discussed how enhancements can be detected using the ionosonde technique. However, more sophisticated radar systems can also be employed, as outlined here.

Incoherent scatter radar A type of radar system that is commonly used to resolve plasma density enhancements is the incoherent scatter radar (ISR). The ISR technique uses the backscatter power generated by ionospheric plasma to deduce the ionosphere's state parameters including plasma density, ion and electron, and bulk plasma velocity. The spatial resolution of ISR measurements varies depending on the system, but is typically of the order of tens of kilometers, with a temporal resolution of the order of 1–5 min. Unlike ionosondes, ISR measurements are not restricted to the bottomside ionosphere and can provide observations in multiple directions well into the topside ionosphere. However, ISRs are extremely sophisticated and, therefore, very expensive instruments. Accordingly, only a few ISRs have been built and are operating in the world at the moment.

An example of ISR measurements of plasma density irregularities is provided in Fig. 3.1, which shows data spanning approximately 18 h collected by the Resolute Bay Incoherent Scatter Radar—North (RISR-N) (Bahcivan et al., 2010), which faces northwards, and RISR-Canada (RISR-C), which faces southwards (Gillies et al., 2016). Fig. 3.1 shows RISR-C data collected by a beam directed at an azimuth of −157.0 degrees of elevation angle of 55 degrees, and RISR-N data from a beam directed at an azimuth of 26.0 degrees of elevation angle of 55 degrees. Note that these beams were directed in opposite directions—their azimuths were separated by approximately 180 degrees. These radars operate at radio frequencies well above the ionosphere's critical frequency, so their narrow radar beams do not suffer from refractive effects.

Plasma density is plotted in panels i and ii. Panels iii and iv show the median plasma density along two beams from each radar, covering 200 and 400 km altitude. The first beam has an elevation angle of 55 degrees (orange), while the second has an elevation angle of 75 degrees (blue). Both beams are directed along the same azimuth. Panels v and vi show the line-of-sight plasma velocity at a 55 degrees elevation angle, and panels vii and viii show the electron temperature at a 55 degrees elevation angle. In panels i and ii, a variety of relative density enhancements and minimums are apparent. In general, the plasma density is enhanced on the dayside (between 18:00 and 00:00 universal time, UT) relative to the nightside (after 00:00 UT).

The traces in panels iii and iv show the same trends as in panels i and ii, respectively. Variations in the median plasma density in both traces, especially after 03:00 UT, are readily apparent. The sudden drop in electron temperature at approximately 00:00 UT marks local sunset; the lack of electron temperature enhancements after that show there is negligible particle precipitation present in either radar's field of view at night. We can, therefore, apply the same logic used in deriving Eq. (3.7) to conclude that the variations detected in panels ii are the result of F-region plasma density irregularities being transported into the region.

Both radars measure $\partial n_i/\partial t > 0$ just before 04:00 UT (panels iii and iv), followed by a $\partial n_i/\partial t < 0$ signature, consistent with the signature of an enhancement moving toward,

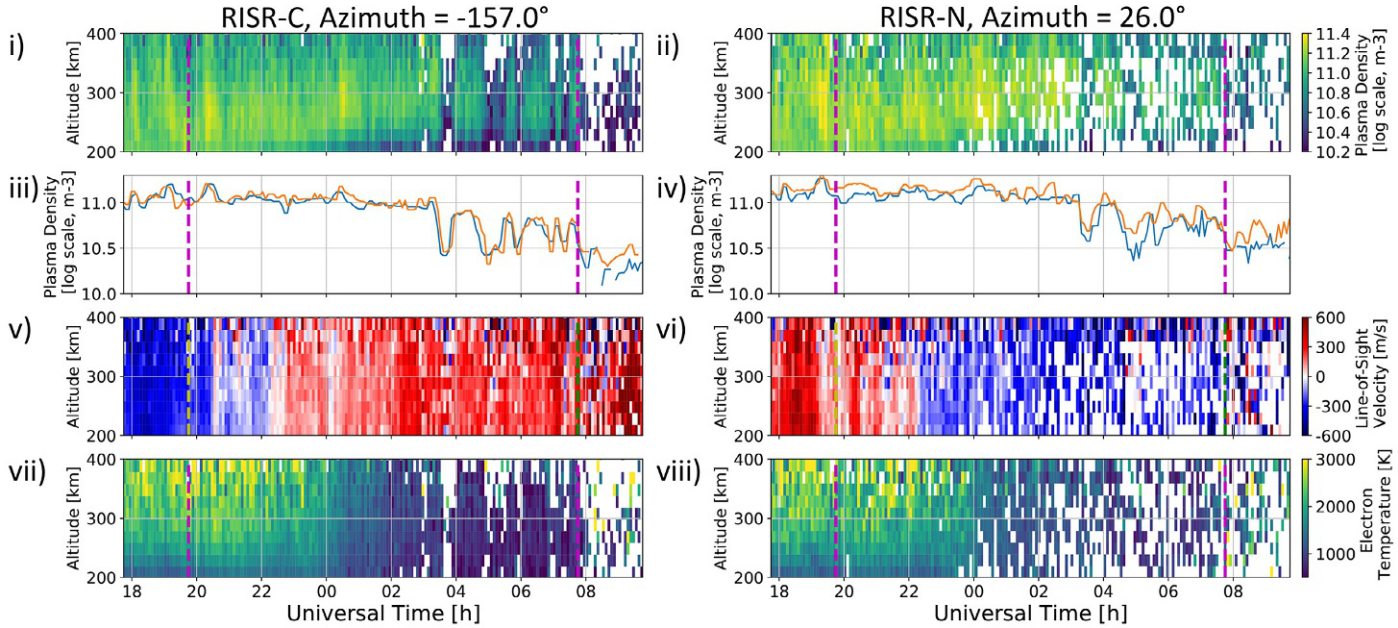

Fig. 3.1 September 29–30, 2019 observations from RISR-C and -N as a function of Universal Time (UT). (left) RISR-C observations at azimuth = −157.0 degrees and elevation = 55.0 degrees. (right) RISR-N observations at azimuth = 26.0 degrees and elevation = 55.0 degrees. In each subfigure: (i + ii) plasma density (iii + iv) the median plasma density between 200 and 400 km (a 15 min median filter has been applied), where *orange* corresponds to the beam of interest and *blue* is a similarly directed beam at an elevation angle of 75.0 degrees (v + vi) line-of-sight plasma velocity, where positive is away *(red)* from the radar and negative is toward *(blue)* the radar (vii + viii) electron temperature. *Dashed lines* indicate the locations of local noon (19:45 UT) and local midnight (7:45 UT). A Python program used to generate panels (i), (ii), and (v)–(viii) has been supplied in the supplementary information available at https://doi.org/10.1016/B978-0-12-821366-7.00001-9.

then away from each radar. A comparison of this feature in the higher (blue) and lower (orange) elevation beams of each radar shows that the enhancement is moving away from RISR-C and toward RISR-N, that is, in a southerly direction. This is consistent with the direction of the plasma flows measured by each radar (panels v and vi). This movement is consistent with the southerly global convection flow expected in that region at that time of day (Ruohoniemi and Greenwald, 2005). A similar effect can be seen on the dayside, such as near 19:00 UT, with the exception that the flows are $v_i > 0$ for RISR-N and $v_i < 0$ for RISR-C, suggesting a northerly motion. This movement is also consistent with the global convection flow expected in that region at that time of day.

We feel that it is necessary to point out that, in accordance with contemporary jargon, these enhancements would be referred to as "patches" depending on our definition of the ambient ionosphere. This is one of the several reasons why we feel that the term "patch" is outdated. Instead, language such as "large-scale plasma density irregularities" is, arguably, more descriptive, without implying that a particular or exceptional process is associated with enhancements that are twice as dense as the background. Furthermore, as Fig. 3.1 illustrates, quantifying the "background or ambient ionosphere" in the polar cap is exceedingly difficult.

Finally, panels vii and viii show that overall the dayside plasma has an elevated electron temperature, which is an expected result of photoionization. However, note that the plasma density enhancements are coincident with slight decreases in electron temperature. This is because the thermal capacity of the enhancements is larger than the ambient ionosphere. Under a constant supply of heat to the plasma, the temperature of the enhancements will be less than the ambient ionosphere, owing to their increased density with respect to the ambient ionosphere. This effect is not as readily apparent under nighttime conditions.

ISRs have, by far, been the subject of the most irregularity studies, no doubt given their capacity to estimate plasma density and plasma density enhancements. Some of the first high-latitude ISR measurements were performed with an ISR located in Chatanika, Alaska (which was subsequently moved to Greenland and contributed even further to the study of enhancements) (Kelley et al., 1982; Vickrey et al., 1980), which demonstrated that, indeed, the nighttime high-latitude ionosphere is replete with plasma density enhancements. Several ISR-based studies (we only provide a few here and suggest to the reader to consider the references contained therein) have followed since and became more common as more ISR facilities were installed in Scandinavia (Carlson et al., 2004; de la Beaujardière et al., 1986), Nunavut, Canada (Dahlgren et al., 2012; Perry and St.-Maurice, 2018; Ren et al., 2018), and Poker Flat, Alaska (Liang et al., 2018; Nicolls and Heinselman, 2007). Observations by these systems have been pivotal in characterizing plasma irregularities, including enhancements, their generation mechanisms, their dynamic properties, and their connection to other M-I-T coupling processes.

Global navigation satellite system Global navigation satellite system (GNSS) transmissions serve as another favored way of detecting and studying irregularities. Plasma densities are inferred by comparing the phase delay multifrequency signals propagating between transmitters (usually located in orbit) to a receiver (usually located on the ground) (Mannucci et al., 1998). With this technique, one can estimate the total electron content (TEC) along the path length of the transmissions and, therefore, irregularities in TEC. Since the frequency of the transmissions is well above the critical frequency of the ionosphere, refractive effects are negligible and the propagation path of a transmission is essentially line-of-sight.

The temporal resolution of TEC measurements is typically of the order of five minutes with a 1 degree by 1 degree geographic latitude and longitude resolution. The technique provides a large-scale perspective. Thanks to the proliferation of GNSS receivers in recent years, we are now able to detect and track enhancements over several hours. A notable example of this is shown in Fig. 3.2, where GNSS techniques were used to track plasma density enhancements as they circulated the polar cap ionosphere in the high-latitude convection flow (Zhang et al., 2013).

In Fig. 3.2, the data are presented in polar magnetic coordinates, with longitudinal lines of magnetic local time (MLT). In Fig. 3.2B, a grouping of TEC enhancements (circled) is seen entering the polar cap, in the late-morning sector. The higher TEC values at lower latitudes, in the morning, noon, and afternoon sectors is the sunlit ionosphere. Proceeding through Fig. 3.2C–I, the enhancements move across the polar cap, in an antisunward direction, along plasma convection streamlines, which are parallel to the equipotential contour line estimates derived from ground-based radar measurements (Ruohoniemi and Baker, 1998). It takes approximately 3–4 h for the grouping of TEC enhancements to complete the circuit—entering (B) and exiting (F) the polar cap region, and returning to the approximate entry location (I). Interestingly, the enhancements move along both open and closed magnetic field lines; the latter segment as the enhancements move sunward along the evening sector of the polar cap region.

One of the major goals of polar cap studies has been the ability to detect and track plasma density irregularities in the region, from their sources to their sinks. Fig. 3.2 was the first to demonstrate the "life cycle" of these irregularities. A GNSS-based technique is the only capable of achieving such a large-scale picture of the coupled M-I-T system. A rich variety of other notable works has demonstrated the utility of GNSS-based techniques for studying plasma density irregularities at high latitudes (Chartier et al., 2018, 2019; David et al., 2019; Noja et al., 2013; Watson et al., 2016).

Optical techniques

Not all observations of plasma density enhancements require radio waves. Optical measurements of F-region "red line" emissions (630 nm), reveal plasma undergoing dissociative recombination of O_2^+ (Wickwar et al., 1974), expressed by

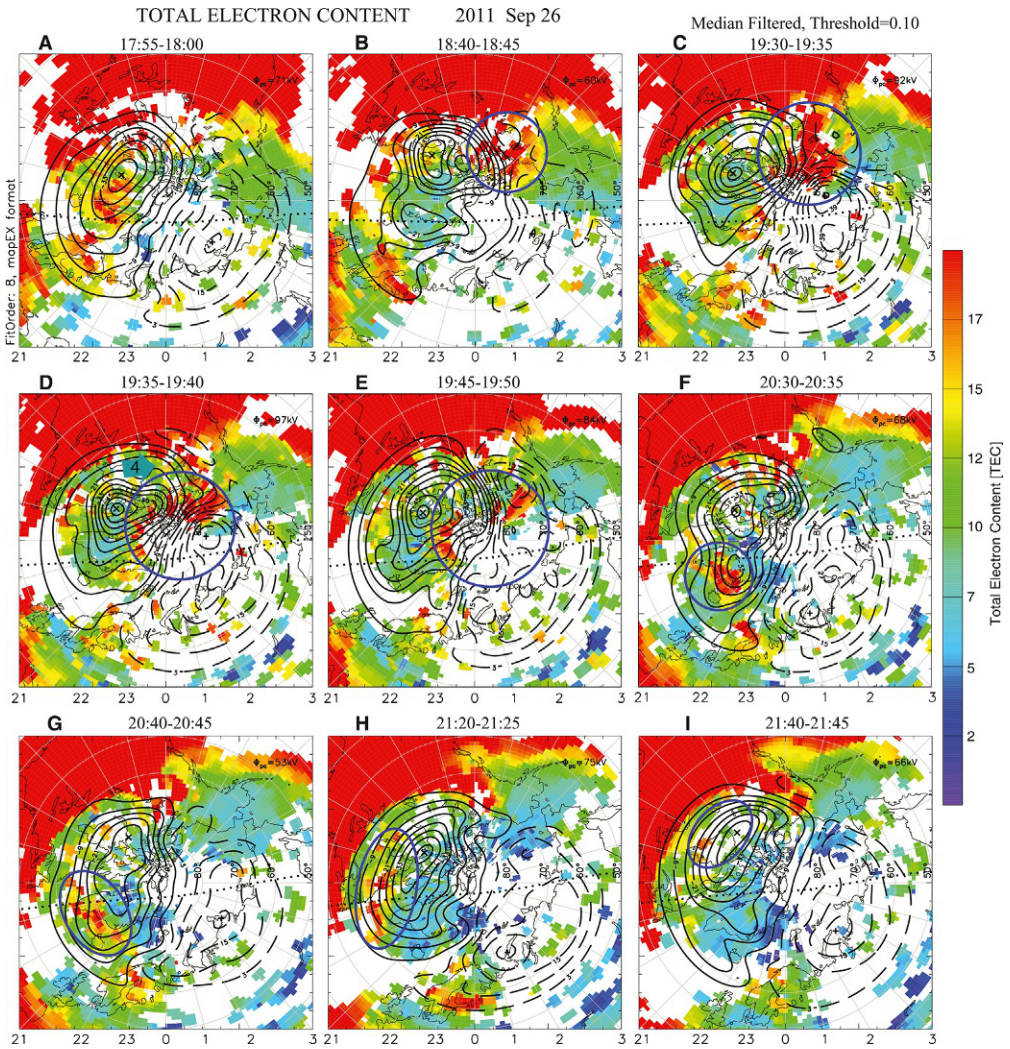

Fig. 3.2 TEC measurements of the northern polar cap region showing the introduction of plasma density enhancements into the region and their transpolar circulation (Zhang et al., 2013). The enhancements *(circled)* are transported through the region via the high-latitude plasma convection streams. The TEC maps are presented in a geomagnetic polar format in which the lines of longitude are magnetic local times (MLT), which remain fixed while the Earth rotates in a counterclockwise direction in the figure.

$$O_2^+ + e \rightarrow O + O^* \tag{3.8}$$

where O_2^+ is a product of the depletion of O^+, described earlier in Eq. (3.4).

A plasma density enhancement will give way to more recombination and thus, more intense optical emissions than the surrounding region, which can be used to detect and track plasma density enhancements. Seminal work in this technique includes (Hosokawa et al., 2006; Lorentzen et al., 2004; Weber et al., 1984).

There are two caveats to this technique that should be discussed. First, the reaction described by Eq. (3.4) is determined by the concentration of O_2; thus, the 630 nm optical emission is altitude dependent. Below 200 km, O* becomes "quenched" by collisional deactivation with the ambient atmosphere. At higher altitudes, O_2 becomes too tenuous to produce O_2^+ for the emission. Therefore, a bias exists in the technique of studying plasma density enhancements using the 630 nm emission; only enhancements in an altitude range of the order of 200–400 km are likely to be observable.

Fig. 3.3, reproduced from (Perry and St.-Maurice, 2018) provides a demonstration of the 630 nm emission and its altitude dependence. In the top panel are data from an Optical Mesosphere Thermosphere Imager (OMTI) (Shiokawa et al., 2000) located at Resolute Bay. 630-nm emissions presented in a "keogram" format in which a longitudinal slice of the imager's field of view is plotted as a function of time. Starting at 05:00 UT, a steady stream of emission enhancements, corresponding to plasma density enhancements, is seen to move in a north-to-south direction.

The bottom panel of Fig. 3.3 presents plasma density measurements taken by RISR-N, which samples a common volume with the imager. There is a clear correlation between the presence of plasma density enhancements measured by RISR-N and the 630-nm emission enhancements detected by OMTI. There is also a very noticeable connection between the increased altitude of the enhancements, measured by RISR-N, and the optical intensity, measured by OMTI. This is especially apparent just before and after 08:00 UT. The enhancements at higher altitudes have lower optical intensities because the concentration of molecular oxygen decreases with increasing altitude.

The second caveat related to this technique has to do with the nonnegligible vertical component of the F-region plasma's convection velocity in the polar cap ionosphere, a result of the fact that the magnetic field at high latitudes is not entirely vertical. The vertical plasma drift causes plasma density enhancements to also move vertically. This can lead to an increase (downward motion) or decrease (upward motion) of the enhancement's 630-nm emissions. This is due to the fact that the enhancement is driven into a denser neutral atmosphere, increasing the chemistry related to its emissions (Perry et al., 2013). Therefore, when interpreting the 630-nm emissions of plasma density enhancements in the polar cap, one has to consider the fact that the emissions depend on both the altitude and the vertical motion of the enhancements.

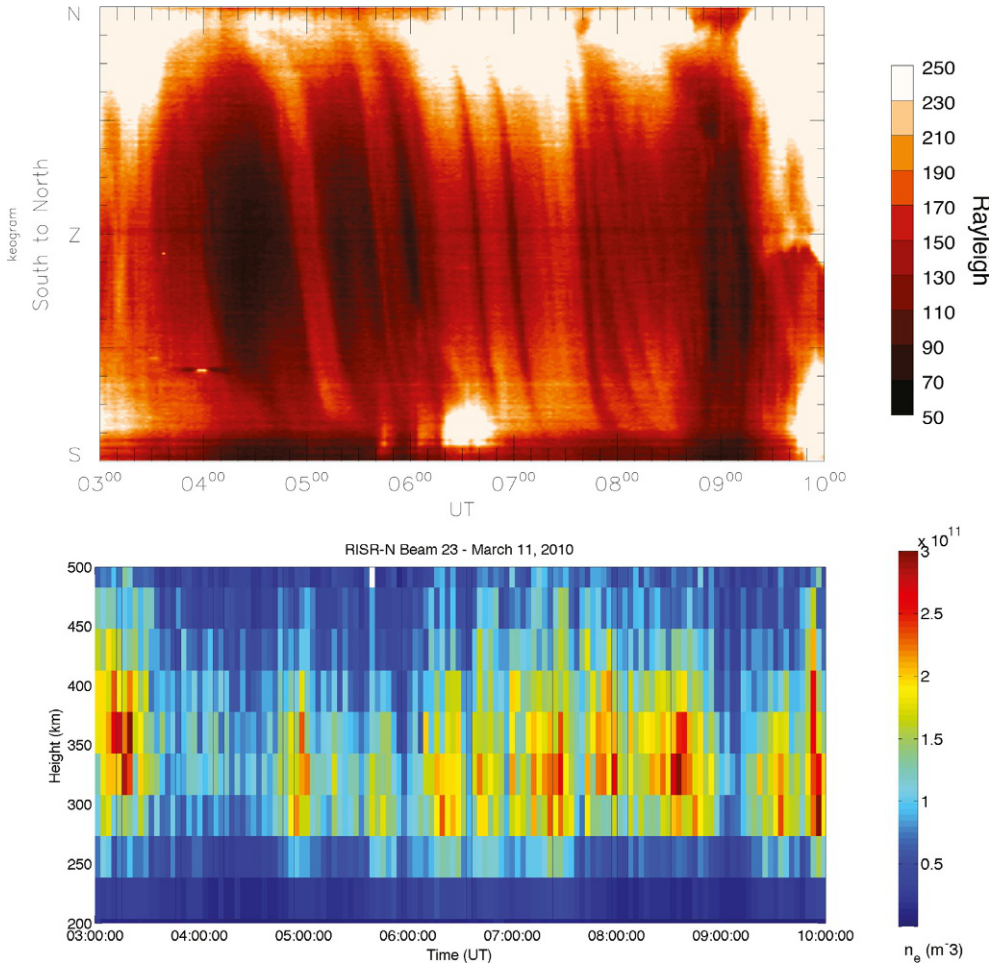

Fig. 3.3 630-nm emissions of plasma density enhancements moving in a north-to-south direction, measured at Resolute Bay (top panel), with simultaneous plasma density measurements from RISR-N (bottom panel). Just before and after 08:00 UT, the optical emissions decrease, corresponding to the measured increase in altitude of the plasma density enhancements (Perry and St.-Maurice, 2018).

3.1.2.2 Sources of plasma density enhancements

Now that some of the properties and detection methods of plasma density irregularities at $\lambda > 10$km have been discussed, it is logical to discuss their source and generation mechanisms.

Impact ionization by particle precipitation is one way of generating plasma in the M-I-T system. Plasma density irregularity production due to particle precipitation transpires in the cusp region (Goodwin et al., 2015; Kelley et al., 1982; MacDougall and

Jayachandran, 2007; Moen et al., 2012; Oksavik et al., 2006; Walker et al., 1999; Weber et al., 1984) and the deep, nighttime polar cap (Perry and St.-Maurice, 2018). However, Fig. 3.1 shows that interspersed on the nightside are plasma density enhancements that are of the order of the dayside plasma density observations measured earlier in the day (<3 UT). That is, the measured density of the irregularities is higher than what is typically observed for impact ionization, and more consistent with photoproduction.

The dayside ionosphere was recognized and shown to be a source of irregularities almost as soon as the appropriate sensors and measurements were available (Hill, 1963). Since then, more contemporary measurements, i.e., Fig. 3.1, showing that the irregularities are moving away from the dayside ionosphere, into the polar cap, and Fig. 3.2, which undeniably shows irregularities emerging from the sunlit ionosphere, have upheld the notion of the dayside ionosphere as a "resevoir" (Carlson, 2012) for plasma density irregularities in the polar cap ionosphere.

The transport of dayside plasma to the nightside ionosphere is often referred to as the tongue of ionization (TOI), owing to its resemblance of a tongue of high-density plasma protruding into the nightside ionosphere from the dayside along plasma convection streams (Knudsen, 1974; Sato, 1959). However, this terminology is misleading in that it presents the image of a steady and uniform stream of plasma moving from the dayside into the nightside polar cap region. TEC maps may give this impression, however, their resolution is fairly coarse. In reality, more finely resolved spatial and temporal measurements of such events reveal that a TOI is a highly structured stream of irregularities (Hosokawa et al., 2009b).

Nevertheless, several observations have shown that, indeed, dense sunlit plasma often moves to higher geomagnetic latitudes in a narrow longitudinal channel, under the influence of high-latitude plasma convection streams. A striking example of this is provided in Fig. 3.4, which shows a low-latitude plume of enhanced plasma during a geomagnetic storm, a storm-enhanced density (SED) plume, moving along high-latitude plasma convection streams and crossing the polar cap ionosphere (Foster et al., 2005). The question remains, however: what processes are responsible for transporting high-density plasma into the polar cap, and thus initiating plasma irregularities—localized plasma density enhancements—which are a seemingly ubiquitous feature of the polar cap ionosphere, including within TOIs?

Several mechanisms have been put forward to explain the generation and introduction of plasma density irregularities in the polar cap ionosphere, with some observational evidence supporting each. The question that still remains unanswered is "which mechanism is most important?" (Carlson, 2012). It is beyond the scope of this work to thoroughly detail each hypothesized generation mechanism and their relative importance. We will, however, discuss a mechanism which appears to be a strong candidate for generating the bulk of the plasma density enhancement irregularities. The hypothesis is that the bulk of the observed irregularities are the ionospheric byproducts of magnetic

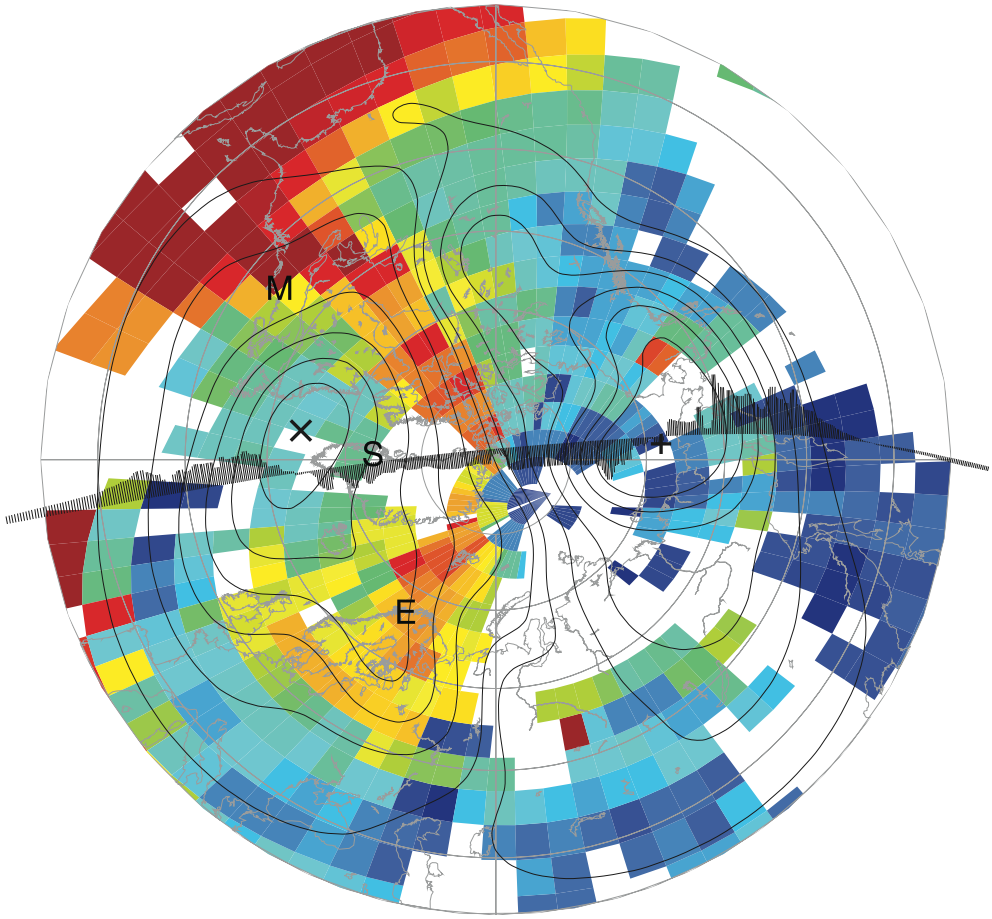

Fig. 3.4 Emerging from an SED plume at lower latitudes during a geomagnetic storm, a TOI is formed as high-density plasma moves into and across the polar cap along plasma convection streams (Foster et al., 2005). The format of this plot is identical to that presented earlier in Fig. 3.2.

reconnection dynamics occurring between the IMF and the terrestrial magnetic field (Lockwood and Carlson, 1992), a process that is also referred to as a flux transfer event (FTE) (Russell and Elphic, 1979) (see also Section 1.2). The ionospheric signature of two consecutive FTEs is depicted in Fig. 3.5, displayed in the same polar format as Figs. 3.2 and 3.4.

Fig. 3.5 illustrates the effect of an FTE that occurs under a purely southward IMF, that is, one in which the z-component is negative and is the only nonzero component of the IMF's vector, in geocentric solar magnetospheric (GSM) coordinates. The demarcation between the lower latitude, dense, photoionized plasma, and the more tenuous nighttime plasma is depicted as a horizontal line in Fig. 3.5, 1. The electrodynamics of an FTE map

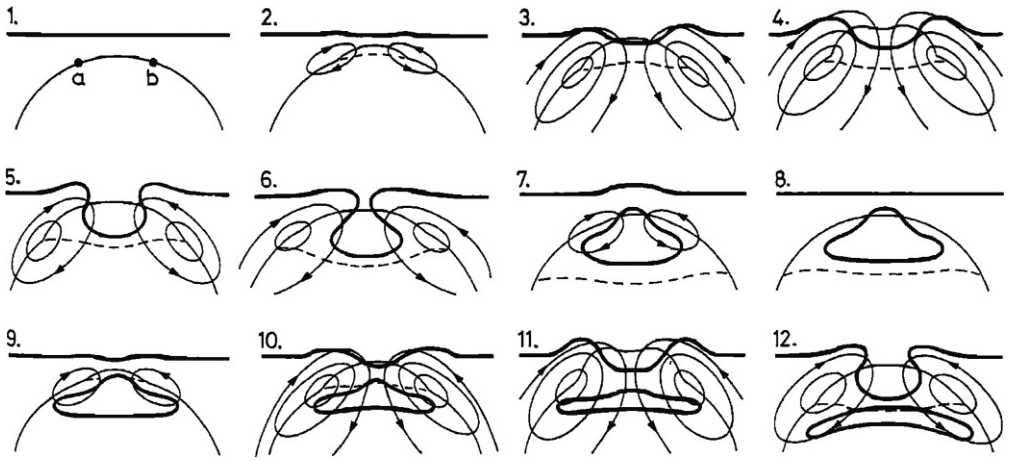

Fig. 3.5 The suggested mechanism for the generation of plasma density enhancements as a results of FTEs (Lockwood and Carlson, 1992). A demarcation between low and high-density plasma is illustrated with a *bold horizontal line*.

from the magnetopause to the high-latitude ionosphere along magnetic field lines, resulting in an electric potential between points "*a*" and "*b*" on the open-closed magnetic field line boundary, is often referred to as the "merging gap." In the reference frame of the boundary, an electric field, directed along the arc $b \rightarrow a$ is established, moving the plasma in an antisunward direction, through the gap, via the $\vec{E} \times \vec{B}$ drift ($\vec{B}$ into the page). In the Earth's reference frame, the FTE will result in either a fixed merging gap with an antisunward directed plasma flowing through it, a stationary plasma with an equatorward expanding gap, or a combination of both (Cowley and Lockwood, 1992; Lockwood and Carlson, 1992).

The electric field directed along the arc joining $b \rightarrow a$ produces a convection drift perpendicular to that arc, resulting in the circular front of protruding plasma shown in Fig. 3.5, 3–5. As the FTE event subsides, the electric potential from $b \rightarrow a$ decreases. As a response, the convection flow decreases, or equivalently, the open-closed field line boundary contracts poleward, resulting in a teardrop shaped volume of enhanced plasma moving into the polar cap region, i.e., Fig. 3.5, 6–7. Consecutive FTE events create a stream of plasma density irregularities moving antisunward. Indeed, this is commonly observed in the polar cap ionosphere when the IMF has a southward component, hence the TOI. FTEs are often sporadic, nonetheless, the frequency of such irregularities closely matches that of FTEs. This mechanism involves a specific ordering of geophysical events and signatures which have not been detailed here, but all of them have been experimentally confirmed with various experiments since the hypothesis was put forward (Carlson, 2012).

3.1.3 Plasma density depletions

Plasma density depletions are the counterpart to plasma density irregularities that are enhancements. Like the enhancements, which we have focused on up to this point, depletions are also described by Eq. (3.7). Accordingly, in the absence of plasma production, e.g., in the nighttime polar ionosphere, a plasma density depletion at scale of $\lambda >$ 10 km can also have a lifetime of several hours and be transported throughout the high-latitude region via the convection streams. This is strongly dependent on many circumstances including the time of day, geomagnetic conditions, and the convection path the irregularity takes through the high-latitude region (Sojka et al., 1981a, b). The properties of depletions can be observed with the same instruments as plasma density enhancements, although it is more difficult given that their densities can be near or below the sensitivity of the instruments. This can be seen in Fig. 3.1, where there are more data gaps at night than during the dayside due to the challenges of measuring low plasma densities with an ISR.

3.1.3.1 Sources of plasma density depletions

Enhanced Joule heating

A mechanism by which F-region plasma density depletion structures are formed is through the enhanced recombination of O^+ via the increased reaction rates $k_1(T)$ and $k_2(T)$ in Eqs. (3.4) and (3.5), relative to the surrounding plasma. These rates are sensitive to increases in the ion plasma temperature. Joule heating will increase the ion plasma temperature in the high-latitude F-region ionosphere. This process involves the sum of the heat exchange between ion, electron, and neutral gases and frictional heating. The latter is proportional to the square of the differential velocity between the ion and neutral gases (St.-Maurice and Hanson, 1982).

Narrow channels of plasma flow enhancements colocated with ion temperature enhancements and plasma density depletions (and frequently particle precipitation) are often observed in the high-latitude and polar cap region. For example, in one observation, a plasma density trough was detected on the edge of auroral arc (Opgenoorth et al., 1990) and polar sun-aligned arc (Perry et al., 2015) in another observation (see also Section 2.3). In the case of the latter, the trough was seen to move through the region in conjunction with the arc showing that not only could plasma density depletions be created deep in the polar cap, but that they could also be transported across significant distances.

Plasma evacuation

The aforementioned sun-aligned arc observation also invoked another depletion mechanism associated with intense field-aligned-currents (FACs) and aurora (see also Section 2.1): plasma evacuation (Perry et al., 2015). This mechanism was first broached

(Doe et al., 1993; Zettergren and Semeter, 2012) to help explain "cavities" frequently observed in the high-latitude ionosphere. An auroral arc can be represented by a FAC pair, where the upward FAC is carried by downward moving electrons, producing the arc's optical emissions. When the E-region conductivity is low, the horizontal currents connected to the downward FAC component of the arc are completed in the lower F region. Plasma will be evacuated from the downward FAC region: the ions move horizontally away from the downward FAC, while the electrons will move vertically upward along the field line. This seeds a plasma depletion cavity, which leads to an enhanced electric field (to maintain the current flow), strengthened plasma convection drifts, frictional heating, and increased reaction rates for the chemical recombination of the ions. This feedback effect accelerates, establishing a plasma density depletion. Although it does not appear that the evacuation mechanism can create a F region depletion on its own, indications are that it works well in conjunction with the chemical recombination mechanism, where the evacuation mechanism contributes strongest at lower F-region and E-region altitudes, and the chemical recombination dominates higher-up (Perry et al., 2015; Zettergren and Semeter, 2012).

Plasma convection

If the high-latitude convection velocity associated with a parcel of plasma is slow, the parcel can remain in the dark polar cap for an extended period of time. This would provide the plasma with an extended period of time to become depleted, assuming no significant plasma production mechanisms are present. This plasma stagnation can result in a plasma depletion structure in the high-latitude region: the "polar hole" (Brinton et al., 1978; Sojka et al., 1981b). The stagnation related hole generally occurs during periods of quiet geomagnetic activity.

A polar hole may also form during active geomagnetic conditions. This feature is not due to stagnation but rather enhanced plasma convection velocities. At polar latitudes, the geomagnetic field has a small, nonnegligible, horizontal component, producing a vertical $\vec{E} \times \vec{B}$ drift. When plasma convection becomes enhanced, the downward component of the plasma convection will also become enhanced, driving the plasma vertically downwards into the dense neutral atmosphere, increasing the chemical recombination of plasma, producing a region of depleted plasma—a hole (Sojka et al., 1981a).

Another way by which plasma depletions can be introduced into the polar ionosphere is by periodically changing the magnetic longitude of the magnetic cusp, the entry point of plasma into the polar region (Milan et al., 2002). In general, plasma entering the polar ionosphere through a cusp located in the afternoon MLT sector convects from the nightside ionosphere along the sunlit evening flank, in a similar fashion to the irregularities observed in Fig. 3.2E–I. On the other hand, plasma entering through a morning MLT cusp will have convected from the nightside along the morning sector; the difference being that this route generally lacks a source of significant plasma

production—photoionization. Thus, a mixture of both low and high-density plasma flows into the polar cap if the position of the cusp oscillates between an afternoon and morning source region due to a varying y-component of the IMF. This effect has both been observed by Milan et al. (2002) and Sakai et al. (2013) and modeled by Sojka et al. (1993, 1994). It is also important to point out that this mechanism, examined from another point of view, may be considered a density enhancement generation mechanism as well. If the source of the plasma streaming into the polar cap is the morning MLT, with sporadic excursions to the afternoon MLT sector, the mostly tenuous stream of plasma would be populated by infrequent regions of enhanced plasma density, compared to the ambient ionosphere.

3.1.4 Plasma density irregularities as an agent of space weather

"Space weather" is a term that describes plasma processes in the near-Earth geospace environment that can affect society. These processes can be initiated externally, for example, by solar coronal mass ejections, or internally by M-I-T coupling processes. Plasma density irregularities (enhancements and depletions) are a major focus of M-I-T coupling and space weather research for two prime reasons. First, they are the byproduct of multiscale M-I-T coupling processes, such as FTEs or enhanced Joule heating events. Second, they can pose a significant hazard to radio wave communications in the high-latitude and polar regions. Radio communications in these regions are becoming increasingly important as civilian and economic entities, such as commercial shipping and airlines, escalate their activities there. By studying the characteristics of irregularities, understanding their sources and sinks, and specifying their effects on radio wave communications, we can mitigate their negative effects on society.

In this section, we will focus on the effects of the irregularities on radio communications in the high-frequency (HF; 3–30 MHz) portion of the spectrum. The effects on radio transmissions on other regions of the radio spectrum will be covered elsewhere in this compendium. HF communications are commonly used in remote geographical regions, such as the polar cap, because of their ability to propagate to points "over the horizon." Specifically, the signals propagate from the transmitter to the ionosphere and are reflected back toward the ground.

HF transmissions whose wave vectors are at an acute angle with respect to the vertical can reach receivers that are well beyond the line-of-sight—over the horizon—using the ionosphere as a reflecting medium. This mode of radio propagation can be described by refraction and total internal reflection. From a simplified version of the Appleton-Hartree equation, the index of refraction, n, of a radio wave is

$$n = \sqrt{1 - \left(\frac{f_p}{f_0}\right)^2} \tag{3.9}$$

where f_o is the frequency of the radio wave, and f_p is the plasma frequency. A quick calculation will show that ionospheric plasma frequencies and HF frequencies are of the same order; therefore, $n \neq 1$ for HF communications is common (Gillies et al., 2012). In order to achieve high fidelity in radio communications, a smooth and uniform ionosphere, free of irregularities, is preferred for an HF communications system that is transmitting over-the-horizon. Otherwise, plasma density irregularities would present as irregularities in the value of the index of refraction; the transmissions would be refracted and reflected in an irregular way, degrading the communications link.

3.1.4.1 Off great-circle path deviations

Some of the most dramatic and compelling evidence of the ramifications of plasma density irregularities on HF radio links in the polar cap region is provided in Fig. 3.6 (Warrington et al., 1997), which shows the bearing (angle of arrival) of radio transmissions received at Alert, Canada, originating from Thule, Greenland, as a function of universal time (UT). Transmissions arriving along the great-circle path between the two points have a bearing of approximately 200 degrees. As Fig. 3.6 shows, the bearing of the received transmissions varies quite dramatically, especially between 8 and 13 UT, where the angle varies by approximately 100 degrees.

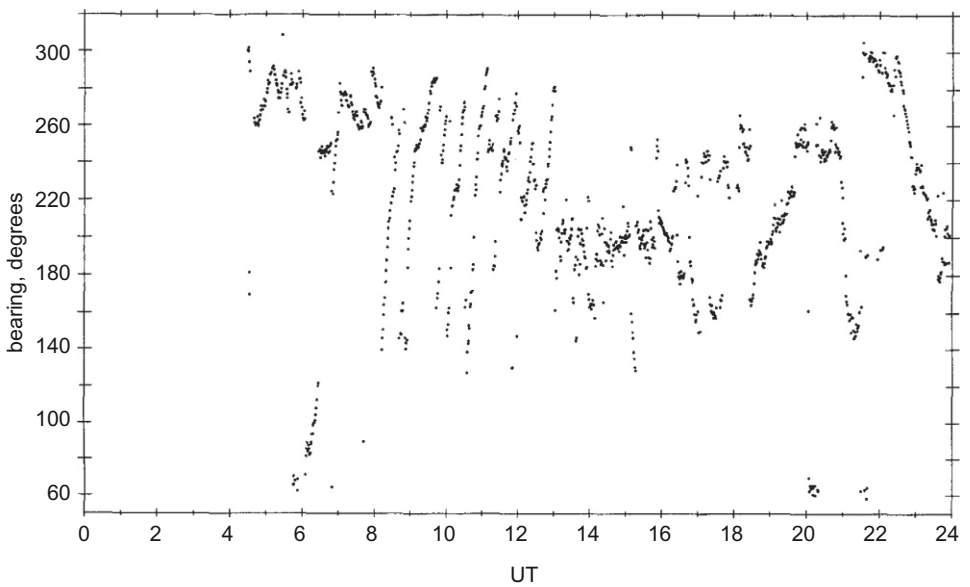

Fig. 3.6 Data from an HF radio link between Alert, Canada and Thule, Greenland showing evidence of significant deviations in the trajectory of the transmitted/received signal. The nominal bearing for the radio link is approximately 200 degrees (Warrington et al., 1997).

The deviations in Fig. 3.6 were attributed to the presence of plasma density irregularities—enhancements—along the ray path between the transmitter and receiver stations. Irregularities introduce significant gradients in plasma density into the ray propagation path which, in accordance with the principles of refraction and internal reflection, will cause the transmissions to deviate both vertically and laterally from their great-circle paths. As one can imagine, these substantial deviations pose a hazard to HF systems which rely on great-circle path propagation to operate effectively.

3.1.4.2 A source of small-scale irregularities and radar backscatter

Plasma density irregularities at scale of $\lambda > 10$km are not only hazardous to radio communications in the high-latitude region because they can deviate the general trajectory of transmissions, but also because they are a large backscatter target of HF radio waves. HF coherent backscatter was recognized very early on in the advent of radar and has been studied extensively in the context of solar-terrestrial physics for decades.

When a radio wave interacts with a plasma population, the incident electric field of the radio wave accelerates the charged particles, which then scatters radiation at a Doppler shifted frequency (Jackson, 2007). At radio frequencies comparable to the plasma frequency (i.e., at HF), a radio wave incident on a volume of plasma will interact with the plasma, which will, in response, emit scattered radiation. The foremost hypothesis regarding radar backscatter originating from ionospheric altitudes is that the scattering processes are analogous to Bragg scattering when $\vec{k} = \pm 2\vec{k}_p$, where $\vec{k}$ is the wave vector of plasma density irregularities and $\vec{k}_p$ is the wave vector of the incident radio wave (Fejer and Kelley, 1980; Milan et al., 1997). The Bragg condition reveals, however, that the irregularities responsible for the scattering have a decameter-scale size (e.g., the 3–30 MHz HF band corresponds to a Bragg scale of 50–5 m)—several orders of magnitude below the scale which we are interested in. The connection between HF radar backscatter from these decameter irregularities and plasma density irregularities at scale of $\lambda > 10$ km is that the latter seed plasma instability processes, which generate the decameter irregularities responsible for coherent backscatter.

The gradient-drift instability (GDI) is generally regarded as a primary source of decameter-scale irregularities in the high-latitude ionosphere (Cerisier et al., 1985; Simon, 1963; Tsunoda, 1988). The onset of the GDI occurs on a plasma density gradient, which are associated irregularities. If an electric field is applied, such as the convection electric field driving $\vec{E} \times \vec{B}$ plasma drifts in the high-latitude regions, the edges whose gradient is parallel to the convection velocity will be unstable to the GDI, while those that are antiparallel will be stable (Keskinen and Ossakow, 1982). Accordingly, in the situation of a plasma density enhancement in the polar cap, the "trailing" of the

enhancement moving through the polar cap is unstable to GDI, while the "leading" is stable. As a result, decameter-scale irregularity growth is strongest on the trailing. We should, therefore, expect that coherent backscatter should also be strongest on the trailing. As it turns out, this is not necessarily the case.

Fig. 3.7 (Dahlgren et al., 2012) shows a plasma density enhancement captured by three separate instruments: the RISR-N ISR, the OMTI imager, and the HF Super Dual Auroral Radar Network (SuperDARN) (Chisham et al., 2007; Greenwald et al., 1995) system located at Rankin Inlet, Nunavut. The strength of coherent backscatter received by SuperDARN is indicated in the grayscale tiling; the colored contours indicate plasma density measured by RISR-N; and, the dashed line indicates the outline of the irregularity's optical signature measured by OMTI. Two things are apparent in this figure. First, enhancements are not the only source of coherent backscatter in the high-latitude region. It is believed that they are a major source; however, there is insufficient evidence as of yet to support this. Second, the agreement on the position of an enhancement by three separate instruments using three different techniques is clear, validating the efficacy of the techniques discussed earlier, in Section 3.1.2.1.

The inset in Fig. 3.7 shows that backscatter is present throughout the enhancement. There is a region of elevated backscatter on the northeast portion of the enhancement, which was a leading edge according to the drift of the irregularity in this event. This is contradictory to the widely held belief that radar echoes should be strongest on the trailing edges of such enhancements.

It is important to note that we are not taking into account the fact that the geolocation of the echoes may be inaccurate due to the off great-circle path deviations discussed earlier. This is not taken into account in SuperDARN's geolocation algorithms. Another factor that must be considered with HF coherent backscatter in general is that the decameter-scale irregularities are field aligned. The Bragg condition can only be satisfied when the incident radar wave vector is close to perpendicularity with the local magnetic field direction. It is in this direction that plasma diffusion is slowest (relative to diffusion along the magnetic field line), allowing for a longer irregularity lifetime (Tsunoda, 1988). Nevertheless, observations (Hosokawa et al., 2009a) and simulations (Gondarenko and Guzdar, 2004b) have consistently shown that enhancements such as the one shown in Fig. 3.7 are seemingly saturated with irregularities.

As a strong scattering target, irregularities such as the one shown in Fig. 3.7 are a space weather hazard to HF radio communications and other systems as well, including GNSS. Details of the latter will be provided elsewhere in this compendium, but, in short, the decameter-scale irregularities seeded by irregularities at scale of $\lambda > 10$ km are believed to be the source of both amplitude and phase scintillation of signals into the very- and ultrahigh frequency, and L radio spectrum bands.

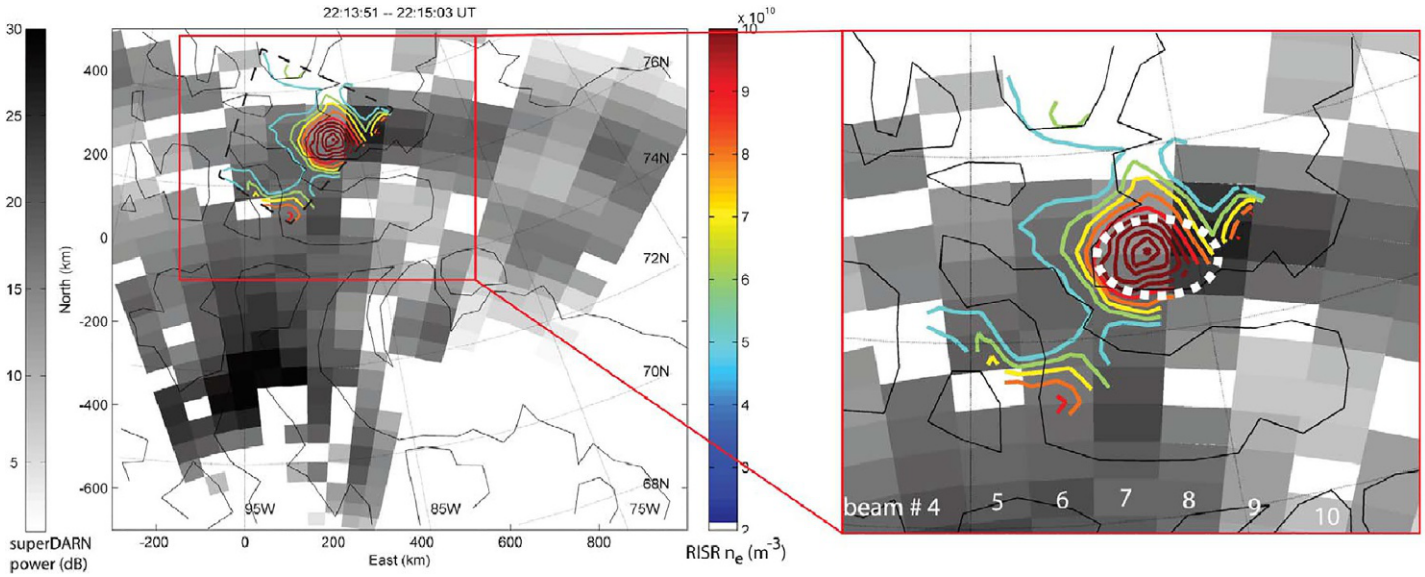

Fig. 3.7 Coincident measurements of a plasma density enhancement. SuperDARN backscatter echoes are presented in *grayscale tiling*, RISR-N plasma density observations are given in *colored contours*, and the *white dashed line* indicates the outline of the irregularity's optical signature measured by an OMTI imager (Dahlgren et al., 2012).

3.1.5 Plasma density irregularities in the M-I-T system

The ionosphere is not a closed system, and it is strongly coupled to the magnetosphere and the thermosphere—the M-I-T system. For example, recall the feedback effect discussed earlier in Section 3.1.3.1 related to the generation of plasma density depletions via enhanced Joule heating, and its dependence on the concentration of thermospheric constituents. Up to this point, the irregularities have been contextualized as products of dynamic M-I-T coupling processes, for example, as the consequence of FTEs or SED plumes. One may get the impression that they are passive features of the larger M-I-T system; however, there is sufficient evidence showing that this is not necessarily the case. That is, the irregularities actively participate in—even incite—M-I-T coupling processes as they move throughout the polar cap.

Regardless of their genesis, plasma density irregularities—enhancements and depletions—constitute conductivity gradients in the ionosphere. Accordingly, the irregularities are often colocated with dynamic plasma phenomena such as elevated plasma flows (Kivanç and Heelis, 1997). The interconnections between these phenomena can be expressed mathematically in the F region (Perry et al., 2015; Sofko et al., 1995):

$$\vec{J}_{\parallel} = -\Sigma_P \nabla \cdot \vec{E}_{\perp} - \vec{E}_{\perp} \cdot \nabla \Sigma_P - \nabla \Sigma_H \cdot \hat{b} \times \vec{E}_{\perp}, \tag{3.10}$$

in which $\vec{J}_{\parallel}$ is the parallel field aligned current density, $\hat{b}$ is the unit vector along the terrestrial magnetic field ($\vec{J}_{\parallel} \cdot \hat{b} > 0$; a positive current density directed parallel to the magnetic field), $\vec{E}_{\perp}$ is the electric field driving plasma convection, and Σ_P and Σ_H are the height integrated Pedersen and Hall conductivity, respectively.

The first term on the right-hand side of Eq. (3.10) has been referred to as the "magnetospheric component" while the remaining two terms have been referred to as the "ionospheric component" (Sofko et al., 1995). Above 200 km, $\Sigma_P > \Sigma_H$. The introduction of a plasma density irregularity, expressed by a nonnegligible value of $\nabla\Sigma_P$, into an otherwise uniform plasma field would need to be supported by changes in the magnitude of $\vec{E}_{\perp}$ and/or $\vec{J}_{\parallel}$ to maintain current continuity, $\nabla \cdot \vec{J} = 0$ (where $\vec{J} = \vec{J}_{\perp} + \vec{J}_{\parallel}$), demonstrating the M-I-T connection. Note that the role of the thermosphere is embedded in the value of Σ_P.

Other work has shown that some enhancements have high-electron temperatures (Ma et al., 2018; Zhang et al., 2017a), compared to others, indicating that they are subject to low-energy particle precipitation as they move through the polar region. Thus, the notion of irregularities being a remnant or a "fossil" of a bygone M-I-T coupling process is inaccurate. One of the more compelling lines of research concerning irregularities and M-I-T coupling has to do with their connection to magnetospheric phenomena, such as ion outflow and merging. In a rather serendipitous observation, an ISR captured a plasma density enhancement moving into a region of ion upflow, demonstrating a "connection

between horizontal plasma transport … and vertical transport along the nightside polar cap boundary" (Semeter et al., 2003). This process has also been measured in situ and linked to the convection velocity of the enhancements (Zhang et al., 2016).

Modeling efforts have indicated that enhancements may be a source of enhanced polar wind streams (Schunk et al., 2005), and that polar cap flow channels, which are often observed in conjunction with enhancements, are an ionospheric manifestation of structures in the magnetosphere lobe, related to magnetic merging in the magnetotail (Nishimura and Lyons, 2016). The latter is consistent with spacecraft observations, taken deep in magnetosphere (Goodwin et al., 2019), which have shown that enhancements and their associated flow channels carry a signature in the magnetosphere and, therefore, are heavily coupled with magnetospheric dynamics. This remains a largely unresolved topic at the moment, particularly the notion of a link between geomagnetic storms and substorms, their impact on dayside plasma flows, and interconnection with plasma density irregularities. Substorms have been linked to significant changes in high-latitude convection (Bristow and Jensen, 2007; Clausen et al., 2013) as well as the production of TOIs and enhancements in the polar region (Goodwin et al., 2020), although the causal link between these dynamics remains elusive.

This area of research enjoyed an increased amount of activity in recent years—the connection between plasma density irregularities in the polar region and magnetospheric dynamics. This activity is driven, in part, by the increased access to insightful ground- and space-based measurements of the coupled M-I-T system. The results, mentioned previously, have provided an indication that there is a strong link between processes in the M-I-T system, transpiring across multiple spatiotemporal scales, which are strongly coupled and, therefore, should be considered together when describing the coupled M-I-T system.

3.2 Modeling high-latitude F-region ionospheric fluid instabilities: Linear and nonlinear evolution and observational signatures

K.B. Deshpande[a,], M.D. Zettergren[a,*], A. Spicher[b], L. Lamarche[c], M. Hirsch[d], and M. Redden[a]*

[a]Department of Physical Sciences and Center for Space and Atmospheric Research (CSAR), Embry-Riddle Aeronautical University (ERAU), Daytona Beach, FL, United States

[b]Department of Physics and Technology, UiT the Arctic University of Norway, Tromsø, Norway

[c]SRI International, Menlo Park, CA, United States

[d]Boston University, Boston, MA, United States

* Equal contribution

3.2.1 Introduction and background

The high-latitude ionospheric plasma exhibits a high degree of spatial structure, which is known to evolve dynamically under the influence of magnetospheric forcing in addition to internal ionospheric processes. Plasma structuring at scale of $\lambda > 10$km, as discussed in Section 3.1.1, is thought to cascade into small scales through a variety of instability mechanisms and structuring processes, but the details of how plasma structuring evolves over time, especially nonlinearly, are poorly constrained. Intermediate-scale sized plasma structures (electron density irregularities) modify the phase and amplitude of transionospheric radio signals, a process referred to herein as scintillation. Rapid variations in the amplitude and phase of the radio signals such as the GNSS signals resulting from these irregularities in the ionosphere can vary with the latitude, season, and geomagnetic conditions. These effects can be detrimental to communication and navigation systems, but are also used as helpful remote sensing diagnostics for the characteristics of fundamental plasma processes related to scintillation.

Ionospheric fluid instabilities that are driven by collisional or inertial processes have received a lot of attention recently since they appear to be able to at least partially explain the generation of intermediate-scale plasma density irregularities (e.g., Kintner and Seyler, 1985; Tsunoda, 1988). Of these types of instabilities, the most commonly invoked (for reasons to be discussed below) at high latitudes are the GDI and *Kelvin-Helmholtz instability* (hereafter "KHI"). GDI occurs in situations of inhomogeneity in ionospheric plasma density, specifically in regions where the plasma drift has a component *along the direction of the background density gradient*. In the presence of seed structures, this configuration leads to Pedersen currents that cause charge configurations responsible for the growth of the seed structures. In the nonlinear stage, GDI appears as alternating "fingers" (i.e., elongated structures along the drift direction) of high and low-density and extremely steep-density gradients in these finger-like structures. Whereas GDI depends on Pedersen currents (collisions), KHI is a fundamentally inertial instability that owes its existence, in the context of the ionospheric plasma, to polarization currents. Configurations having a background shear in the plasma drift (e.g., KHI) can be unstable to perturbations in drift which cause polarization currents and charge accumulation that result in the formation of perturbation electric fields and drift which reinforce the perturbations and cause them to grow. In the context of nonlinear growth of fluid instabilities, there is a tendency for structures produced by a primary instability to become susceptible to secondary instabilities, resulting in a *cascade* to different spatial scales. Cascading, the exchange of energy between different unstable modes, and stabilizing processes at small scales (viscous in nature), generally lead to *turbulence*—a term we use in this review to describe a state characterized by a relatively well-defined spectrum of irregularities. More details of these instabilities are further discussed and reviewed in Section 3.2.2.

Plasma instabilities such as GDI and KHI create intermediate-scale sized structures which in turn cause scintillation of transionospheric radio signals. Ionospheric scintillations are more pronounced in the equatorial and high-latitude regions with irregularities responsible for producing scintillations being predominantly in F layer at altitude ranging from 200 to 1000 km and E-layer altitudes from 90 to 120 km regions (Aarons, 1982). In the auroral and polar regions, the dominant factors in the production of the ionospheric irregularities are current systems (causing GDI and KHI) and energetic particle precipitation.

Complimentary to existing reviews of ionospheric scintillation of radio signals (Yeh and Liu, 1982; Aarons, 1982; Bhattacharyya et al., 1992), the purpose of this chapter is to discuss recent progress specifically in the nonlinear simulation of irregularities and scintillation and application of these approaches to the interpretation of radio data. In this section, we first provide a geophysical context to the different types of instabilities followed by a brief survey of relevant review articles on ionospheric irregularities. We then provide a summary of contextual observations used in prior work to establish connections of irregularities and scintillation to larger structures. This is followed by a review of the linear theory of F-region plasma instabilities thought to be the culprit for a large fraction of scintillation at high latitudes (Section 3.2.2). The bulk of the section is devoted to summarizing past and current approaches to nonlinear simulation of plasma instabilities (Section 3.2.3) and review of theory and simulation of radiowave propagation through turbulent and evolving media (Section 3.2.4). We also provide some example simulation codes to help understand basic aspects of the linear and nonlinear theory for GDI and KHI. Finally, we conclude with a summary and specific discussion of future steps required to further nonlinear simulations efforts and their application to extant and future observations.

3.2.1.1 Geophysical context in which instabilities are thought to play a role

Different high-latitude regions and the scintillation-producing instabilities that are typically found in those regions are summarized in Fig. 3.8; this section focuses on scintillation in the cusp, polar cap, and auroral regions labeled on this diagram.

A recent monograph by Zhang and Paxton (2015) presents a comprehensive review of the auroral dynamics and its space weather effects. While GDI is believed to be dominant in the polar cap, it also exists inside structured plasma density enhancements in the auroral oval known as "blobs" (Basu et al., 1990). KHI that develops in strong velocity shear regions can be a prevalent source of the auroral irregularities (Basu et al., 1988). "Hard precipitation" (1–100 keV electrons) results mainly in discrete or diffuse auroras in the E region, whereas low-energy electrons (<1 keV) can generate "soft precipitation" in the F region. Auroras form due to solar wind-magnetosphere and ionosphere interaction during which the precipitating energetic auroral particles collide with the neutrals in the Earth's upper atmosphere (Störmer, 1955). Fig. 3.9A shows an example of an

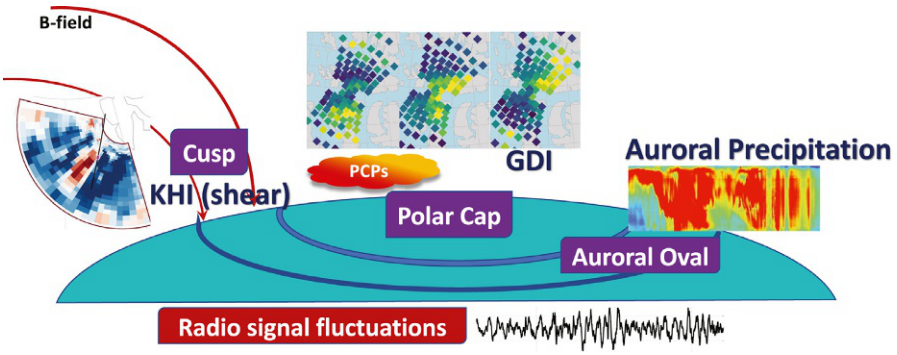

Fig. 3.8 Illustration showing different types of instabilities found in different regions (polar cap, cusp, auroral oval) that can cause scintillation-producing irregularities. The Sun is on the left side of the figure, while midnight is on the right. *Thanks to: Don Hampton (for auroral Image) and Spicher, A., Ilyasov, A.A., Miloch, W.J., Chernyshov, A.A., Clausen, L.B.N., Moen, J.I., Abe, T., Saito, Y., 2016. Reverse flow events and small-scale effects in the cusp ionosphere. J. Geophys. Res. Space Phys. 121 (10), 10466–10480. https://doi.org/10.1002/2016JA022999 (for cusp image).*

auroral arc. The typical boundary of the auroral oval can extend both equatorward and poleward during heightened geomagnetic activity (Aarons, 1997), such as during an auroral substorm (Akasofu, 1968) and geomagnetic storms. The auroral structures due to particle precipitation or formation of different instabilities can result in magnetic field aligned irregularities at different altitudes and can cause scattering of radio waves in HF to UHF range. The reader is referred to a comprehensive review of auroral arcs by Karlsson et al. (2020). In terms of magnetospheric connection, the auroral zone connects to the plasmasheet in the Earth's magnetosphere while cusp connects to the solar wind (Kelley, 2009). Thus, the particles precipitating in the auroral zone are mainly plasmasheet electrons. Although less common, precipitation in the polar cap can also cause sun-aligned arcs or theta aurora (Zhu et al., 1997). An example of such aurora is shown in Fig. 3.9B (adopted from Mailyan et al., 2015). Strong mesoscale flow shears are thought to exist within and around these arcs, which when embedded in a larger polar cap convection pattern could be an important area for instability development (Koustov et al., 2008; Lyons et al., 2016; Robinson et al., 1987; Valladares and Carlson, 1991; Weiss et al., 1993).

Inhomogeneous flows are also common in the cusp region (e.g., Heppner et al., 1993; Moen et al., 2008; Oksavik et al., 2004, 2005; Rinne et al., 2007). One particular cusp phenomenon containing cross-field sheared plasma where electron density irregularities with scales reaching down to tens of meters have been observed is the reversed flow event (RFE) (Moen et al., 2008; Oksavik et al., 2011; Rinne et al., 2007; Spicher et al., 2016). An example of an RFE is shown in Fig. 3.9C. RFEs are longitudinally extended (>400–600 km) but latitudinally narrow (~50–250 km) flow channels with flow direction opposite to that of the large-scale convection background (Rinne et al., 2007). RFEs

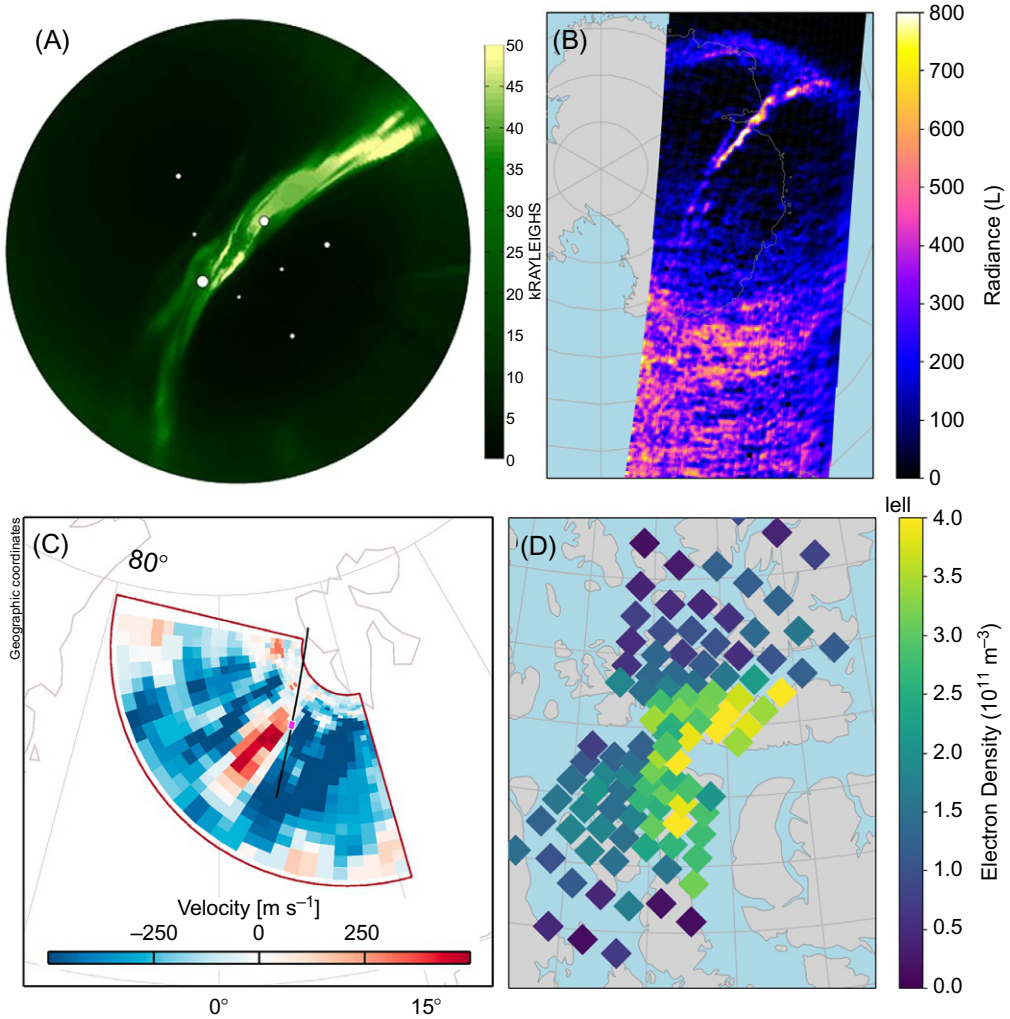

Fig. 3.9 (A) Auroral arc observed by the South Pole All-Sky Imager on August 9, 2010 at 20:37 UT. (B) Sun-aligned arc in the Southern Hemisphere polar cap observed by the Global Ultraviolet Imager (GUVI) on September 27, 2004. (C) Reverse flow event observed by the EISCAT Svalbard Radar on December 3, 2011 at 7:27 UT. (D) Polar cap patch observed by the Resolute Bay Incoherent Scatter Radars North and Canada (RISR-N and RISR-C) on November 21, 2017 at 18:46 UT. *Panel (A): Adapted from Kinrade, J., Mitchell, C.N., Smith, N.D., Ebihara, Y., Weatherwax, A.T., Bust, G.S., 2013. GPS phase scintillation associated with optical auroral emissions: first statistical results from the geographic south pole. J. Geophys. Res. Space Phys. 118 (5), 2490–2502. https://doi.org/10.1002/jgra.50214; Panel B: Adopted from Mailyan, B., Shi, Q.Q., Kullen, A., Maggiolo, R., Zhang, Y., Fear, R.C., Zong, Q.-G., Fu, S.Y., Gou, X.C., Cao, X., Yao, Z.H., Sun, W.J., Wei, Y., Pu, Z.Y., 2015. Transpolar arc observation after solar wind entry into the highlatitude magnetosphere. J. Geophys. Res. Space Phys. 120 (5), 3525–3534. https://doi.org/10.1002/2014JA020912; Panel C: Adapted from Fig. 3 of Spicher, A., Ilyasov, A.A., Miloch, W.J., Chernyshov, A.A., Clausen, L.B.N., Moen, J.I., Abe, T., Saito, Y., 2016. Reverse flow events and small-scale effects in the cusp ionosphere. J. Geophys. Res. Space Phys. 121 (10), 10466–10480. https://doi.org/10.1002/2016JA022999.*

are usually observed around magnetic noon, occurring more often during a dominant B_y IMF, i.e., $|B_y| > |B_z|$, and are believed to be signatures of a flux transfer event (FTE) (Moen et al., 2008; Oksavik et al., 2011; Rinne et al., 2007). Due to RFE, the shears in the velocity perpendicular to the magnetic field can initiate KHI (e.g., Hasegawa, 1975; Keskinen et al., 1988), making them a candidate for the creation of irregularities in the cusp (Basu et al., 1988, 1994; Carlson et al., 2007; Kersley et al., 1988; Keskinen et al., 1988; Moen et al., 2013; Oksavik et al., 2011).

Polar cap patches (Fig. 3.9D) are plasma density enhancements that convect across the polar cap (Crowley, 1996; Weber et al., 1984). Patches form either from dense dayside plasma transported into the polar cap by the background convection pattern or through a localized region of precipitation (Lockwood and Carlson, 1992; Rodger et al., 1994). In addition, the polar cap can also contain plasma depletions known as polar holes (Brinton et al., 1978; Makarevich et al., 2015). In both cases, ionospheric structures create density gradients in the polar cap plasma, on which a variety of instability mechanisms can act and create plasma irregularities. See Section 3.1.1 for more on polar cap patches and depletions.

3.2.1.2 Prior review articles concerning ionospheric irregularities

There are a large number of extant reviews covering various aspects of measurements and theories of ionospheric irregularities and radio scintillation caused by turbulent media. We first discuss reviews on radio propagation and then move to those concerning formation of irregularities. Collectively these reviews on scintillation phenomena and their connection to irregularities suggest use of physics-based scintillation models to understand the connection to cascading mechanisms.

Yeh and Liu (1982) described what has become a standard framework for electromagnetic wave scattering due to ionospheric irregularities. They presented the different spatial scales of density structures associated with phase and amplitude scintillations that fall in the refractive or diffractive regimes. The major contribution to the amplitude fluctuations on the ground comes from the phase front deviations caused by irregularities of the Fresnel scale size $\sqrt{(\lambda H_{iono})}$, where λ is the wavelength of the radio wave and H_{iono} is the height of the ionospheric structures, mainly due to diffractive effects. Irregularities larger than Fresnel scales produce refractive effects and dominate the phase fluctuations. The irregularity spectrum follows a power law form with respect to the wavenumber that suggests the coexistence of intermediate-scale sized irregularities that produce only refractive effects and small irregularities that produce only diffractive effects. In case of weak scattering assumption, a phase screen model can be used to simulate these effects on the radio signals. Such a model treats the irregularity layer at a given height as a slab of limited thickness through which the radio wave propagation may be numerically computed. The problem of radio wave propagation through random media can be solved using the parabolic equation method (PEM) under certain assumptions, such as the

temporal variations of the irregularities are much slower than the wave period, and the characteristic size of the irregularities is much greater than the wavelength and forward scattering assumption. The ionospheric density irregularity can be represented as an electron density distribution obtained from a full physics-based plasma model, a spectral model, or an empirical model. Again, when a radio signal propagates through this irregularity, it experiences signal fluctuations.

Fejer and Kelley (1980) presented both ground-based and in situ measurement techniques, as well as a theoretical framework, developed to study and explain ionospheric plasma irregularities. They discussed E- and F-region irregularities at high and low latitudes, with more detail on equatorial regions where more progresses had been made. For high-latitude F-region irregularities, they grouped the possible sources in three categories: particle precipitation, electrostatic turbulence (spatially varying electric field), and plasma instabilities.

Tsunoda (1988) provided a review of high-latitude F-region ionospheric irregularities with emphasis on fluid interchange instabilities. After introducing some of the density irregularity characteristics such as spectral shapes, scale sizes, and distributions, the author reviewed larger-scale (>10 km) high-latitude plasma structures comprised of polar cap patches, blobs, Sun-aligned arcs, as well as density enhancements and depletions caused by soft particle precipitation and strong electric fields. The author then provided a descriptive model where <10 km structures are created by fluid interchange instabilities acting on the larger-scale density structures mentioned above. The basic properties of interchange instabilities and their linear growth rates are reviewed in detail, especially that of the $\mathbf{E} \times \mathbf{B}$ instability, i.e., GDI, and of the current-convective instability (CCI). Based on evidence from observations, the production of small-scale irregularities seems consistent with the model where GDI plays a dominant role.

A notable past review by Kintner and Seyler (1985) presented a rigorous theory of irregularity formation based on a fluid model of the ionospheric plasma. In this work, they first discussed electrically neutral fluid turbulence within the framework of the Navier-Stokes (N-S) equations and discussed how a classical Kolmogorov (energy-based) approach leads to the identification of a spectrum of turbulence with a $k^{-5/3}$ wavenumber dependence. Ionospheric measurements implying fluid-like behavior were presented and used to motivate their presentation of a fluid model of the ionosphere that includes inertial effects—thus rendering the ionospheric equations in a form similar to the N-S equations used to study neutral turbulence. Kintner and Seyler (1985) included ion inertia, to leading order, via the polarization current, which figures into the current continuity equation (cf. also discussion by Lotko, 2004; Mitchell et al., 1985), while still retaining resistive instabilities (e.g., discussion by Keskinen and Ossakow, 1983). Their formulation naturally describes both gradient and shear-driven instabilities in a single framework and has become the basis for a number of numerical models since developed (e.g., Gondarenko and Guzdar, 2006; Huba et al., 1988; Keskinen et al., 1988; Zettergren

et al., 2015). While Kintner and Seyler (1985) discussed the spectra of plasma fluid turbulence in the context of ionospheric irregularities, they noted that further numerical work is required to fully understand the ionospheric situation.

Wernik et al. (2003) reviewed the connection between ionospheric irregularities and scintillation parameters. For example, the phase scintillation spectrum is related to the shape of the irregularity spectrum. Phase and amplitude scintillations are found to be proportional to the fluctuations in plasma density ΔN_e, which may not follow the distribution of the irregularity amplitude $\Delta N_e/N$ (Kivanç and Heelis, 1998). This causes seasonal variations, for example, nighttime scintillation over auroral oval during the summer is higher than in winter, while polar cap scintillation minimizes in summer due to the rapid decay of convecting irregularities. In cusp and nighttime auroral oval, structures at scales greater than 50 km are created by structured fluxes of precipitating electrons, which may become unstable under certain conditions and cause smaller irregularities due to wave-wave interaction and cascading.

3.2.1.3 Detailed motivating observations: In situ

A significant number of in situ studies have investigated high-latitude F-region irregularities. Density structures ranging from hundreds of kilometers to a few meters have been observed, with power spectral density for scintillation-producing scales (<10 km) commonly obeying power laws (in log-log) with a single spectral slope p or double slopes (e.g., Basu et al., 1988; Dyson et al., 1974; Fremouw et al., 1985; Ivarsen et al., 2019; Kintner and Seyler, 1985; Lagoutte et al., 1992; Mounir et al., 1991; Phelps and Sagalyn, 1976; Singh et al., 1985; Spicher et al., 2014; Tsunoda, 1988; Villain et al., 1986). Irregularity production and decay can affect p, for example, Atmosphere Explorer D satellite's in situ data analysis by Basu et al. (1984) revealed a systematic variation of p with auroral parameters and Ivarsen et al. (2019) showed a correlation between p and solar illumination. The spectral shape of irregularities can thus help in characterizing and classifying plasma structuring processes (e.g., Kintner and Seyler, 1985). It is worth mentioning here that the in situ one-dimensional spectral slopes p may also be of interest with respect to scintillation data, as spectral indices derived from scintillation phase measurements are expected to be steeper by unity compared with p (Tsunoda, 1988, and references herein). For example, a comparison between the slopes of power spectra derived from in situ (sounding rocket) electron density data and ground-based GPS carrier measurements within an RFE showed reasonable agreement with this prediction, suggesting that high-resolution in situ data could in principle be used for modeling GPS scintillations (Jin et al., 2019). In general, the power laws commonly observed seem consistent with fully developed turbulence generated through an instability mechanism responsible for cascading evolution of large-scale irregularities to progressively small-scale irregularities (e.g., Dyson et al., 1974; Kintner and Seyler, 1985; Tsunoda, 1988). The two main classes of macroscale instability mechanisms that have gained significant attention to explain

high-latitude F-region irregularities are GDI and flow shear-driven processes such as KHI.

As discussed in Section 3.2.2.2, the growth rate of GDI has a preferred direction. Consequently, a distinctive feature of GDI is that the resulting structures are expected to develop anisotropically, e.g., with a stable leading edge and a structured trailing edge. Observations of such asymmetries were presented by Cerisier et al. (1985), which commonly (but not consistently) observed different characteristics of density irregularities on both sides of density enhancements, i.e., a stable and an unstable side. The authors also suggested that their observations were consistent with GDI being active as a source mechanism. Asymmetries in the spectral slopes of 1D cuts through patches parallel and perpendicular to the background plasma convection were also discovered by Basu et al. (1990), where the GDI was believed to be operating. Furthermore, Spicher et al. (2015a) and Goodwin et al. (2015) showed in situ measurements of polar cap patches both close to their origin on the dayside, and as they had traveled deeper into the polar cap toward nightside. The latter patches exhibited shorter leading edges consistent with the GDI structuring in the patches as they traveled across the polar cap with significantly more structured and elongated trailing edges. Additional in situ studies based on satellite data (e.g., Lagoutte et al., 1992; Mounir et al., 1991; Singh et al., 1985; Villain et al., 1986) and sounding rocket (Moen et al., 2012; Oksavik et al., 2012; Spicher et al., 2015b) provided further support to the view that high-latitude F-region irregularity creation could be at least partially due to GDI and cascading.

Early sounding rocket (Kelley et al., 1980) and satellite (Mounir et al., 1991) observations suggested that the evolution of irregularities could be significantly different in the polar cap and in the auroral zone. In the polar cap region, the turbulences are related to GDI, while in the auroral region, the major sources of ionospheric irregularity are shears, precipitation, and FACs (Mounir et al., 1991). The importance of velocity shears has also been emphasized for the cusp (e.g., Chernyshov et al., 2018; Heppner et al., 1993; Spicher et al., 2016), and for the auroral oval by, e.g., Basu et al. (1984) and Basu et al. (1988). In particular, Basu et al. (1988) studied the power spectra of electric field and electron density fluctuations coinciding with strong and moderate shears. For moderate shears, the spectra obtained were in agreement with predictions for KHI (Basu et al., 1988; Keskinen et al., 1988), while for the strongly sheared regions where large FACs were also observed, Basu et al. (1988) suggested that other mechanisms such as current-driven ion-cyclotron waves, current-convective or thermal instabilities could contribute (Basu et al., 1988, and references herein). Kelley and Carlson (1977) also presented sounding rocket observation of strong F-region flow shears on the edge of a substorm arc collocated with intense relative plasma perturbations. The authors discussed the observations with respect to flow shear instabilities, including long-wavelength regime KHI.

Despite the significant number of in situ studies providing observations of irregularity structures spanning a wide range of scales down to scintillation-producing scales, the physical sources for their creation are still poorly understood. While generally attributed to GDI and shear-driven KHI, the detailed time-dependent evolution, signatures, and their relative contributions in scintillation are still unresolved and not presently predictable, thus motivating further modeling work of these two macroscale instability mechanisms.

3.2.1.4 Detailed motivating observations: Scintillation

Fluctuations in radio signals, such as those from polar-orbiting satellites, beacons, and GPS and GNSS satellites have been observed at high latitudes for at least five decades. Before that, scientists looked at the sporadic scintillation of radio sources to study the ionosphere (e.g., Briggs, 1964). Although the global scintillation occurrence was well known, the early scintillation observations were mostly from the lower latitudes due to the dearth of high-latitude data (e.g., Aarons, 1982, 1993; Basu et al., 2001; Wernik et al., 2003). With the development of infrastructure in the high latitudes, more scintillation studies have been possible in these regions in recent decades. Multifrequency and multireceiver scintillation observations were used to derive turbulence parameters based on the weak scattering assumptions (Bhattacharyya et al., 1992). Pioneering work on high-latitude scintillation studies on understanding scintillation morphology, plasma structuring during different instability processes over polar cap and auroral regions derived from in situ as well as scintillation measurements is described in Basu et al. (1985, 1988, 1990, 1994, 1998). More recently, presence of ionospheric irregularities responsible for GPS (L-band) scintillation was reported to be associated with E-region particle precipitation (Kinrade et al., 2012) with scintillations occurring close to or on the trailing edge of arcs (Datta-Barua et al., 2015; Mrak et al., 2018; Semeter et al., 2017).

In addition to L-band GPS signals, scintillation has also been observed in the transionospheric UHF and VHF signals (Fremouw et al., 1978; Lamarche et al., 2020). These are typically observed from networks of ground-based receivers that detect signals from beacons transmitting on a variety of LEO satellites (Bernhardt and Siefring, 2006; Siefring et al., 2015). Although these networks are less extensive than the GNSS network, they provide important information about frequency dependence in scintillation.

A significant number of studies examining high-latitude ground-based GNSS data have been performed, comprising statistical analyses (e.g., Alfonsi et al., 2011; Jin et al., 2015, 2018; Kinrade et al., 2013; Meziane et al., 2020; Prikryl et al., 2010, 2011, 2015; Spogli et al., 2009; Spogli et al., 2013) and studies investigating scintillations in different geophysical contexts, including cusp aurora (e.g., Jin et al., 2015; Oksavik et al., 2015), auroral arcs (e.g., Forte et al., 2017; Mrak et al., 2018; Semeter et al., 2017; van der Meeren et al., 2015), polar cap patches (e.g., Jayachandran et al., 2017; Jin et al., 2014, 2016, 2017; Mitchell et al., 2005; van der Meeren et al., 2015; Zhang

et al., 2017a), auroral blobs (e.g., Jin et al., 2014, 2016), the storm-enhanced density and tongue of ionization (e.g., van der Meeren et al., 2014; Wang et al., 2016, 2018), reversed flow events (Jin et al., 2019; Spicher et al., 2020), etc.

At high latitudes, enhanced phase scintillations generally peak in the cusp and in the auroral oval (Aarons, 1997; Jin et al., 2015; Prikryl et al., 2010, 2011, 2015; Spogli et al., 2009), and are associated with polar cap patches/tongue of ionization in the polar caps (e.g., Prikryl et al., 2010). In particular Jin et al. (2017) presented evidence of the combination of polar cap patches and cusp auroral dynamics causing an increased level of phase scintillation. The strongest phase scintillations occur when polar cap patches have entered the nightside auroral oval (thus termed auroral blobs) implying that auroral dynamics including shear and precipitation play an important role in enhancing plasma structuring at phase scintillation scales (Clausen et al., 2016; Jin et al., 2014, 2016). Kersley et al. (1988) also observed strong scintillations and flow shears. While it has been suggested that sun-aligned arcs and associated shears may also cause space weather issues for northward IMF (e.g., Carlson, 2012; Moen et al., 2013), a very limited number of studies exist on the relationship between scintillations and transpolar arcs. For example, van der Meeren et al. (2016) showed weak scintillation and irregularities observed on the nightside of a long-lived transpolar arc.

3.2.2 F-region fluid instabilities: Linear theory

This section summarizes key results from the linear theory of GDI and KHI—instabilities that are believed to play a critical role in high-latitude irregularity formation and scintillation. We do not attempt to provide detailed derivations of how these are obtained (viz containing all algebraic steps), but instead list governing equations, discuss assumptions, and present some key results to be compared against nonlinear simulations in later sections.

Fig. 3.10 shows an illustration of fundamental physical processes responsible for the initiation of GDI. In this diagram, a density perturbation is applied to a background

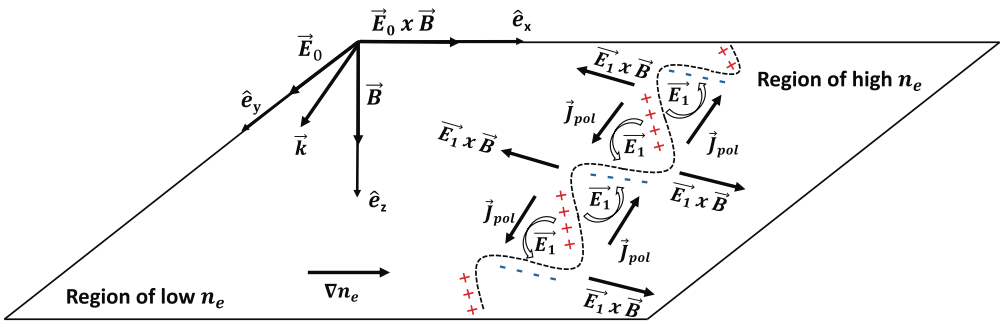

Fig. 3.10 Charge accumulation resulting in gradient-drift instability (GDI).

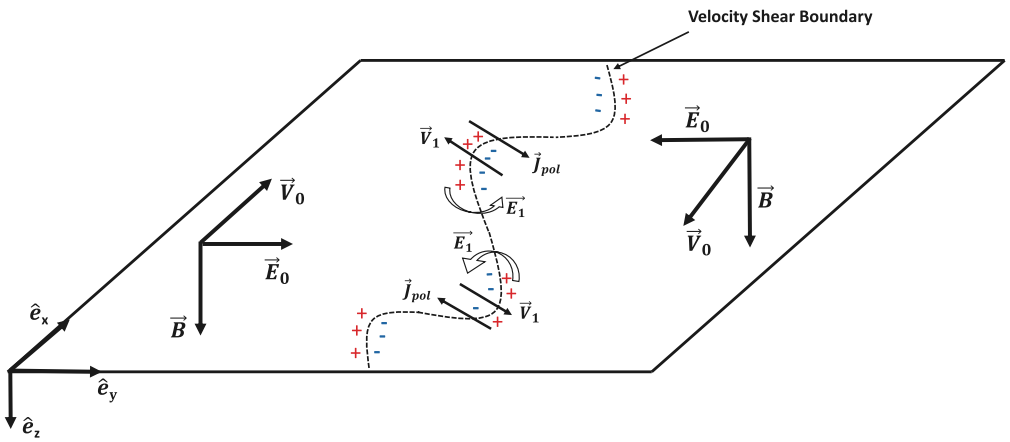

Fig. 3.11 Kelvin-Helmholtz instability (KHI) resulting from a flow shear.

density gradient and subjected to a background electric field. This background field, in the presence of variable ionospheric conductance [density], leads to larger [smaller] Pedersen currents—not shown to reduce visual clutter in the figure—in the high [low]-density region. The divergence [convergence] of this current then results in negative [positive] charge accumulation shown. Perturbation electric fields, $\mathbf{E}_1$ in this diagram, result in $\mathbf{E}_1 \times \mathbf{B}$ drifts that reinforce the seed density perturbations, resulting in unstable growth. This growth can be suppressed by the polarization current (see Section 3.2.2.2) which is proportional to $\partial \mathbf{E}_1/\partial t$ and leads to a partial shorting out of the accumulated charge and a reduction in the response drift and instability growth—note the oppositely directed Pedersen currents (omitted to reduce figure clutter but flowing from the negative to positive charges on the diagram, i.e., they cause these charges to accumulate) and polarization currents in Fig. 3.10.

Ion inertial effects are responsible for destabilizing KHI (Keskinen et al., 1988), which can alternatively be stabilized by conduction currents (collisions). The key ingredient for KHI in the ionosphere is a background plasma velocity shear across a relatively narrow boundary layer. If the component of velocity normal to the boundary layer formed by the shear region $\mathbf{v}_1$ is perturbed, it results in a nonuniform polarization current that causes charge accumulation (Fig. 3.11). The electric field from this charge distribution reinforces the original velocity perturbation and results in the growth of the instability. Pedersen currents can partially short out the charge accumulation from the polarization current and can effectively cause damping of the instability—note, again, the oppositely directed polarization vs Pedersen currents in Fig. 3.11 (not shown but flowing from the positive to negative charges, i.e., they are caused by response fields produced by these charges).

3.2.2.1 Assumptions and governing equations

Instabilities discussed herein are all fundamentally (quasi-)electrostatic in nature—they all involve, at some level, the assumption $\mathbf{E} = -\nabla\Phi$ and the response fields that drive the instabilities that are related to charge accumulation. In this subsection, we will outline linear analysis of these instabilities for conditions representative of the ionospheric F region at high latitudes. First, the plasma will be assumed to drift at the $\mathbf{E} \times \mathbf{B}$ velocity (F region conditions). We also neglect Hall currents (they are very small in the F region) so that the conduction current is given by $\mathbf{J}_c = \sigma_P \mathbf{E}$, where σ_P is the Pedersen conductivity. Depending on the instability and conditions of interest, the ionospheric current density $\mathbf{J}$ will include conduction currents (viz those proportional to conductivity), and (for some analyses) polarization currents (related to ion inertia).

For linear analysis of GDI and KHI, an equipotential field line (EFL) approximation is used; this assumption requires that the electric potential Φ *does not vary along the geomagnetic field lines*. Justification for this is based on the analysis in Farley (1959) and is valid so long as the length scales perpendicular to the field line are not too small ("small" as used here is qualified further in Section 3.2.3.5). The EFL assumption allows equations to be recast in terms of field-integrated plasma quantities like plasma column density ($N(x,y) \equiv \int n(x,y,z)\, dz$, where z is the field line coordinate).

Assumptions outlined above may be combined with the plasma continuity and current continuity equations to produce a system describing the *local* F-region plasma:

$$\frac{\partial n}{\partial t} + \nabla \cdot (n\mathbf{v}) = 0 \tag{3.11}$$

$$\nabla \cdot \mathbf{J} = 0 \tag{3.12}$$

$$\mathbf{v} \approx \frac{\mathbf{E} \times \mathbf{B}}{B^2} \tag{3.13}$$

$$\mathbf{E} = -\nabla\Phi. \tag{3.14}$$

The role of ionospheric conduction (viz collisions) and ion inertia is captured by the particular choice of terms included when computing the current density $\mathbf{J}$—further in Sections 3.2.2.2 and 3.2.2.3.

Eqs. (3.11)–(3.14) can be integrated along the field line (using the EFL assumption) resulting in an analogous set of equations involving column density/conductance; usually we also reduce the system to a set of equations for the N, Φ only by substitution. These equations can then be linearized in the usual fashion by decomposing solutions into the background (N_0, Φ_0) and perturbations (N_1, Φ_1), viz $N = N_0 + N_1$, $\Phi = \Phi_0 + \Phi_1$, and assuming that the perturbations are small so that higher-order nonlinear terms may be neglected.

3.2.2.2 GDI linear theory

Classical linear growth rates for GDI may be derived by considering only the conduction current, viz $\mathbf{J} = \mathbf{J}_c = \sigma_P \mathbf{E}$. The density has a background gradient, here assumed to be in the x-direction $\nabla N_0 = \partial N_0/\partial x\, \hat{\mathbf{e}}_x$ while the background electric field is in the y--direction, $\nabla \Phi_0 = -E_0 \hat{\mathbf{e}}_y$, as shown in Fig. 3.10. Perturbations in column density and potential (N_1, Φ_1) are taken to be proportional to $e^{iky - i\omega t}$,

$$i\omega \tilde{N}_1 + \frac{ik\dfrac{\partial N_0}{\partial x}}{B}\tilde{\Phi}_1 = 0 \tag{3.15}$$

$$N_0 k^2 \tilde{\Phi}_1 + ik\tilde{N}_1 E_0 = 0 \tag{3.16}$$

These may be solved to yield a solution for the frequency:

$$\omega = i\frac{E_0}{\ell B}, \quad \ell \equiv \left(\frac{1}{N_0}\frac{\partial N_0}{\partial x}\right)^{-1}. \tag{3.17}$$

The parameter ℓ here is referred to as the "scale length" of the background gradient. As the frequency is purely imaginary and positive the perturbation grows exponentially in time at a characteristic *growth rate* of

$$\gamma \equiv \Im\{\omega\} = E_0/(\ell B) \tag{3.18}$$

Growth rates for GDI in the presence of ion inertia can be derived by including the polarization current (e.g., Lotko, 2004) in the linear analysis of the instability (Ossakow et al., 1978), in this case we take:

$$\mathbf{J} = \sigma_P \mathbf{E} + c_m\left(\frac{\partial}{\partial t} + \mathbf{v}\cdot\nabla\right)\mathbf{E}, \tag{3.19}$$

where $\mathbf{v} = \mathbf{E} \times \mathbf{B}/B^2$ and c_m is the inertial capacitance defined in (Mitchell et al., 1985):

$$c_m \equiv \frac{\sum_s n_s m_s}{B^2}; \quad C_m \equiv \int c_m(z)dz. \tag{3.20}$$

The z-coordinate here is again used to represent the distance along the geomagnetic field line. Repeating the linearization and Fourier analysis procedure with these assumptions (e.g., Ossakow et al., 1978), and neglecting background drift normal to the density gradient, gives for continuity and current continuity equations:

$$i\omega \tilde{N}_1 + \frac{ik\dfrac{\partial N_0}{\partial x}}{B}\tilde{\Phi}_1 = 0 \tag{3.21}$$

$$-ikE_0\,\widetilde{\nu}\,\tilde{N}_1-\widetilde{\nu}\,k^2N_0\widetilde{\Phi}_1+i\omega k^2N_0\widetilde{\Phi}_1=0 \tag{3.22}$$

Solving this system of equations gives frequencies of

$$\omega=-\frac{1}{2}i\widetilde{\nu}\pm\frac{1}{2}i\sqrt{\widetilde{\nu}^2+4\,\widetilde{\nu}\,\frac{E_0}{\ell B}}, \tag{3.23}$$

where $\widetilde{\nu}\equiv\Sigma_P/C_m$ is the ratio of Pedersen conductance to integrated inertial capacitance. The largest growth rate corresponds to the positive root in this equation, and represents the growth rate for GDI in the presence of ion inertial effects.

Two limiting cases of interest for GDI with inertial growth are the small inertia limit ($\widetilde{\nu}\gg1$), in which the growth rate implied by Eq. (3.23) reduces to that already given in Eq. (3.17). Alternatively, in the inertia-dominated case $\widetilde{\nu}\ll1$, we have a frequency that is, to the leading order:

$$\omega=i\sqrt{\widetilde{\nu}}\frac{E_0}{\ell B}\approx i\sqrt{\nu_s\frac{E_0}{\ell B}}, \tag{3.24}$$

where ν_s is the ion-neutral collision frequency. From Eq. (3.24) dependence of the growth rate on ion inertia (characterized by the inertial capacitance parameter) can be written as

$$\mathcal{I}\{\omega\}=\sqrt{\frac{\Sigma_P}{C_m}\frac{E_0}{\ell B}}\propto C_m^{-1/2} \tag{3.25}$$

This expression clearly shows that increasing the value of the integrated capacitance (i.e., representing an increased importance for ion inertia) works to reduce the linear growth of GDI.

The simplified treatment of linear GDI shown above assumes a specific altitude regime and geometry of the background gradient and drift velocity vectors—namely that they are parallel. Although this is useful for a theoretical understanding, contemporary work has made significant progress in defining dispersion relations that are valid in a wide range of altitudes for arbitrary vector orientations and can describe the Farley-Buneman and current-convective plasma instabilities along with GDI in a single theoretical formulation (Makarevich, 2014, 2016a, b, 2019). For the specific case of long-wavelength GDI in the F region, the following growth rate expression can be extracted from the generalized treatment of Makarevich (2019)

$$\gamma=-\frac{1}{k_\perp^2}\left(\frac{\nabla n}{n}\cdot\mathbf{k}\times\hat{\mathbf{e}}_B\right)\left(\frac{\nu_i}{\Omega_i}\mathbf{v}-\frac{\mathbf{E}_\perp}{B}\right)\cdot\mathbf{k} \tag{3.26}$$

Because no particular relative orientation of the density gradient, electric field, and wave propagation direction is assumed, all these quantities must be expressed as vectors ($\nabla n/n$, $\mathbf{E}$, and $\mathbf{k}$, respectively). The unit vector $\hat{\mathbf{e}}_B$ is in the direction of the geomagnetic

field, viz the $\hat{\mathbf{e}}_z$-direction in our diagrams of Fig. 3.10, and ν_s and Ω_s are the ion collision and gyrofrequencies, respectively. Under the assumption $\mathbf{k} \perp \mathbf{B} \perp \mathbf{v} \parallel \nabla n$, this expression simplifies to Eq. (3.18). The generalized GDI growth rates depend not only on the relative directions and magnitudes of the density gradient and electric field but also the propagation direction of the wave (Keskinen and Ossakow, 1981; Makarevich, 2014). The $1/k_\perp^2$ factor effectively normalizes the perpendicular components of both $\mathbf{k}$ vectors in the expression such that the growth rate depends on the perpendicular direction of the wavevector but not its magnitude, indicating that GDI causes structures to grow preferentially in a particular direction, but uniformly across all scales (Makarevich, 2014).

The plasma structures resulting from GDI are then anisotropic, evidenced by the characteristic "fingers" that grow perpendicular to a density enhancement's trailing edge (Deshpande and Zettergren, 2019; Gondarenko and Guzdar, 2004b; Hosokawa et al., 2016). This is not the same effect as the leading/trailing edge asymmetry that is often discussed with GDI acting on polar cap patches (Lamarche and Makarevich, 2017). If the gradient and plasma drift velocity are antiparallel (such as the leading edge of a patch), there are almost no wavevector directions that result in a positive growth rate, while if they are parallel (trailing edge of a patch) the growth rate is almost always positive. Hence, GDI tends to be active on the trailing edge and suppressed on the leading edge, which explains many observations of small-scale structuring primarily on the trailing edge of patches (asymmetry) (Hosokawa et al., 2013, 2016; Milan et al., 2002; Moen et al., 2012; Weber et al., 1984). This has also been discussed in Section 3.1.1. The fact that the GDI growth rate is wavevector-dependent further predicts that the trailing edge structuring will form preferentially in a particular direction (anisotropy).

3.2.2.3 Linear KHI in the ionosphere

KHI occurs in the presence of shear plasma flows; typically analysis will assume either a sharp (infinitesimal) boundary, in which case the problem may be treated analytically (cf. Keskinen et al., 1988, Appendix A) or a far more realistic smooth drift profile, which then requires a numerical solution of the resulting linear system of differential equations (e.g. Berlok and Pfrommer, 2019) as discussed further below. The instability growth is a function of the ratio of Pedersen conductance to inertial capacitance $\tilde{\nu} \equiv \Sigma_P / C_m$ and also of the scale length of the shear layer ℓ, often parameterized through a hyperbolic tangent profile, in this article we take:

$$\nu_x(y) = \nu_0 \tanh\left(\frac{y}{\ell}\right) - \nu_n \tag{3.27}$$

A starting, equilibrium state for KHI (needed for the linear analysis) requires additional assumptions. Particularly the steady-state current continuity equation $\nabla \cdot \mathbf{J} = 0$ must hold for a straightforward analysis, which means that the plasma velocity profile

(i.e., variation with the y-direction) should be asymmetric in the neutral atmosphere frame of reference (or equivalently there must be a nonzero neutral wind in the frame where the plasma velocity profile is symmetric). This is required to balance the divergent Pedersen current implied by a symmetric electric field configuration. Because of this the neutral wind required (in the frame where the plasma velocity is symmetric) is uniquely determined by the choice of plasma velocity amplitude v_0 and density jump across the shear layer (Keskinen et al., 1988) given by

$$\frac{\lim_{y\to\infty} n(y)}{\lim_{y\to-\infty} n(y)}. \tag{3.28}$$

For linear KHI analysis, the full current density given by Eq. (3.19) is required. The geometry for ionospheric KHI is fundamentally different from the GDI cases considered to this point; here we suppose a background state where (see also Fig. 3.11):

$$\nabla_\perp N_0 = \frac{\partial N_0}{\partial y}\hat{\mathbf{e}}_y; \quad \nabla_\perp \Phi_0 = \frac{\partial \Phi_0}{\partial y}\hat{\mathbf{e}}_y = -E_0\hat{\mathbf{e}}_y, \tag{3.29}$$

and for our linear perturbation analysis, we must allow the perturbed quantities to vary continuously in the y-direction and harmonically in the x-direction:

$$\Phi_1(x,y,t) = \Re\left\{\tilde{\Phi}_1(y)e^{ikx-i\omega t}\right\}; \quad N_1(x,y,t) = \Re\left\{\tilde{N}_1(y)e^{ikx-i\omega t}\right\}, \tag{3.30}$$

The algebra is substantial but linearizing the plasma continuity and current continuity equations and plugging in these perturbations yields a system of ordinary differential equations (viz an eigenvalue problem) to be solved.

$$(\omega - kv_0)\tilde{N}_1 - k\frac{1}{B}\frac{\partial N_0}{\partial y}\tilde{\Phi}_1 = 0 \tag{3.31}$$

$$\left[\frac{\partial}{\partial y}\left(\frac{N_0\partial\tilde{\Phi}_1}{\partial y}\right) - k^2 N_0\tilde{\Phi}_1\right](\omega - kv_0 + i\tilde{\nu}) + i\tilde{\nu}(v_n - v_0)BN_0\frac{\partial}{\partial y}\left(\frac{\tilde{N}_1}{N_0}\right) + k\tilde{\Phi}_1\frac{\partial}{\partial y}\left(N_0\frac{\partial v_0}{\partial y}\right) = 0. \tag{3.32}$$

where, as in prior equations, $v_0 \equiv E/B$, and v_n is the neutral wind velocity. This eigenvalue problem must be solved numerically for the growth rates—e.g., the values of ω for which these equations are valid in the nontrivial sense $\tilde{N}_1, \tilde{\Phi}_1 \neq 0$ and the corresponding eigenfunctions (solutions $\tilde{N}_1$, $\tilde{\Phi}_1$ corresponding to "allowable" values of frequency).

An example of growth rate solutions by this method from Keskinen et al. (1988) is shown in Fig. 3.12. Note that this figure is a reproduction and differs in the notation for the rest of this article; these may be translated as $L \equiv \ell$ and $\nu \equiv \tilde{\nu}$. As shown in this result,

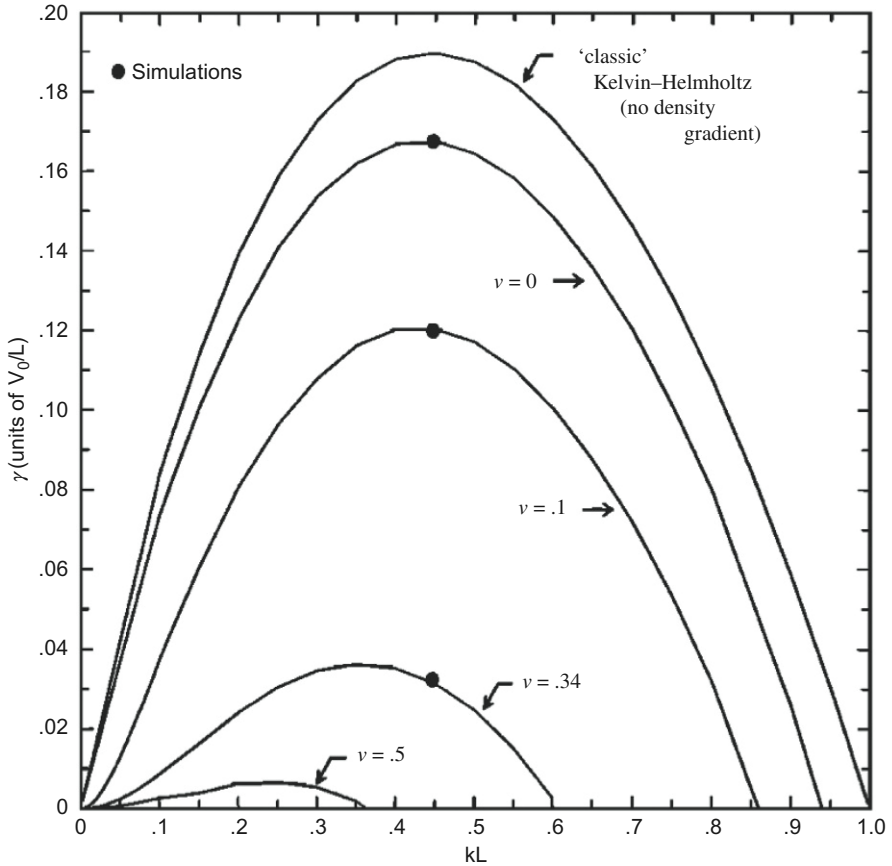

Fig. 3.12 KHI linear growth rate solutions. For purposes of comparing to the rest of this article note that $L \equiv \ell$ and $\nu \equiv \widetilde{\nu}$. *Reprinted from Keskinen, M.J., Mitchell, H.G., Fedder, J.A., Satyanarayana, P., Zalesak, S. T., Huba, J.D., 1988. Nonlinear evolution of the Kelvin-Helmholtz instability in the high-latitude ionosphere. J. Geophys. Res. Space Phys. 93 (A1), 137–152.*

the maximum growth rates occur for modes having $k\ell \approx 0.4 - 0.5$, such that the *fastest growing* mode has wavelength $\lambda \approx 2\pi\ell/0.44$. Fig. 3.12 also shows that the particular value for the growth rate at this maximum is strongly dependent on the parameter $\widetilde{\nu}$ (the ratio of conductance to capacitance)—generally larger values of this parameter result in more damping via Pedersen currents, which "short out" KHI, and decrease overall growth rate.

3.2.2.4 Applications of linear theory

As outlined in Sections 3.2.2.2 and 3.2.2.3, relatively simple expressions can be obtained for the growth rates of GDI and KHI using linear theory, subject to certain assumptions.

These growth rates depend only on a few parameters, which can be measured both from the ground or in situ. Thus, several studies have applied results from linear theory to observations to evaluate the role of different instability mechanisms in producing irregularities.

To explain the presence of strong HF backscatter echoes in the cusp due to decameter-scale irregularities, Moen et al. (2002) combined tomographic images based on TEC and line-of-sight velocity measurements from the CUTLASS Finland radar and estimated the linear growth rate of GDI (using Eq. 3.17). They found that irregularities would develop within 12 min due to GDI acting on the large-scale gradient. They suggested that particle precipitation could act as the primary mechanism, or that GDI could occur on intermediate-scale-sized structures. Later, Carlson et al. (2007, 2008) proposed a framework where the KHI would initialize plasma structuring of polar cap patches as they transit through the cusp entry region, providing seed irregularities enabling GDI to develop faster as a secondary mechanism. Using the fastest growing mode (based on Keskinen et al., 1988), they estimated KHI to have a growth time of about 50 s. Consistent values of KHI growth times were then calculated by Oksavik et al. (2011) using SuperDARN HF data observations of RFEs. Later, Moen et al. (2012) used high-resolution electron density data from the Investigation of Cusp Irregularities-2 (ICI-2) sounding rocket to estimate the growth time for GDI on the trailing edge of a density enhancement in the cusp. Using Eq. (3.17), they found a value of 47.6 s, and suggested that the growth time could be as fast as about 10 s, which is 50–70 times faster than previously estimated (Moen et al., 2002). Similar growth times were then reported using data from the Swarm satellites (Spicher et al., 2015a). Additionally, also using ICI-2 data, Oksavik et al. (2012) investigated in detail the minimum linear growth times of GDI and KHI to assess which mechanism would grow faster and at what scales. The authors found shorter growth times for GDI than for KHI for most of the flights, suggesting that GDI would be dominating over KHI during that event.

Also based on in situ measurements, Burston et al. (2016) used DE-2 satellite data to compare the linear growth rates of GDI, CCI, KHI, and "stirring" (defined in Section 3.2.3.7), in both the inertial and collisional regimes. Note that the authors used the word turbulence instead of stirring (Burston et al., 2016; Kelley, 2009), but we here opt for the latter name to avoid confusion with turbulence generated from primary ionospheric instabilities. Based on the linear growth rates, they found inertial stirring to be dominant, followed by inertial GDI. The authors also showed that these two processes and the collisional CCI can regularly grow within timescales shorter than 60 s in the linear regime, while the KHI did not meet the instability condition in any of their cases. It is worth mentioning that Burston et al. (2016) used a different KHI growth rate compared to Oksavik et al. (2012).

Burston et al. (2009) also made use of linear theory and estimated the amplitude of GDI waves with the help of ionospheric imaging reconstruction (MIDAS 2.0) for

13 days during magnetic storms. The authors used Eq. (3.24) and assumed that the amplitude of GDI waves were proportional to $\exp \gamma t$, where t is the time. Burston et al. (2009) were able to estimate GDI growth rates γ for the entire part of the reconstructed ionosphere at each time step, to calculate how the GDI wave amplitude varied with time, and to correlate their calculations with scintillation indices recorded at several stations. They found weak but statistically significant correlation between the scintillation indices and the GDI mechanism for causing irregularities during storm time. Burston et al. (2010) then used the same method to correlate scintillation indices with the amplitude of waves caused by GDI and by stirring, and found in general a better correlation for GDI.

Several studies have also evaluated the GDI growth rates based on remote sensing imaging (Incoherent Scatter Radar (ISR) and All-Sky Imager (ASI)) techniques. Hosokawa et al. (2013) estimated growth rates on the order of 10^{-1} s^{-1}–10^{-2} s^{-1} while Lamarche and Makarevich (2017) and Lamarche et al. (2020) found rates on the order of 10^{-2} s^{-1}–10^{-4} s^{-1} using measured gradient and velocity magnitude and directions. In general, these studies found that qualitatively linear growth rates often agree with measurements where plasma irregularity observations occur, but as for the studies based on in situ observations, it is challenging to use them to fully explain the irregularity evolution, especially when the instability is in the nonlinear stage or likely to be part of a complex structuring process.

One important factor to take into account when interpreting the results from different observational studies is the inherent limitations of different observational techniques. In general, in situ instruments on sounding rockets will have the highest spatial and temporal resolution, followed by those on satellites (although both suffer from space-time ambiguity issues), with ground-based remote sensing instruments like ISRs or ASIs having the lowest resolution, but largest region of coverage. The spatial resolution of a particular measurement technique controls the level of detail at which the structuring can be measured, which in turn impacts the gradients and shears measured and the resulting linear growth rates. This may help explain why the growth rates derived from the ICI-2 sounding rocket Langmuir probe (Moen et al., 2012) are an order of magnitude greater than those estimated from ISR densities (Lamarche and Makarevich, 2017). It is also important to remember that satellites and sounding rockets typically measure a 1D slice through the density structure, and unless this slice is perpendicular to the edge of the structure it will underestimate the steepness of the edge gradient. Finally, we note that the impact of the neutral dynamics has generally been omitted for observation-based linear growth rate calculations.

These issues highlight the fact that the edges of large-scale irregularities are likely to be quite complex, with smaller density perturbations overlying larger background gradients. It is not clear whether it is appropriate to apply linear growth rates to the steeper perturbation gradients, the large-scale edge gradient, or both. Nonlinear modeling can help address how structuring develops on an arbitrary superposition of structures at a variety

of scales, but only if the model is initialized with a realistic spectrum of structures. Measuring details of the spectrum of ionospheric seed structures on which instability mechanisms act as key to advancing our understanding of how instabilities evolve.

3.2.2.5 Diffusive stabilization at small scales

At the smallest scales we consider (likely below ~100 m), pressure effects like diamagnetic drift and cross-field diffusion may become significant. Diamagnetic drifts lead to additional flows to be considered, while at F region and lower altitudes, where collisions are frequent, charged particles can also diffuse across geomagnetic field lines (e.g., Kelley, 2009). Ions are less magnetized than electrons and so are more able to diffuse across geomagnetic field lines. This can lead to charge separation and a *perpendicular* ambipolar electric field that will generally act to suppress further diffusion. As a consequence of these processes, encapsulating small-scales requires incorporating pressure terms self-consistently into both drift equations and electromagnetic solutions. Most models of GDI and KHI, to date, have not fully incorporated pressure effects (Zettergren et al., 2015) or have been run at resolutions where they are not the dominant contributor to irregularity evolution (e.g., Gondarenko and Guzdar, 2006; Huba et al., 1988, and related studies).

One may approximate the scale at which plasma pressure effects become substantial via examination of the diamagnetic drift expression (e.g., Schunk and Nagy, 2009). Typical plasma drifts in GDI or KHI unstable situations are likely to be in the 250–1000 m/s range, roughly corresponding to 12.5–50 mV/m electric fields. Using representative plasma parameters, one needs approximately a ~10 m scale length to generate the diamagnetic drift equally as strong as the drift generated by a 12.5 mV/m electric field. This suggests that diamagnetic drift effects can be safely ignored for all but the smallest irregularities considered in the ionosphere.

In addition to diamagnetic effects, one must also consider cross-field diffusion. A generic diffusion equation (derived under assumptions of constant diffusion rate, for the sake of simplicity and illustration) describing F-region plasma transport may be written in the following form.

$$\frac{\partial n}{\partial t} + D\frac{\partial^2 n}{\partial x^2} = 0; \quad n(x,t) = \int_{-\infty}^{\infty} A(k) e^{-k^2 D t} e^{ikx}\, dk \tag{3.33}$$

where, D is the *diffusion coefficient*, and the solution for density n is written for the case of an unbounded domain with density decaying to zero at infinity. This shows that a single spatial mode with wavenumber k decays exponentially at a rate given by

$$k^2 D = \frac{4\pi^2 D}{\lambda^2} \tag{3.34}$$

showing the well-known fact that small-scale modes decay faster. If the instability growth rate, γ, is known (for either GDI, KHI, or some other mechanism), the net irregularity growth/decay rate in the linear regime is $\gamma - k^2 D$ (Keskinen and Ossakow, 1981). By setting this net growth/decay rate to zero and solving for λ, we can identify a critical scale, above which the growth rate is larger than the decay rate (and irregularities will grow) and below which the decay rate is larger than the growth rate (and irregularities will dissipate) (Lamarche et al., 2020). For a scale-independent growth rate (such as GDI without ion inertial effects, Section 3.2.2.2), this calculation is straightforward.

$$\frac{E}{\ell B} - \frac{4\pi^2 D}{\lambda^2} = 0 \Longrightarrow \lambda = 2\pi\sqrt{\frac{D\ell B}{E}} \tag{3.35}$$

The critical scale, λ, can be interpreted as the minimum scale at which GDI growth will occur under given conditions. As the growth rate ($E/\ell B$) increases, small-scale structures may move from the diffusion regime into the growth regime (cf. Lamarche et al., 2020, Fig. 12).

The appropriate form of the diffusion coefficient, D, depends on the background conditions of interest, particularly the particle collision frequencies. In the F region, the ion diffusion coefficient for motion across the geomagnetic field is given by (Kelley, 2009; Perkins et al., 1973):

$$D = \frac{\nu_{ths}^2 \nu_s}{\nu_s^2 + \Omega_s^2} \tag{3.36}$$

where $\nu_{ths} = \sqrt{k_B T_s / m_s}$ is the ion thermal speed and ν_s and Ω_s are the ion-neutral collision and ion gyrofrequencies, respectively. The diffusion coefficient is dependent on which modalities of cross-field transport are considered to be important, so variations on the above expression can be found in the literature. For example, a robust E-region will have a significant impact on diffusion through E-region shorting (e.g., Vickrey and Kelley, 1982). This is a nonlocal effect (discussed in Section 3.2.3.5) and is challenging to quantify in linear interpretations because it requires knowledge of the plasma conductance along the entire field line (viz it is inherently nonlocal).

3.2.3 Simulating ionospheric F-region instability and turbulence: A nonlinear modeling tutorial

Linear theory presented in Section 3.2.2, while useful for a wide range of studies discussed in Section 3.2.2.4, does not address mid- or late-stage development of irregularities—an essential aspect relevant to the resulting scintillation of radio signals as they pass through those irregularities. This section presents nonlinear aspects of ionospheric instability behavior within a framework of numerical simulation studies both past and current. For the recent modeling results presented, we include links to source code for

demonstration simulations so the readers may reproduce, modify, and study these demos or use them for their own instability-related research.

3.2.3.1 Summary of nonlinear modeling approaches

Various nonlinear ionospheric models of GDI and KHI, which incorporate ion inertia effects, have been developed and applied in prior work to study mid-to-late-stage evolution of the instabilities. While ultimately limited in resolution, these models have served to illustrate important aspects of irregularities not apparent from the linear theory. Here we focus specifically on more recent models that have incorporated ion inertia, e.g., in the manner introduced by Kintner and Seyler (1985).

Mitchell et al. (1985) simulated high-latitude F-region GDI with a two dimensional model (the plane perpendicular to the geomagnetic field) that included both polarization and Pedersen currents. This model included ionospheric and magnetospheric slabs and was used to show the relative effects of polarization drifts on the initiation and evolution of GDI, generally showing that the polarization drifts slow progression of the instability and lead to strong large-wavelength features in the nonlinear stage. Keskinen et al. (1988) applied the same model to study linear and nonlinear evolution of KHI under conditions of strong background plasma flow shears. Their analysis of the linear stage of KHI was used to derive growth rates for the instability under various shear conditions and was critically compared against nonlinear simulations for purposes of validation. Work by Huba et al. (1988) synthesized these nonlinear studies to demonstrate roles of polarization current as a stabilizing mechanism for GDI and Pedersen currents as a stabilizing mechanism for KHI while suggesting likely appropriateness of slab models of these instabilities for km-scale structures, i.e., the EFL assumption is appropriate for such structures. Ganguli et al. (1994) examined the interplay between fluid-scale and microscale processes in shear instabilities and parameterized microinstability effects into their fluid model of KHI via an anomalous viscosity in the model.

Three-dimensional, nonlinear studies of the role of GDI in structuring plasma patches have sought to explain various observed aspects of the progression rate of the instability. Guzdar et al. (1998) focused on effects of including field line resolved dynamics on the growth of the instability compared to prior 2D, slab modeling efforts. These studies were later extended by Gondarenko and Guzdar (1999) to include effects of ion inertia, which was shown to slow the growth of irregularities, similar to prior studies, and led to the suggestion that the persistence of polar cap patches could be a consequence of slowed growth due to parallel to B (shorting) and inertial effects. Results from this model were compared against data from the DE satellites (Gondarenko and Guzdar, 2004a, b)—reasonable agreement further indicated that GDI was a likely source of the polar cap irregularities, and that ion inertia played a key role in secondary instabilities (e.g., KHI) and nonlinear evolution of GDI. Effects of variable magnetospheric electric field (including field reversals) (Gondarenko et al., 2003) on the development of irregularities

have illustrated the important role of time-dependent forcing (elsewhere referred to as "stirring") on the character of density structures. Further work using the same models explored mixed-mode instability development due to the combined presence of flow shears on the leading edge of a polar cap patch and unstable density gradients on the trailing edge (Gondarenko and Guzdar, 2006)—in particular, these studies have suggested a mode through which the density irregularities can be isotropized as compared to GDI acting alone (which overwhelmingly favors anisotropic development of plasma structures).

Most recent modeling efforts have examined the behavior of GDI and KHI under a range of data-inspired conditions and have self-consistently included thermodynamic and chemical effects on the development of these high-latitude instabilities. Simulations by Zettergren et al. (2015) have investigated plasma depletion processes, resulting from strong frictional heating of the ionosphere and chemical alterations (e.g., Zettergren and Semeter, 2012, and references therein), as a potential source for unstable density gradients. They show that the cavity formation process critically affects the character of subsequent instability, particularly during nonlinear development. Deshpande and Zettergren (2019) coupled the Zettergren et al. (2015) model of plasma instabilities (subsequently named GEMINI: Geospace Environment Model of Ion-Neutral Interactions) to the SIGMA (Satellite-beacon Ionospheric-scintillation Global Model of the upper Atmosphere) model of radio propagation (Deshpande et al., 2014) to demonstrate that GDI unstable polar cap patches cause scintillation of a character similar to observed GNSS data from Resolute Bay, Canada. They have further suggested the possible use of their full physics-based toolchain for studying specific plasma processes resulting in L-band scintillation. This GEMINI-SIGMA toolchain has also been used to study KHI generated by polar cusp flow shears by Spicher et al. (2020). They showed that shear-flow conditions observed from the EISCAT Svalbard Radar (ESR) and DMSP were capable of producing ionospheric KHI and that scintillation modeled from KHI irregularities was reminiscent of observations from the Svalbard GPS network.

3.2.3.2 GDI simulations: Comparisons against linear theory and basic nonlinear features

Before discussing nonlinear features of the model results, we first compare GDI simulations against the linear growth rates presented in Sections 3.2.2.2 and 3.2.2.3 for three different cases (a) classical GDI (no inertia), (b) GDI with ionospheric inertial effects, and (c) GDI with a magnetospheric capacitance added (conceptually this can be understood as including a magnetospheric slab in calculations of capacitance along with the ionospheric contribution). These comparisons are summarized in Fig. 3.13 and can be compared against growth rates from Section 3.2.2.2. In order to compare the simulations against the linear theory, we extract plasma density along a line in the vertical (y) direction at the center of the region containing the unstable gradient. Because this region moves

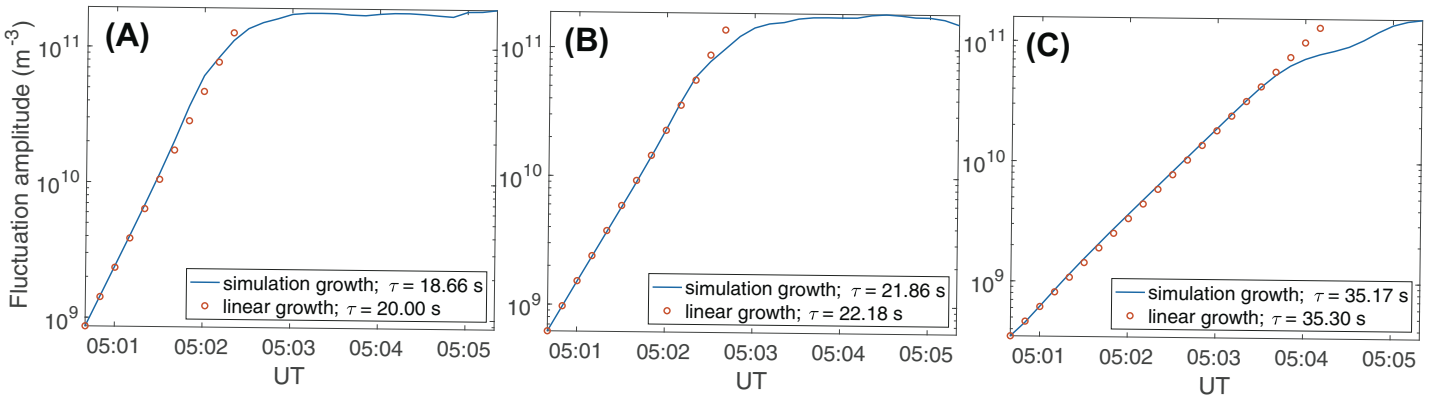

Fig. 3.13 A comparison of linear growth times $\tau \equiv 1/\gamma$ vs nonlinear simulation for gradient-drift instability. (A) Without ion inertia, (B) with ionospheric inertia, and (C) with an added magnetospheric capacitance.

with time, the location where the line is taken must be different at each time step in the simulation. Fluctuations due to the instability are separated from the background by subtracting off the mean density along the extracted line and then a standard deviation of the background-subtracted fluctuations is used to define the amplitude of the fluctuations along the line as a function of time. Perturbation amplitudes are plotted in Fig. 3.13 alongside a pure exponential function computed from the linear growth rate and density following initial settling in the simulation (settling appears as a brief, initial decay in noise due to the arbitrary perturbations imposed at the beginning).

All three simulations match the linear theory quite well during the initial stage of growth. Comparisons show clear deviations near saturation when the amplitude of the fluctuations is no longer growing strongly—following 5:02 UT in panel (A); following 5:02:30 UT in panel (B); and following 5:03:30 UT in panel (C).

Fig. 3.14 shows different example simulations including (A) the initial state for each example simulation, (B) classical GDI (no inertia), (C) GDI with ionospheric inertial effects, and (E) GDI with a magnetospheric capacitance added. Additionally, a simulation containing a more robust E region was included to illustrate the effects of a higher conductivity on the development of the instability in (D).

From Fig. 3.14 it is clear that the physical processes included in the simulation, viz inertia, MI-coupling, and E-region conductance, greatly impact the character of the resulting density structures. Comparison of panels (B) and (C) show that the inclusion of ionospheric inertia has the effect of slightly slowing the growth of the instability (also evident in Fig. 3.13) and that the plasma density structures have a slightly larger (y) extent and tend to be somewhat less narrow than those computed without ionospheric inertia (cf. Huba et al., 1988). Inclusion of stronger E-region (generated from an energy flux of $0.05\ \mathrm{mW/m^2}$ electron precipitation) creates a shorting pathway for the charge and greatly suppresses the growth of structures as shown in panel (D). Finally, panel (E) demonstrates that a large magnetospheric capacitance (30 F in this case) can also greatly slow the growth of the instability.

3.2.3.3 KHI simulations: Comparisons against linear theory and basic nonlinear features

KHI growth is wavenumber dependent (see Section 3.2.2.3) so if the instability is seeded from noise one may, in principle, expect a range of wavelengths to visibly appear as the instability passes through the linear stage. In practice, however, we find that the fastest growing mode fairly clearly (at least visually) dominates the linear and early nonlinear evolution of the instability such that one does not need to be too careful about the seeding specific wavenumbers of interest.

For our cursory comparisons against linear theory, we initialize our simulations with white noise perturbations in density. Because these are not accompanied by potential perturbations defined through Eq. (3.31) some settling in the simulation will occur while the

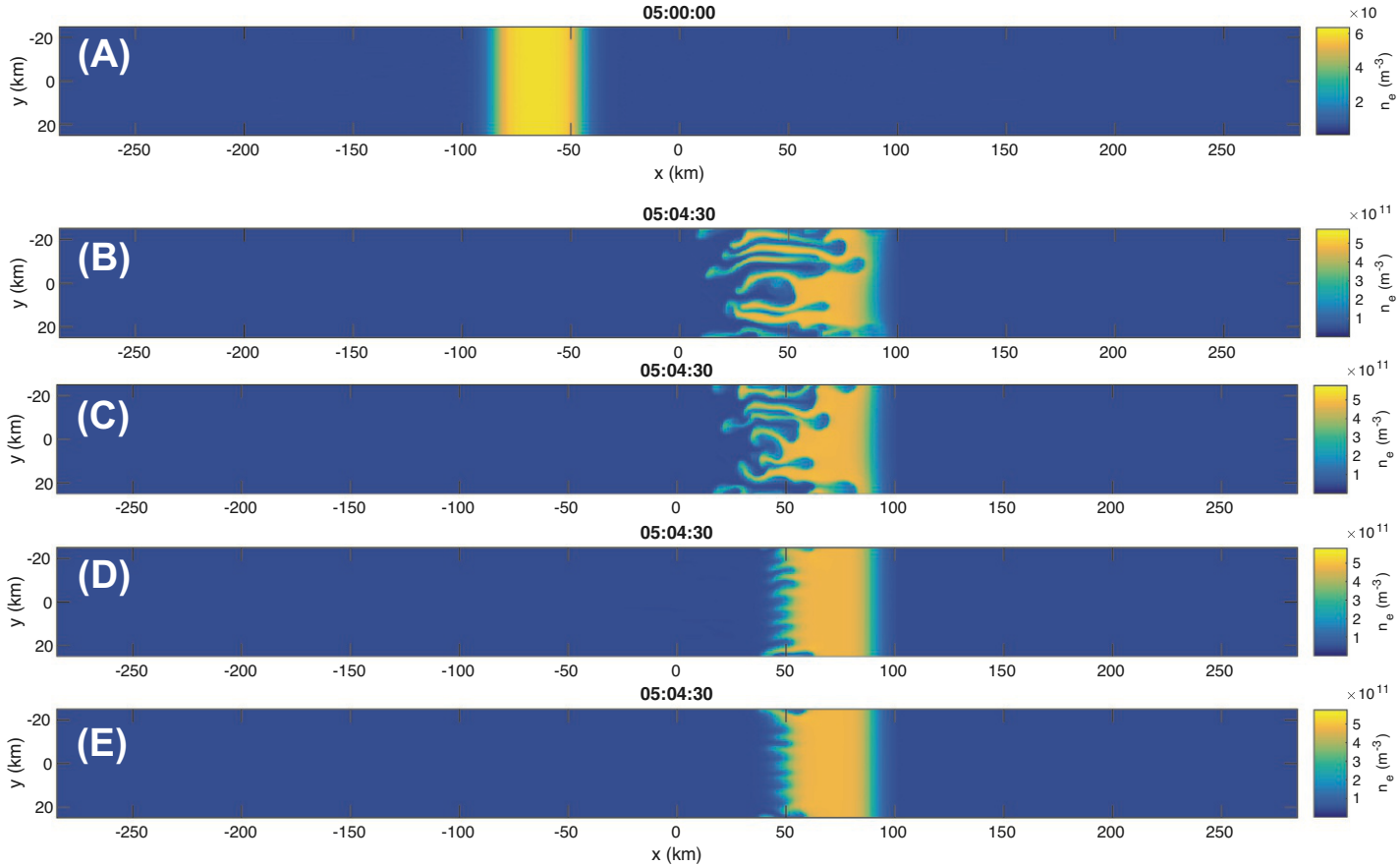

Fig. 3.14 Plasma density snapshots at 300 km altitude taken from various GEMINI simulations of GDI. (A) Initial state for all simulations, (B) simulation without ion inertia, (C) simulation with ionospheric inertia included, (D) simulation with modest E-region conductivity, and (E) simulation with a magnetospheric capacitance added.

simulation established a density/potential configuration consistent with this equation, which will then be destabilize. This process of seeding the simulation is obviously suboptimal as comparisons with the linear theory must occur after the initial settling. The relatively large capacitance used in KHI simulations, i.e., the time constant for the simulation to settle into a consistent potential perturbation, is long enough for this to require more than a minute in our simulations. One proper solution to the issue of providing consistent seed to the nonlinear simulation would be to solve the eigenvalue problem encoded in Eqs. (3.31) and (3.32) for the eigenvalues and eigenfunctions and use these to define inputs for both density and potential perturbations. While more elegant, this approach requires a substantial set of additional software in order to be used, so we instead use the noise-seeded approach with the caveat that we can only sensibly compare to the linear theory after some settling has occurred.

When doing KHI simulations, in particular, one must be careful to properly observe background equilibrium conditions and grid size. One must be careful that the fastest growing mode that is a harmonic of the grid size in the periodic direction; otherwise, spatial aliasing of the instability growth could occur. Finally, one must take care, when comparing with linear theory, to initialize the simulation background state in a manner that corresponds to the balanced state consistent with that defined by Keskinen et al. (1988). To do otherwise will cause the simulation to again experience a settling process in which an equilibrium is first reached before instability growth occurs.

Example simulations included in this article use a background state corresponding to boundary layer width $\boldsymbol{\ell} = 3.15$ km; this results in the fastest growth mode of ~45 km according to the linear theory shown in Fig. 3.12 (Keskinen et al., 1988). The velocity shear for our simulations is set by the parameter $v_0 = -500$ m/s, corresponding to a 3 to 1 density jump across the shear boundary layer (Keskinen et al., 1988). The example simulation is conducted in the neutral wind frame of reference (required for the initial balanced state Keskinen et al. (1988)) per Eq. (3.27). Fig. 3.15A shows the linear growth rate compared with the nonlinear simulations for the small $\widetilde{\nu}$ limit demonstrating a generally reasonable match particularly during the early stages of the instability. Inherent complexities in seeding the simulations and nonlinear evolution make comparing the linear theory to the simulations challenging and we do not pursue those further.

Fig. 3.15B–E shows snapshots of the nonlinear stage density resulting from primary KHI at various times during our example simulation. Panel (B) shows initial appearance of the characteristic vortices forming near the beginning of the nonlinear stage of evolution—note consistency of the wavelength of these perturbations with the theoretical fastest growth mode (~45 km wavelength). In panel (C) both the effects of the forward and inverse cascade can be seen as what were initially two well-formed vortices have merged into a single large vortex with small-scale structures evident inside. Panels (D)–(E) show late-stage evolution of the instability which is characterized by turbulence

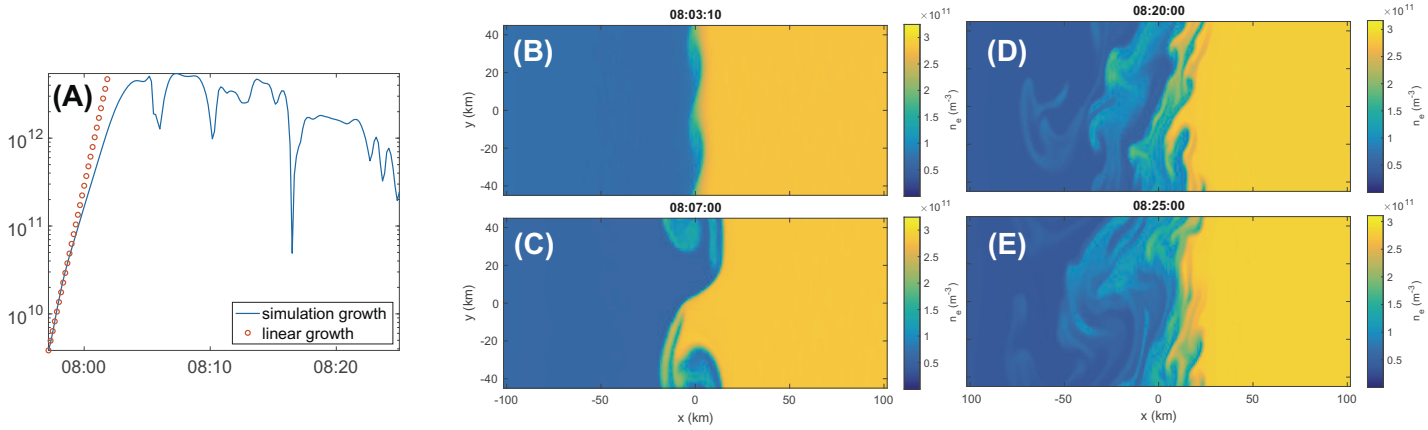

Fig. 3.15 Time-dependent evolution of KHI in our example simulations.

(wide range of spatial scales apparent) and showing intrusion of density irregularities into regions well outside the initially narrow boundary layer.

3.2.3.4 Secondary instabilities, time-dependent cascade

Anecdotal evidence of secondary instability exists in prior simulation studies that have simulated GDI and KHI. Mitchell et al. (1985) and Huba et al. (1988) discussed the effects of capacitance on the nonlinear development of GDI in terms of the effects of the size of the late-stage bubble structures—there is a tendency toward larger structures when polarization currents are included—similar to what we see in the example simulations in Fig. 3.14. Gondarenko and Guzdar (1999) showed that inertial effects also lead to pronounced tilting and further structuring of the elongated "fingers" that develop due to primary GDI. These studies have generally made it clear that the presence of electrodynamic effects (encapsulated in polarization currents) impacts the spectrum of irregularities present, particularly during the late-stage evolution of the instabilities. KHI modeling by Keskinen et al. (1988) shows that the cascade of density structures to small scales in the vortexes that form as secondary KHI waves are generated on the edge of the primary waves as they steepen and begin to "break." Since they initialize their simulations with a harmonic mode of the full grid, inverse cascade (i.e., formation of larger vortices) is not present, though it is readily apparent in our examples in Fig. 3.16.

Recent high-resolution modeling studies of GDI in the polar cap and KHI in the cusp show the evidence of secondary instability in the form of highly turbulent density fields suggestive of a combination of gradient and shear-driven effects. Fig. 3.16 (left), following Deshpande and Zettergren (2019), shows a simulation of late-stage GDI in which

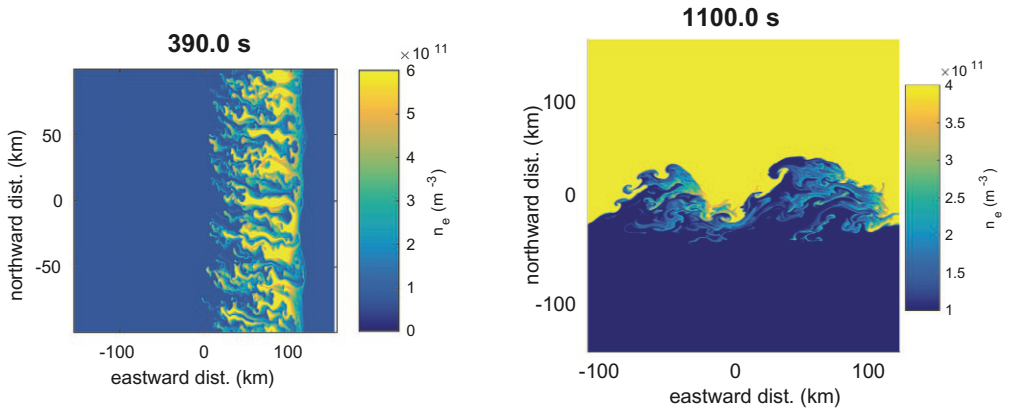

Fig. 3.16 Examples of well-developed secondary instability tending toward turbulence (following Deshpande and Zettergren (2019) and Spicher et al. (2020)). Left: Density structures at 300 km altitude during the nonlinear stage of GDI. Right: Density structures at 300 km altitude during the nonlinear stage of KHI.

wave-like structures can be seen to have a grown on the edges of the density "fingers." Similarly, Fig. 3.16 (right) shows KHI modeling from Spicher et al. (2020) shows both the formation of vortexes-within-vortexes and regions of bubble-like structures reminiscent of secondary GDI.

It can be seen from the simple example simulations in Figs. 3.14 and 3.15 that the primary GDI naturally results in situations favorable for secondary KHI (and vice versa). Fig. 3.17 shows both density and flow structures during the nonlinear stage of each of these instabilities. Fig. 3.17A and B shows density and x-component of plasma drift for the GDI simulation with ionospheric inertia. Fig. 3.17C and D shows density and y-component of drift for the example KHI simulation. Comparison of Fig. 3.17A and B shows clearly that sheared flows develop in the GDI "fingers," with slower flows in the high-density regions and faster flows where density is lower. Fig. 3.17C and D shows collocated drifts along density gradients formed from primary KHI.

Further complications involving excitation of secondary instabilities prevent a simple and fully accurate description of such dynamics. M-I coupling, encapsulated by the inertial capacitance parameters in our analysis, plays the dual role of destabilizing KHI while stabilizing GDI. As such secondary instabilities (KHI leading into GDI and vice versa) will be very sensitive to the ratio of conductance to capacitance $\widetilde{\nu}$. The particular, quantitative effects of this parameter on secondary instabilities have not been studied carefully as far as we know. The presence of plasma drifts at an angle other than normal or tangent to background density gradients has the potential to create a wider range of density irregularities since both primary GDI and KHI (if shears are also present) may be excited in a way that interacts strongly, e.g., with each instability providing robust seed structures for the other. Such "mechanics" have been suggested in prior studies as possibly contributing to fast structuring of polar cap patches leaving the cusp region (Carlson et al., 2007), but to our knowledge have not been fully studied with a robust modeling approach and an eye toward self-consistent comparisons with available data.

3.2.3.5 Mapping of electric fields: E-region shorting

Instabilities discussed herein are quasi-static in nature (viz involving charge accumulation) and are affected by the presence of any type of conducting pathway that allows neutralization of this charge. The E region can be strongly conducting by comparison to the F region where these instabilities initiate, even for a relatively modest plasma density and may be understood to generally suppress irregularity growth. A complicating factor to this is that for small-scale sizes perpendicular to the geomagnetic field the electric fields will no longer map large distances (Farley, 1959; Kintner and Seyler, 1985) and the unstable modes will tend to localize along the field line, to a degree. There are several different limiting descriptions, then, of the behavior of the instabilities (a) purely local—wherein only the F region is considered, (b) perfect mapping of fields between the F and E region, which can describe the suppression of instabilities, and (c) full 3D treatments, which will

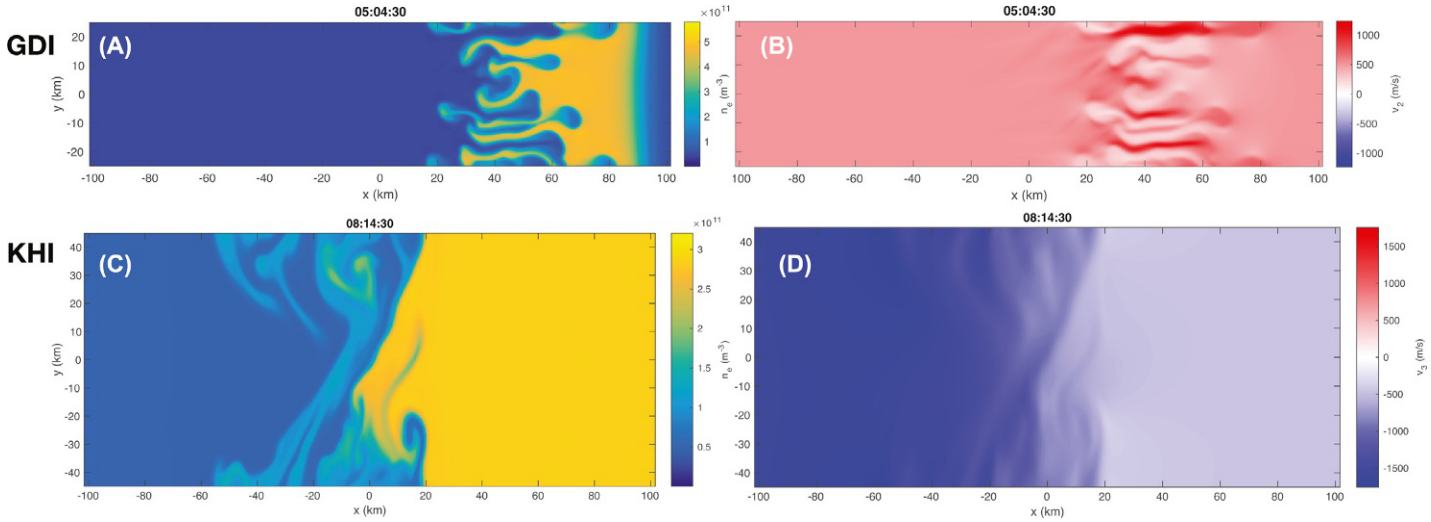

Fig. 3.17 Density and drift for the GDI and KHI simulations showing a tendency for excitation of complementary instabilities. Panel (A) Density at 300 km altitude from the GDI simulation with ionospheric inertia. Panel (B) *x*-component of the plasma drift velocity exhibiting small-scale shearing at the interface of the density "fingers." Panel (C) density structuring during the nonlinear stage of the KHI simulation. Panel (D) *y*-component of the plasma drift illustrating a substantial component along the density gradient in some locations.

describe both the shorting process and the localization of modes as they cascade to the smallest scales. We consider, in simulations presented in this work, scenario (b) which is valid in the limit of perfect mapping of the fields.

Following Farley (1959), Kintner and Seyler (1985), and Huba et al. (1988), we may roughly estimate the field line mapping distance of potential for a structure by considering the electrostatic form of the current continuity equation under assumptions of constant conductivity (for simplicity and sake of illustration).

$$\sigma_{\parallel}\frac{\partial^2\Phi}{\partial z^2}+\sigma_P\frac{\partial^2\Phi}{\partial x^2}=0 \tag{3.37}$$

Applying a trial solution of $\Phi(x,z)=\Re\{\widetilde{\Phi}\,e^{ik_{\parallel}z+ik_{\perp}x}\}$ to this equation yields:

$$k_{\parallel}^2\sigma_{\parallel}\,\widetilde{\Phi}+k_{\perp}^2\sigma_P\,\widetilde{\Phi}=0;\quad k_{\parallel}=ik_{\perp}\sqrt{\frac{\sigma_P}{\sigma_{\parallel}}} \tag{3.38}$$

Thus, for a perpendicular oscillation having real wavenumber $k_{\perp}$ the parallel variation of potential is imaginary and positive such that it *decays exponentially* along the geomagnetic field line with a characteristic length scale of

$$\lambda_{\parallel}=\lambda_{\perp}\sqrt{\frac{\sigma_{\parallel}}{\sigma_P}} \tag{3.39}$$

In the F region, the conductance ratio is quite large, indicating that electric fields generated here due to charge accumulation (i.e., fields from charge accumulation) will map fairly effectively until the scales become quite small. For an F-region Pedersen conductivity of 5×10^{-6} S/m and a parallel conductivity of 25 S/m (conditions somewhat similar to many of our simulations), a $\lambda_{\perp}=1$ km structure will map about 2200-km along the field line (i.e., well into the magnetosphere).

Simple simulations presented in Fig. 3.14 have suggested, as discussed, that the presence of any type of E-region, however, modest, slows the growth. This particular example shows that even 0.05 mW/m^2 of precipitation particles will damp growth of GDI quite substantially such that it appears to grow much slower than the linear and local analysis suggests and could potentially play a role in stabilizing drifting patches.

While finite parallel conductivity will tend to suppress mapping of fields between the E and F regions, the coupling with the magnetosphere is largely dictated by ion inertial effects. The inclusion of these effects through a simplification of the generalized Ohm's law (e.g., Kintner and Seyler, 1985) removes the fundamental physics of wave propagation (Alfvén waves) from the system. Such assumptions effectively model the ionosphere as a distributed capacitance rather than a system that exchanges information with the magnetosphere via transmission and reflection of waves. For waves with a sufficiently long wavelength (low frequency), the adopted model is probably reasonable, but it is clear that applicability will not extend to higher frequency waves. The typical Alfvén

speed in the topside ionosphere is in the ballpark of ~100 km/s (obviously this will be sensitive to geomagnetic conditions). For a distance of 1000 km, this corresponds to a 10 s time scale; in some cases, this may be comparable to linear growth rates estimated above. Thus, our "local" (viz nonwavelike) model of ion inertia can only be considered an approximation and there are additional dynamics concerning Alfvén waves that may, in principle, need to be resolved in future modeling efforts.

3.2.3.6 Nonlinear steepening

The nonlinear character of GDI naturally results in steepening of initial density irregularities as the instability proceeds. This can be understood as a consequence of the finite geometry (y-direction) of the irregular "finger-like" density structures as they form. The accumulation of charge on the lateral edges (y extents) of these structures results in an electrostatic field and response $\mathbf{E} \times \mathbf{B}$ drift that slows the high-density region such that it moves more slowly that the surrounding region. At the same time, the velocity field tends to be convergent on the trailing edge of the structure so that the density gradient steepens. This steepening dynamic has been discussed in the context of finite plasma clouds in studies by Perkins et al. (1973) and Zabusky et al. (1973). Similarly the divergent nature of the flows on the leading edge of a finite high-density structure lends a more diffuse character to its evolution (this can be seen in simulations where the bubbles "break through" the front edge of the patch).

Steepening and cascade to small scales have important consequences for how the instability can be described during its various phases. During the initial stages of the instability, when the irregularities have not yet steepened fully, the perturbation potential structures can be expected to map efficiently along geomagnetic field lines. As steepening and cascade occurs, smaller structures naturally develop such that at some point it is likely that the EFL approximation will be violated. Coupled with this, at the smallest scales we consider (10s of meters), cross-field diffusion, and associated charge accumulation will generally act to stabilize the progression of GDI (Kelley, 2009). Consequently, to fully describe evolution at these scales one needs to account for finite perpendicular pressure and fully three-dimensional potential variations; this is extremely challenging from a numerical point of view as it places rather extreme requirements on the number of grid points needed for such simulations. To date models have not been able to resolve these scales and physical processes fully.

3.2.3.7 Stirring of ionospheric plasma via external forcing

Another mechanism that has gained significant attention to explain ionospheric irregularities is referred to as *stirring* (or sometimes "turbulent mixing," though we avoid this term) (Kelley, 2009). The distinction between stirring and the ionospheric instabilities (and resulting turbulence) discussed to this point is that processes labeled as stirring are *externally imposed* on the ionospheric plasma. A spatially inhomogeneous background

electric field, which could be generated by magnetospheric structuring will, e.g., result in the strong growth of GDI in specific directions (e.g., Burston et al., 2016; Kelley, 2009) leading to a potentially complicated, inhomogeneous field of irregularities. Additionally, turbulence in the neutral atmosphere can likewise stir the plasma and create irregularities through ion-neutral collisional momentum transfer (e.g., Kintner and Seyler, 1985). In both of these cases, the irregularities partially result from influences outside the ionospheric plasma rather than purely due to internal plasma dynamics in the ionosphere.

Various studies have considered the impacts of stirring on irregularity generation. For instance, using sounding rocket data, Earle and Kelley (1993) concluded that stirring would be as probable as linear instability theory to explain their observations. Additionally, Kivanc and Heelis (1997) studied the spectral characteristics of density and velocity structures associated with 18 polar cap patches and found the presence of structures on most of the patches identified, regardless of their location. The authors suggested that while the GDI could contribute to the development of the irregularities, their creation could be more easily explained by a stirring mechanism. This was further supported by Kivanç and Heelis (1998) who based on a statistical analysis, suggested that GDI was not the dominant mechanism for creating the density and velocity irregularities observed on scale-size ranging from 30 km to 300 m and that the majority of 1-km scale size density irregularities was due to inhomogeneous velocity structures of magnetospheric origin; these could stir density gradients or initiate KHI (Kivanç and Heelis, 1998). Finally, as already discussed in Section 3.2.2.4, Burston et al. (2016) compared linear growth rates of different mechanisms including GDI, KHI, CCI, and found inertial turbulent mixing to be dominant, followed by inertial GDI.

3.2.4 Simulating observable effects of ionospheric instability: Remote sensing tutorial

Although plasma irregularity cascading and turbulence are known to be important factors in ionospheric physics, the fundamental physics behind these processes is still relatively poorly understood. In situ measurements are expensive and are limited to confined spatial regions along the spacecraft trajectory. Thus, remote sensing of the ionosphere using a veritable "ocean of information" from the navigation and communication satellites presents a unique tool to investigate the ionospheric instabilities and helps us understand their effects. However, scintillation observations alone are insufficient to understand responsible plasma physics. Thus, in order to solve this problem, we need other supplementary approaches such as modeling, including full physics-based simulation tool that can capture the observable effects of ionospheric instabilities and can assist in scintillation prediction. In this section, we will review the theory of propagation of signals in random (viz turbulent) media followed by a discussion about the current propagation modeling efforts.

Basu et al. (1981, 1988) used in situ satellite data from Atmospheric Explorer D (AE-D) to model scintillations at high latitudes; note, however, that these measurements are not sufficient to represent geomagnetic and altitudinal variations of density fluctuations. Fremouw and Rino (1973) presented the first empirical model that could estimate the S4 scintillation index (normalized standard deviation of amplitude fluctuations) for VHF/UHF under weak scattering conditions, which often underestimate scintillations at auroral latitudes. Two climatological models, Global Ionospheric Scintillation Model (GISM) and WBMOD (for WideBand MODel) ionospheric scintillation model have had success in predicting the overall trend of scintillations. However, they lack the capability of resolving the scintillation effects of irregularities in localized regions. WBMOD also fails to predict the day-to-day and short-term (during a magnetic storm) variability of scintillations (Wernik et al., 2003) (see also Priyadarshi (2015) for a review of these scintillation models). A more recently developed global full 3D forward propagation model Satellite-beacon Ionospheric-scintillation Global Model of the upper Atmosphere (SIGMA) attempts to address many of these issues (Chartier et al., 2016; Deshpande and Zettergren, 2019; Deshpande et al., 2014; Deshpande et al., 2016). SIGMA takes electron density distributions from an empirical, spectral, or physics-based plasma model. SIGMA is based on multiple-phase screen (MPS) method and that solves forward propagation equation according to the theoretical presentation by Rino (2010). The use of this model is discussed further in detail in Sections 3.2.4.2 and 3.2.4.4. In this section, we will review the theory of propagation through a turbulent ionosphere in Section 3.2.4.1, followed by a discussion of some of the state-of-the-art propagation models in Section 3.2.4.2. We will then compare the spectral and physics-based models of ionospheric irregularities in Section 3.2.4.3. Some specific signatures of scintillations observed on the ground when the signal passes through GDI or KHI are discussed in Section 3.2.4.4. Signal received on the ground can be used to derive physical properties of the ionospheric irregularities the signal passes on its way using an inverse method. This is discussed in Section 3.2.4.5. Different radio frequencies are sensitive to different scales of ionospheric structures as they propagate through those as discussed in Section 3.2.4.6. Finally, to complete the discussion of effect of the irregularities on radio waves, we briefly touch the topic of high-frequency (HF) reflections in Section 3.2.4.7 as a means to probe some of the ionospheric irregularities.

3.2.4.1 Theory of propagation through a turbulent ionosphere

Radio signals propagating through the turbulent ionosphere is a problem of propagation of electromagnetic waves through *random media*; the signal undergoes reflection, refraction, diffraction, and interference. Standard scintillation theory simplifies this complicated problem by assuming that there is no backscatter (only forward scatter) and it is mainly weak scattering (Rino, 2010) which mostly holds except for some strong auroral scintillation instances. In this section, we present a brief summary of the theory of propagation of transionospheric signals. The reader is referred to the classic reviews by Yeh

and Liu (1982) and Bhattacharyya et al. (1992) for more detailed descriptions of many scintillation-related concepts and propagation of transionospheric signals.

Propagation of radio waves through the constantly changing ionosphere can be solved by using a multiple phase screen approach. Simply speaking, a wavefront from radio source (satellite or any beacon) gets distorted while passing through the ionosphere and emerges having a random phase change, because of the turbulent variations of the refractive index of the media (Briggs, 1975). There are a few basic assumptions that need to be stated before describing the solution to the propagation problem. Scintillations observed by a receiver are assumed to be related to ionospheric irregularities that are "frozen-in" with respect to the magnetic field, which is due to electron density structures that are convecting at a uniform velocity along the field lines. Thus, the receiver would record the motion of the diffraction pattern on the ground due to either the motion of the irregularities or the satellite motion or a combination of both. The "non-frozen-in" effects comprise of random flow velocities, however, they are believed to make up only a small contribution toward the high-frequency part of the scintillation spectrum. It should be noted here that a full physics-based plasma model can simulate these effects well. Another assumption is that the scale size of the irregularities that cause scintillations (Fresnel scale and above) is much greater than the wavelength of the radio signal and is smaller than the distance traveled by the signal from the irregularity to the ground. Thus, the radio wave gets scattered only in the forward direction. Furthermore, the last assumption for weak scattering is that the diffraction effects by Fresnel scale-size structures are dominant. This allows us to solve the propagation problem by multiple phase screen approach or Rytov approximation.

The electron density in an ionosphere fluctuates causing the refractive index to fluctuate as well. The deviation of density from its background value ΔN_e is a function of space (x, y, z) and time. The variations Δn_i in the refractive index are approximately linearly proportional to ΔN_e at VHF/UHF under the high-frequency or short wavelength assumption. As a radio wave propagates through the density fluctuations, only the phase is affected by the random fluctuations in the refractive index (to the first order). Fluctuations in optical path are obtained by integrating Δn_i along the vertical direction and are related to the phase deviation by the free-space wavenumber k.

It must be noted that this section uses engineering notation ($j \equiv \sqrt{-1}$ and an $e^{j\omega t}$ time-harmonic convention), in contrast to Section 3.2.2 which uses ($i \equiv \sqrt{-1}$ and an $e^{-i\omega t}$ time-harmonic convention).

The phase fluctuations on a radio signal of wavelength λ as it passes through the irregularity are given by

$$\varphi(\vec{\rho}\,, t) = \frac{2\pi}{\lambda} \int \Delta n_i(\vec{\rho}\,, z, t)\, dz, \tag{3.40}$$

where $\vec{\rho} = (x, y)$ is the transverse coordinate and z is the vertical distance. The phase deviation can be written in terms of the TEC ΔN_T along the signal's path as

$$\varphi(\vec{\rho}\,, t) = -\lambda r_e \Delta N_T(\vec{\rho}\,, t), \tag{3.41}$$

where

$$\Delta N_T(\vec{\rho}\,, t) = \int \Delta N_e(\vec{\rho}\,, z, t)\, dz, \tag{3.42}$$

and $r_e (= e^2/4\pi m \epsilon_0 c^2)$ is the classic electron radius. A plane wave coming from a source that is a lot farther from the ionosphere than the receiver on the ground is from the ionosphere, is represented by its electric field with constant amplitude A_0. Upon emerging from the ionosphere, it takes the following form:

$$\vec{u_0}\,(\vec{\rho}\,, t) = A_0 e^{-j\varphi(\vec{\rho}, t)} \tag{3.43}$$

For the phase screen approach where the random media with density fluctuations ΔN_e is represented as an infinitesimally thin screen that imposes only phase variations (from Eq. 3.41) on the incoming wave. The diffraction pattern of the plane wave beyond the phase screen can be obtained using Kirchhoff's diffraction formula, under the forward scattering assumption. This is described in detail by Ratcliffe (1956).

$$\vec{u}\,(\vec{\rho}\,, z, t) = \frac{jkA_0}{2\pi z} \iint e^{-j[\varphi(\vec{\rho'}, t) + (k/2z)|\vec{\rho} - \vec{\rho'}|^2]}\, d^2\rho', \tag{3.44}$$

where $k = 2\pi/\lambda$ is the wavenumber. $\vec{u}\,(\vec{\rho}\,, z, t)$ is the field at a distance z from the screen and is obtained by integrating the wave field $\vec{u}\,(\mathbf{r}, t)$ (where $\vec{r} = (x, y, z)$ is a 3D spatial coordinate) and its spatial derivative with the simplification from the forward scattering assumption (see Ratcliffe (1956) for detailed derivation). This signal is then propagated through the free space between the phase screens and then from the bottom of the phase screen to the ground, where both the phase and amplitude of the signal vary. The MPS technique (Knepp, 1983) is combined with a split-step solution (a method that treats a problem in smaller steps to separate out linear and nonlinear parts in Fourier and spatial domains) to the forward propagation equation (FPE) that represents all the above steps to solve the scintillation problem in the most general way (Rino, 2010). In this method, the signal experiences phase fluctuations as it passes through the phase screens and in between the phase screens and from the bottom of the irregularity to the ground, it experiences free-space propagation. FPE encompasses refraction, diffraction, scattering, and interference effects on the radio wave propagating through the random ionosphere. The detailed mathematics for FPE is beyond the scope of this review. Thus, the reader is referred to the scintillation theory reviews by Yeh and Liu (1982), Bhattacharyya et al. (1992), and Rino (2010). Yeh and Liu (1982) also gives details about another theory for weak scintillations

called Rytov Solution, which considers the effects of scattering on the amplitude of the wave inside the irregularity. This is valid for the case when multiple scattering effects can be neglected and amplitude scintillations are caused by the irregularities with scales size of the order of the first Fresnel zone. The following section presents some of the current propagation modeling approaches.

3.2.4.2 State-of-the-art approaches

Global climatological models such as WBMOD or GISM provide a global distribution of scintillations and allow us to understand the overall behavior of the responsible irregularities. Recent analytical models, such as a three-dimensional model of plasma plumes that are caused by interchange instabilities developed by Retterer (2010), can be used to derive the strength of scintillations in terms of S4. There are very few recent propagation and scintillation models that have been developed in recent years to study irregularities that cause radio scintillations, especially in high-latitude regions. Deshpande et al. (2014) developed a full 3D forward propagation model SIGMA following Rino (2010) and Rino and Carrano (2011). The model SIGMA solves the FPE to encapsulate the scattering, interference, refraction, and diffraction effects on a radio signal caused by ionospheric irregularities. It can work anywhere on the globe and can accept the electron densities from any form of irregularity model, such as a spectral model (Chartier et al., 2016; Deshpande et al., 2016), an empirical model or a physics-based plasma model, e.g., GEMINI (Deshpande and Zettergren, 2019). Other models based on phase screen theory include a model by Rino et al. (2018a) where a compact parameter set was utilized to simplify the model at equatorial regions and was used for GPS performance analysis at three different frequencies (L1, L2, and L5). A new stochastic structure model called configuration space model was developed to generate realizations of number density that simulates extended highly anisotropic media (Rino et al., 2018b, 2019). This model can be used in propagation simulations applicable at equatorial as well as high latitudes.

3.2.4.3 Physics-based vs spectral approaches to irregularities

Ionospheric irregularities can be modeled using a physics-based model or realization of spatial electron density distributions derived from an irregularity spectrum. The latter is based on an assumption that irregularities are random media with certain statistical properties, e.g., turbulence typically follows a power law spectrum. The irregularity spectrum can then be presented in terms of a single-slope or double-slope power law spectrum. Some of the notable spectral models of irregularities encompassing the constraints on the ionosphere, such as high latitude, weak scattering etc., are those presented by Shkarofsky (1968), Costa and Kelley (1977), Rino (1979a, b), and Wernik et al. (1990). Analytical models by Fremouw and Rino (1973) can estimate the root-mean-square fluctuations in the scintillation index of the received radio signal under averaged scintillation activity. There are other spectral models that have been derived from satellite

data (Basu et al., 1988). Some of the early in situ satellite measurements have pointed to a one-dimensional spectrum following a power law. The 3D spectra of electron density of ionospheric irregularities can be derived easily from the 1D spectra if the irregularities are assumed to be isotropic. The spectra can then be used to obtain a realization of electron number density distribution in the irregularities. However, the spectral models do not encompass the different stages of instability development. Thus, spectral models are only valid for fully developed turbulence which is the reason why we need to consider physics-based models to represent the *evolution* of ionospheric irregularities.

There are very few full physics-based 3D models that can generate plasma structures locally. For example, SAMI3 (Huba et al., 2000, 2008) works at low-to-midlatitudes, calculates the plasma and chemical evolution, and drifts of several ion species given neutral composition, wind, and temperature as input. However, SAMI3 has limited spatial resolution which to date has not been used to resolve scintillation scales. Another similar, high-resolution model for low-latitude phenomena like equatorial plasma bubbles has been presented by Yokoyama (2017).

The ionospheric model GEMINI (Zettergren et al., 2015) includes both aeronomical and electrodynamic processes relevant to the formation of ionospheric fluid instabilities (viz. GDI and KHI) at high latitudes (Zettergren et al., 2015). It has been recently interfaced with the propagation model SIGMA and used with resolutions high enough to resolve structures close to Fresnel scale size (Deshpande and Zettergren, 2019). The models together were also used to study how the difference in the development of KHI (e.g., through changing inertial capacitance) can affect the scintillation onset times as well as the strength of GPS scintillations in cusp regions (Spicher et al., 2020).

3.2.4.4 Scintillation signatures of ionospheric instability

Deshpande and Zettergren (2019) demonstrated that a combination of a physics-based plasma model and a propagation model can be used to study radio signal fluctuations on the ground as the signals pass through an instability, such as GDI, and that with reasonable initial conditions, the instability generated from GEMINI can result in GPS signatures on the ground comparable to observations. Fig. 3.18 shows an example of scintillations produced by GDI. Panel A of Fig. 3.18 shows an illustration of SIGMA where a signal from a satellite scatters between the layers (or phase screens) and propagates to the ground experiencing phase and amplitude fluctuations. Fig. 3.18B shows three different snapshots of 2D electron density at the height of maximum F region; Fig. 3.18C shows the snapshots of the corresponding propagated 2D phase on the ground, and Fig. 3.18D shows the phase time series which are basically obtained with the value at receiver shown by the red cross in each snapshot of panel (B). Phase scintillations seem to appear when the signal passes through the trailing edges of GDI or the patch here, especially when the large-scale structures in the GDI break into small-scale structures. During the earlier time of GDI development when the patch is starting

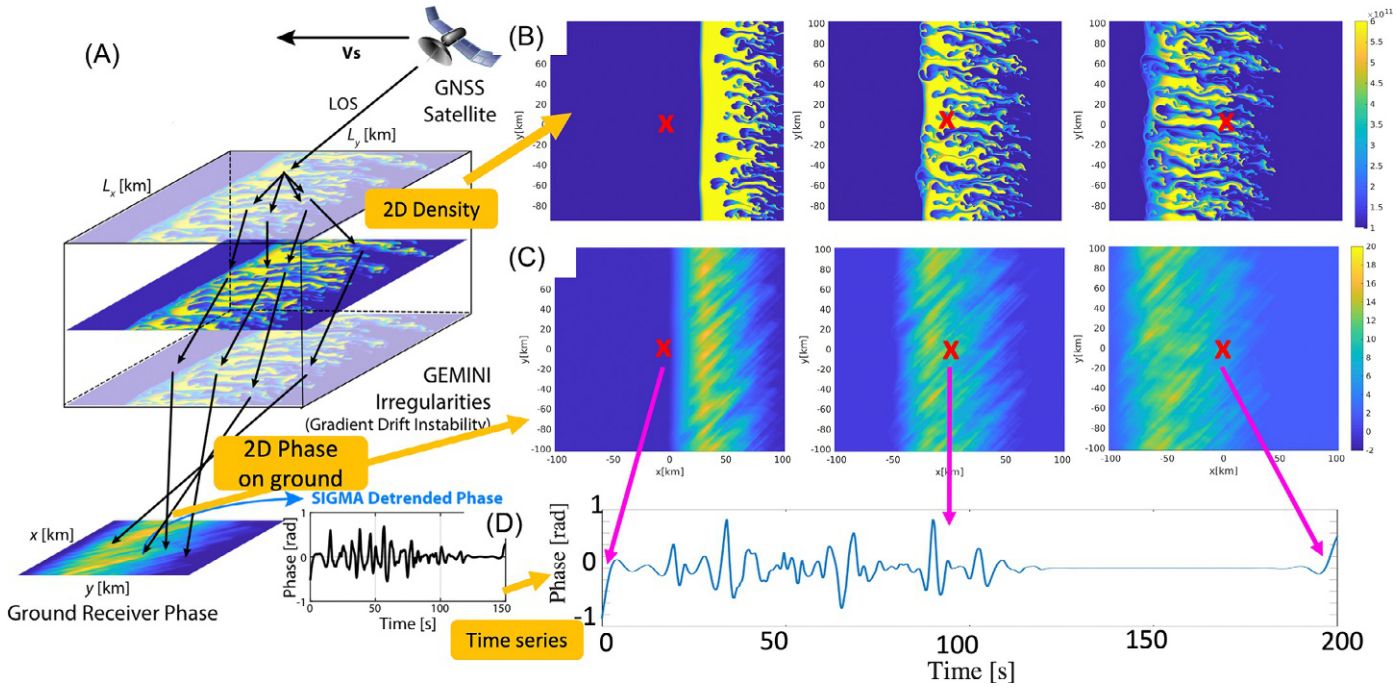

Fig. 3.18 (A) Illustration of SIGMA showing the density cube where scattering of radio signal occurs and the fluctuations are observed on the ground in the form of time series as well as simulated propagated 2D phase pattern on the ground. At different stages of development of the density structures represented in (B) as 2D snapshots of density, (C) the 2D phase pattern on the ground and thus (D) the fluctuations in the time series on the ground, all change.

to break into structures that are still too large compared with scintillation scales, the radio signal passing through those structures does not undergo any scintillation (not shown in this figure). Predominant spectral power appears to be concentrated in the spatial scales of 1–4 km for the case shown in Fig. 3.18.

Very recently, using observations and modeling, Spicher et al. (2020) presented a nonlinear, quantitative analysis of the KHI as the possible source of irregularities causing GPS phase scintillations detected in a cusp flow channel, and how it causes GPS phase variations. Using GEMINI-SIGMA they observed that, compared to GDI, KHI displays a specific pattern in scintillation occurrence, that is, with respect to the density boundaries, vortices, and small-scale structures developing around those vortices. Under reasonable assumptions consistent with observations, their modeling results showed that KHI could be responsible for the creation of density irregularities within minutes, assuming a shear scale length of $\ell \sim 1$ km. They studied how simulated KHI or shear (of varying inertial capacitances of ~10 F and ~30 F and maximum Pederson conductance ~1.2 S) affects scintillations at different stages of KHI development. For the numerical simulations performed, their findings include, for example, with larger capacitance KHI generates vortices and structures of scintillation scale earlier than that with the lower capacitance.

3.2.4.5 Inverse analysis

The technique of data inversion allows one to understand the physics behind remotely sensed observations. For GNSS scintillation data, there have been studies that used an inverse technique to infer ionospheric irregularity parameters such as turbulence strength, the height of irregularity, density in the background, etc. at low and high latitudes (Carrano and Rino, 2019; Carrano et al., 2012; Deshpande et al., 2016; Keskinen, 2006). All of these studies are essentially trying to fit N data points to a scintillation or propagation model that has M adjustable parameters and which predicts a functional relationship between the measured independent and dependent variables. The typically used method for the fitting is the least-squares fit (the maximum likelihood estimator (Press et al., 1992) for assumed Gaussian statistics). An inverse technique, however, calls for running the full propagation models over a multidimensional parametric space, which is possible only if the computation time for each run is not overly burdensome. Having said that, coupled models such as GEMINI-SIGMA may take a few days for a single run, preventing their use for an inverse analysis. For scintillation models with more than half-a-dozen parameters to fit, it is prudent to use data from other instruments such as radars, satellite data, ASI, etc. to provide a priori specification of some parameters. Another tool that can be extremely useful for inverse analysis for radio scintillations are groups of radio receivers which permit using a spaced-receiver analysis technique to estimate ionospheric drifts for irregularities "frozen-in" the magnetic field lines (Costa et al., 1988; Datta-Barua et al., 2015; Rino and Livingston, 1982). Furthermore, if signal fluctuations can

be fit using a Rytov spectrum, i.e., assuming that weak scattering is occurring, it is possible to use an inverse analysis to estimate the height of the scattering layer, and its thickness (Yeh and Liu, 1982).

3.2.4.6 Scale-dependent scintillation

The majority of observational techniques presently used can either achieve good coverage across large areas of space and time (i.e., ground-based radars and imagers) or high resolution (i.e., instruments on satellites and sounding rockets), but generally not both. This makes it challenging to investigate the full range of dynamics and coupling at all scales using observations alone, but they can play an important role in constraining model parameters. Using ISRs, the approximate size, shape, and basic characteristics of patches can be determined and used to initialize realistic model runs. Furthermore, the output of scintillation models can be compared with real scintillation measurements to determine how closely the models captured the physical processes that occurred in the ionosphere. This is particularly important for tuning model input that cannot be measured directly.

Radio waves are most sensitive to scintillation by ionospheric structures at the Fresnel scale (Yeh and Liu, 1982). The Fresnel scale depends on both the distance between the irregularity layer and the observing receiver and the frequency of the incident radio wave. This means that radio waves of different frequencies will be sensitive to structuring at different scales. GPS and GNSS satellites often transmit multiple frequencies, but they are usually all fairly close together in the L-band (1–2 GHz). To probe different scales in the ionosphere, it is useful to also consider the scintillation of ultra high-frequency (UHF) and very high-frequency (VHF) signals, where available. Some low Earth orbit satellites carry Coherent Electromagnetic Radio Tomography (CERTO) beacon transmitters, which continuously transmit VHF (150.012 MHz), UHF (400.032 MHz), and L-band (1066.752 MHz) radio waves (Bernhardt and Siefring, 2006). These signals can be detected by ground receivers and analyzed for scintillation similar to those observed on the GPS signals. Scintillation observations at multiple frequencies allow one to consider if ionospheric irregularities are uniformly distributed over a range of spatial scales or if a particular size is favored under some conditions.

3.2.4.7 HF effects

Propagation of high-frequency (HF) signals, generally identified as 3–30 MHz, can also be influenced by plasma irregularities. HF signals experience significantly more refraction and diffraction in dense ionospheric plasma than the higher frequency signals discussed previously in this chapter. This extreme refraction allows oblique HF radio signals to be "reflected" off the bottom side of the ionosphere and permits over-the-horizon communication. A substantial amount of work has been done to create raytracing algorithms that determine the propagation path of a HF signal through an inhomogeneous ionosphere

(Frissell et al., 2018; Michael et al., 2020; Ravindran Varrier, 2010; Theurer, 2012). Additionally, Smith et al. (2020) applied the finite-difference time-domain method to solve for electromagnetic wave interactions with subkilometer scale plasma irregularities and determine the transmission through a perturbed ionosphere.

3.2.5 Synthesis, outstanding issues and future needs

Evaluating contributions of precipitation to scintillation Particle precipitation is believed to contribute to plasma structuring in the cusp region at F-region altitudes, where low-energy ($\leq$1000 eV) electrons deposit most of their energy (e.g., Dyson et al., 1974; Kelley et al., 1982; Millward et al., 1999). While Moen et al. (2002) hypothesized that the source of the decameter-scale irregularities associated with HF backscatter in the cusp might be due to the structures within particle precipitation, evidence suggests that precipitation acts as a direct source of density fluctuations with scale sizes about $\lambda \geq$ 7 km (Dyson et al., 1974; Kelley et al., 1982; Labelle et al., 1989), or as seed irregularities on which the GDI could operate causing small-scale irregularities (Moen et al., 2012; Oksavik et al., 2012).

Recent observations also support the view that structured precipitation and associated FACs are an essential component for the creation of severe scintillations around the dayside auroral region (Fæhn Follestad et al., 2020). Furthermore, on the nightside, Jin et al. (2014, 2016) and Clausen et al. (2016) showed that the strongest phase scintillations occur when polar cap patches have entered the nightside auroral oval, implying that auroral dynamics including precipitation and/or field-aligned currents and flow shears play important roles in enhancing plasma structuring at phase scintillation scales. Additionally, Kinrade et al. (2013) presented statistical evidence of a correlation between enhanced σ_φ (standard deviation of phase fluctuations) and auroral intensity, and Semeter et al. (2017) and Mrak et al. (2018), using precise multiinstrument observations, showed that strong phase fluctuations and signal loss of locks were collocated with trailing edges of nightside auroral arcs in the E region. Chartier et al. (2016) presented observations of an auroral E-region ionization enhancement occurred with associated phase scintillations, modeling of which showed that an enhanced E-region density on top of the mean EISCAT density was needed to explain the observed phase scintillations.

Evaluating the effects of auroral precipitation and/or FACs on irregularity creation at different altitudes, and comparing it with respect to instabilities such as KHI or GDI is thus essential to advance our understanding and for differentiating the importance and contributions from these different sources of density irregularities. There are currently no detailed modeling studies that have evaluated how precipitation may directly induce irregularities or serve to generate seed structures; however, contemporary instability models now contain physics-based descriptions of energetic electron transport (e.g.,

Deshpande and Zettergren, 2019; Spicher et al., 2020) so these studies appear to now be feasible.

Small-scale density irregularity evolution Despite the importance of density irregularities, a complete physical description of how structures cascade from ~10–100 s of km scales to scintillation-producing scales (~100 s of m) is still lacking. Effects of secondary physical processes and instabilities (which will affect the smallest scales), along with diffusive stabilization, E-region, and polarization shorting are poorly constrained. Furthermore, evaluation of instability behavior in realistic situations (nontrivial initial and boundary conditions) has not been conducted. Of particular importance to resolve, is the affect of diffusive processes perpendicular to the geomagnetic fields and the behavior of the ionospheric potential in three dimensions at high resolution (i.e., there is a need to remove the EFL assumption discussed herein).

Encapsulating magnetospheric coupling Simulation examples presented and referenced herein demonstrate a strong influence of MI coupling, encapsulated in the magnetospheric capacitance parameter in our models, on the development and details of irregularities during the linear and nonlinear stages of development. Nevertheless, these rely on assumptions about how the currents close either in or outside the model (e.g., via conductance or polarization currents in the ionosphere or through magnetospheric polarization currents, which are assumed to exist but not self-consistently modeled). It is important to note that the models discussed in this review are not proper magnetospheric models in the sense that they do not resolve the propagation of Alfvén waves. The characterization of the magnetosphere in these models is therefore overly simple and furthermore relies on ad hoc assumptions about conditions in the overlying magnetosphere, encoded in the model capacitance parameter C_m.

To our knowledge, there have not been concerted modeling efforts aimed at developing a quantitative description of the ionospheric stirring process (e.g., forcing via space and time-dependent magnetospheric activity), although some studies have examined basic effects on convection reversals (global scale) on the evolution of GDI (Gondarenko and Guzdar, 2004b). To properly account for stirring will require a good observational characterization of the spectrum of the electric field fluctuations in the ionosphere (both in wavenumber and time) to serve as constraints for event-based studies, which would seem like a very promising future avenue for future modeling/theoretical work. In a similar vein, we are unaware of any study that has definitively evaluated the effects of neutral atmospheric turbulence or structured winds on ionospheric irregularities (we also consider this to be a stirring process).

On amplitude scintillation and diffractive effects As mentioned in Section 3.2.1.2, amplitude scintillations are attributed to diffraction due to Fresnel scale or smaller ionospheric structures, while phase fluctuations are due to structures larger than Fresnel scale size. The Fresnel scale depends on the wavelength of radio signals and the height of the structures in the ionosphere, resulting in small-scale sizes for higher frequency. The current state-of-the-art models for simulating the plasma instabilities or the ionospheric structures in the irregularities are limited in resolution. For example, the plasma physics model GEMINI can model the structures in a 3D space of few hundreds of kilometers in each direction with the highest resolution of ~200 m. This could still limit resolving sub-Fresnel scale structures responsible for some of the diffractive scintillations associated with amplitude scintillations at GPS frequencies but it could be sufficient to model amplitude scintillations at lower UHF (400 MHz) and VHF (150 MHz) frequencies. It is computationally expensive to increase the resolution of the modeled plasma structures for both plasma modeling as well as propagation modeling. However, in order to study amplitude scintillations in detail, both low-frequency observations and improvement the spatial resolutions in these physics-based models are necessary.

Toward a more quantitative approach to interpreting scintillation data Future studies of ionospheric instabilities and scintillation would benefit greatly from more quantitative methods for analyzing scintillation data. Recently developed physics-based simulations and data processing tools would seem to be a promising avenue for predicting scintillation time series resulting from different types of instabilities as a function of progression through the linear and nonlinear stages and into turbulence. This opens up the possibility of being able to identify unique observational signatures of different instabilities as a function of stage of progress, angle of observation, background conditions, etc. Such a possibility represents a potentially powerful, untapped tool for studying instabilities in different geophysical situations, especially since scintillation observations are numerous and can leverage existing, dense GPS receiver networks.

3.2.5.1 Future needs

Observations and analysis needed to advance the field Many of the current uncertainties in how to correctly initialize and drive plasma irregularity and scintillation models will have to be resolved with improved observations of the ionospheric state. Currently, 3D mappings of the initial state are only achievable with incoherent scatter radars, which tend to have a minimum resolution in the F region on the order of 10s of kilometers. This is comparable to high-resolution global models (25–200 km), but inadequate for local models that can resolve features down to 200 m. There are other observational techniques capable of much higher spatial and temporal resolutions (e.g., in situ rocket and satellite measurements), but these tend to sample an extremely small area in the

ionosphere. Single spacecraft observations of plasma turbulence/irregularities are also generally subject to space-time ambiguities, and require assumptions for analysis (e.g., Taylor's "frozen in" hypothesis) (Narita, 2012; Paschmann and Daly, 1998, and references therein). Fundamental properties of fluctuating fields such as relationships between frequency and wave numbers, wave vectors and wave propagation, energy transfer across scales, growth or damping, etc. may be extracted from multipoint measurements (e.g., de Wit et al., 1999; Narita et al., 2010), making (future) ionospheric multispacecraft and multipoint analysis techniques essential to advance our knowledge of plasma structuring in the ionosphere. Future radar experiments such as EISCAT_3D (McCrea et al., 2015) and advancements like interferometry full-profile ISR fitting may allow subbeam and subrange gate resolution and significantly improve the description of the initial state for irregularity models (Holt et al., 1992; Hysell et al., 2008, 2015). In addition, more work needs to be done in developing methods to merge disparate data sets at different scales (such as All-Sky Imager and ISR data with rocket and satellite data) so that information about both large-scale evolution and dynamics and small-scale initial structure can be made available. Scintillation modeling would also be improved with a more thorough parameterization of spectral models under different ionospheric conditions.

Observationally, it is also essential, moving forward, to obtain a better characterization of physical conditions accompanying inhomogeneous plasma flows, and to be able to quantify shear strengths, shear scale lengths, Pedersen conductance to inertial capacitance ratios, effect of the neutrals, etc. These quantities strongly impact simulation results and would help constrain models to better understand the relationship between different instability mechanisms and irregularities causing scintillations (e.g., Spicher et al., 2020).

Modeling While recently developed nonlinear ionospheric model tools have begun to capture some aspects of ionospheric instability at high latitudes, there remains much work that can, in principle, be done with these tools. Very little of the parameter space of these models has been explored in published works (mostly due to the computational cost of running simulations with large numbers of grid points) so we currently have only very rudimentary ideas of how precipitation, background conditions, seeding, and nonideal effects (i.e., those not encapsulated in the standard linear theory) may affect the onset and progression of instability.

Ultimately, a distributed and dynamic model of the magnetosphere-ionosphere system (including finite propagation times) would be desirable, but due to the fast Alfvén speed in the ionosphere, such an approach would come with a rather extreme computational cost. This is further compounded by the computational expense of running the existing simulations, which must include three spatial dimensions and extremely high resolution to capture Fresnel scales for signals of interest. Indeed existing simulations are already CPU bound and it has proven very troublesome to do something even as

conceptually straightforward as relax/replace the EFL assumption with a full 3D potential solution. Thus, it may be quite a while before a full 3D potential solver or a full description of magnetospheric dynamics can be applied to study ionospheric instabilities. Notwithstanding such issues, there are still more incremental improvements that can be made to better understand ionospheric turbulence, e.g., examination of stirring via time-dependent boundary conditions, etc.

Coupling with local MHD codes with plasma models may also be a future pathway to including a more refined description of magnetospheric aspects of coupling. The ionospheric model itself could be represented via a lumped parameter conductance and capacitance, which could then be connected to a fully electromagnetic model of the overlying magnetosphere, and vice versa. In essence the two codes could, in principle, provide improved boundary conditions to each other in a way that should improve characterizations of magnetospheric effects on the development of ionospheric turbulence.

It is important to note that no simulation studies to date have resolved the full spectrum of turbulence that may be expected to result from the nonlinear coupling of GDI and KHI (i.e., these models are not direct numerical simulations, DNSs). Recent works (Deshpande and Zettergren, 2019; Spicher et al., 2020) have resolved 200 m scales in their simulations; yet higher resolution is needed to study the full instability progression. The likely stabilizing processes leading to a saturated state for the instabilities we study are cross-field diffusion which will tend to become significant at roughly decameter scales (Section 3.2.2.5). A full accounting for turbulence and scintillation that it creates will be needed to resolve these scales as these scales will produce diffractive effect contributing greatly to the scintillation. Additionally, these scales are likely too small to apply the EFL assumption so this will also probably need to be relaxed for DNS simulation of ionospheric instabilities.

We strongly emphasize the importance of improved modeling of precipitating electron population, which can affect conductivity, heating, and other aspects of plasma behavior. Presently GEMINI includes many of these processes but they are based on semiempirical methods which should be compared against physics-based approaches and used to examine the myriad ways in which precipitation can contribute to the formation of density irregularities.

Additionally, there is a need to explore how the spectral slopes of ionospheric density structures change for various stages of different instabilities, how they are related to the in situ measurements as discussed in Section 3.2.1.3, and if there is a correlation of these slopes to the slopes in scintillation data on the ground. This investigation can only be done fully using physics-based models instead of spectral models in the ionospheric irregularity study.

Finally, working with coupled models, such as GEMINI-SIGMA at higher resolution is challenging because of computational constraints, such as memory required for density

blocks, time of computation, Fourier analysis on huge matrices, etc. Furthermore, full inverse analysis is impossible for expensive simulations such as those with GEMINI-SIGMA. For future studies, these models need to be updated to work more efficiently with larger matrices so that high-resolution plasma densities can be enabled. Current propagation models also work with just E or F region. There is a need to meticulously include both E- and F-region effects in propagation modeling, for example, by splitting the propagation into two parts of the ionosphere.

3.3 Ionospheric electron density large gradients at midlatitudes

Shun-Rong Zhang and Ercha Aa

MIT Haystack Observatory, Westford, MA, United States

3.3.1 Introduction

Ionospheric plasma is produced primarily by solar photoionization that varies smoothly on either global or regional scales for any temporal scale. At high latitudes, additional ionization is available due to energetic particle precipitation. Once the ionization is created, many physical and chemical processes can either smooth out the plasma spatial variation or build up large-scale structures. During geospace storms or substorms, some of these processes could be intensified and exhibit significant variability in space and time. These structures often exhibit substantial spatial gradients and thus can impose detrimental effects on modern navigation and communication systems, forming potential space weather hazards. Radio scintillation at L-band frequencies induced by significant density gradients, for example, can cause signal phase disruption and lead to telecommunication difficulties and satellite navigation availability reduction.

In this chapter, we will characterize several typical large-scale plasma density gradient structures, including SED, midlatitude ionospheric trough, and polar cap patch and tongue of ionization (TOI). Fig. 3.19 shows some of these simultaneous structures in TEC and their spatial context during an intense geomagnetic storm. We will discuss some of the fundamental physical and chemical processes. It should be noted that our understanding of these processes remains limited and will continue to evolve as observation, modeling, and analysis efforts make new progresses.

3.3.2 Storm-enhanced density

SED, first coined by Foster (1993), is a highly structured ionospheric disturbance that manifests as a large TEC/*Ne* enhancement channel elongated primarily sunward (azimuthally) and sometimes partially poleward in the local afternoon at mid- and subauroral latitudes. This enhancement is coincident spatially and temporally with storm-time ionospheric characteristics historically named as the "dusk effect" (Buonsanto, 1999;

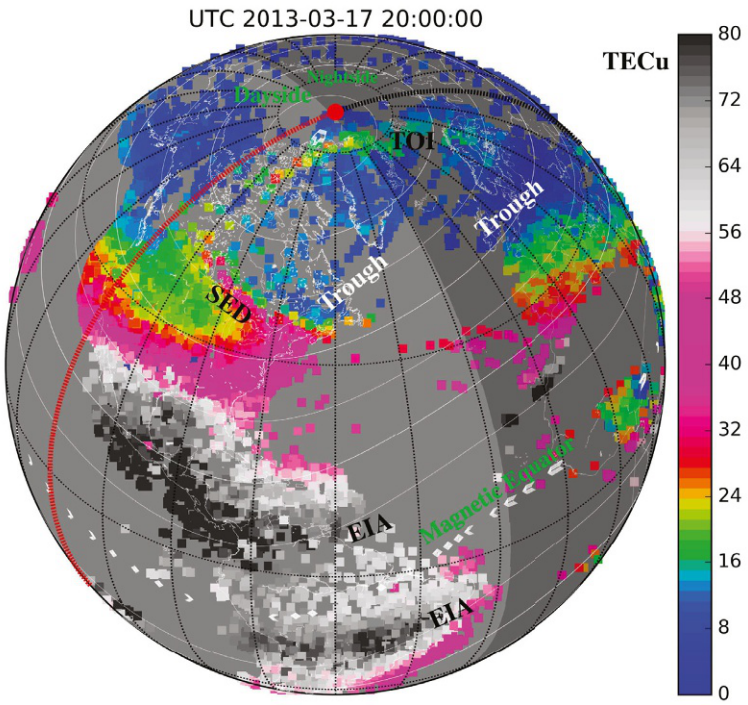

Fig. 3.19 A global view of ground-based GNSS TEC observation during the March 17, 2013 storm. Several plasma density structures are very significant, including storm-enhanced density, the midlatitude ionospheric trough, the polar tongue of ionization, as well as the equatorial ionization anomaly crests.

Mendillo, 2006). This regional ionospheric positive storm phase at dusk was the topic of intense debate in the 1970s (Prölss, 1995). High-latitude convection penetration and disturbance meridional neutral winds were considered as the main processes responsible for the dusk effect.

With the wide availability of GNSS data and coincident satellite in situ measurements in the plasmasphere and magnetosphere, our SED plume understanding evolved to become part of a larger set of geospace storm processes, associated particularly with the erosion of the outer plasmasphere by strong subauroral polarization stream (SAPS) electric fields (Foster and Vo, 2002). SED is associated with the important supply of cold, dense O^+ rich plasma of the ionospheric origin to the inner magnetosphere and eventually to the magnetopause (Walsh et al., 2014). The SED plasma also convects through the cusp into the polar cap, providing significant ion mass flux with high number densities to form the polar Tongue of Ionization (TOI). In general, previous efforts have revealed significant SED longitudinal and UT dependence (Coster et al., 2007; Yizengaw et al., 2006) and magnetic conjugacy (Foster and Rideout, 2007) among other characteristics.

3.3.2.1 Dusk effect

To start with the SED discussion, let us analyze what has been extensively explored under the name of "dusk effect" in the pre-SED era which characterized the SED-type plasma density enhancement as ionospheric positive phase storm. The positive phase ionospheric deviation is typical during the storm's early stage (e.g., the storm main phase). The dusk effect is an electron density enhancement that often occurs at subauroral latitudes, frequently reported in the American sector, in the afternoon-evening sector. The enhancement in both peak density NmF2 and TEC can be substantial, sometimes 50%, lasting for 1–2 h or longer. Fig. 3.20 shows an example of the storm-time F-region electron density observations over Millstone Hill (42.6°N, 288.5°E) and its vicinity. The dusk effect with elevated electron density occurred to the south, east, and west but not quite much to the north of Millstone Hill. To the north is the midlatitude ionospheric trough with low-electron density.

To explain this regional feature of density enhancements, many mechanisms have been suggested including both neutral and electromagnetic effects. Storm-time penetration or expansion of high-latitude convection electric fields with their magnetospheric

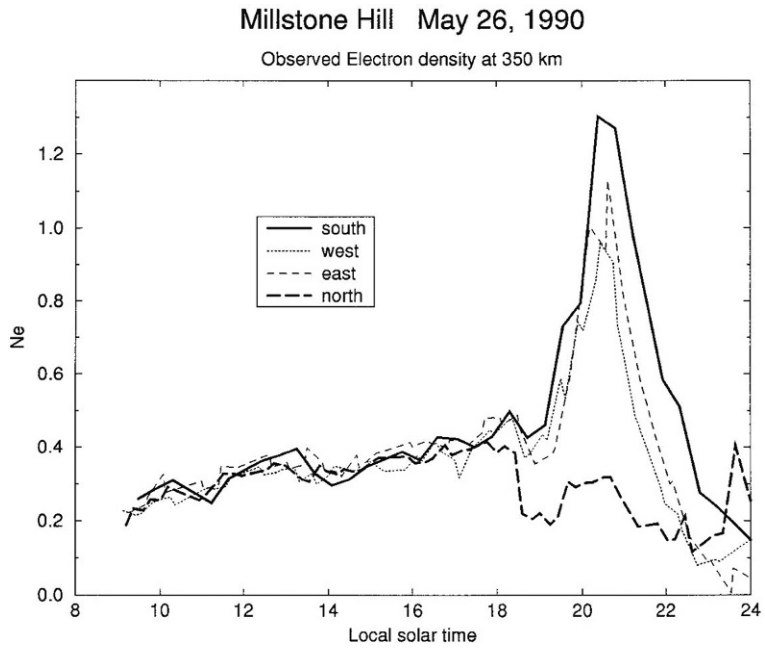

Fig. 3.20 Electron density at 350 km altitude observed by the Millstone Hill incoherent scatter radar steerable antenna pointing at 45 degrees elevation angle to the south, west, east, and north. The dusk effect appears as an exceptionally large north-south density gradient during evening hours. *After Buonsanto, M.J., 1995. A case study of the ionospheric storm dusk effect. J. Geophys. Res. Space Phys. 100 (A12), 23857–23869.*

origin (Kelley et al., 1979) can easily reach Millstone Hill at subauroral latitudes. This dayside electric field has both eastward and polar components, driving poleward and westward plasma drifts, which are perpendicular to the geomagnetic field **B**. The poleward drift perpendicular to **B**, $\mathbf{V}_p^N$, has an upward component which can push ions to high altitudes where they can survive for a longer time due to slower chemical loss rates than they would at low altitudes (Fig. 3.21), thus effectively the upward drift raises the column electron density after a certain time. Also, because of the parabola-type height profile of the F2 region ion density, when the ions are moved upward, the electron density in the topside increases and the bottomside decreases. Indeed, there are both observational and theoretical supports for the penetration or expansion electric field during the period of IMF Bz negative (Fejer et al., 1990; Huang et al., 2006; Jaggi and Wolf, 1973; Nishida, 1968; Spiro et al., 1988). As discussed further in Section 3.3.3.2, a specific pattern of the electric field spatial distribution is needed to account for specific regional patterns of the dusk effects.

An enhanced equatorward neutral wind can induce an ion upward motion along the magnetic field lines to higher altitudes where ions have slower chemical loss rate and longer lifetime, thus enhancing the column electron density. This is very much similar to the effect of the upward component of $\mathbf{V}_p^N$ (Fig. 3.21). Also similarly, enhanced equatorward

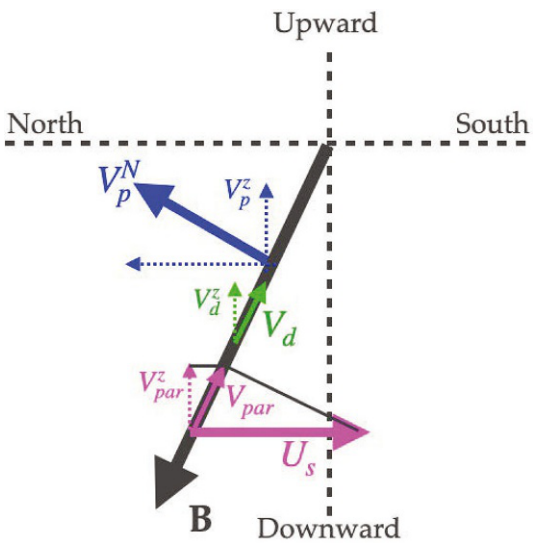

Fig. 3.21 The F region ion motions in the magnetic meridional plane in the northern hemisphere induced by a zonal electric field, a meridional neutral wind, and ambipolar diffusion. $\mathbf{V}_p^N$ is the northward ion drift perpendicular to magnetic field **B**, induced by the eastward electric field **E** through **E** $\times$**B**; $\mathbf{V}_p^N$ has a vertical component $\mathbf{V}_p^z$. $\mathbf{V}_d$ is the ambipolar ion velocity (parallel to **B**) which has a vertical component $\mathbf{V}_d^z$. $\mathbf{V}_{par}$ is the ion velocity induced by the meridional wind $\mathbf{U}_s$; $\mathbf{V}_{par}$ has a vertical component $\mathbf{V}_{par}^z$.

winds can directly enhance the ionospheric density in the topside by the upward transport. The needed equatorward neutral wind enhancement (sometimes a "surge") is a well-established storm-time neutral dynamical phenomenon (Fuller-Rowell et al., 1994; Lu et al., 2020). With the storm onset, Joule and particle precipitation heating within the aurora set up upward and meridional pressure gradients in the upper neutral atmosphere and cause equatorward wind enhancements at midlatitudes. These aurora-driving neutral wind disturbances may be up to a few hundred m/s. They can sometimes reach subauroral latitudes within 1 h, which is faster than the propagation of auroral induced gravity waves (Fuller-Rowell et al., 2002), depending on the exact distance from the auroral zone that is expanding equatorward.

3.3.2.2 SED phenomenology

SED characterization remains an active research frontier involving analysis of available observations primarily from GNSS TEC and incoherent scatter radars at mid- and high latitudes. The essential features can be summarized in the following prospects:

(1) Occurrence. SED is a spatially continuous large-scale feature spanning predominately mid- and subauroral latitudes in the afternoon-evening sectors. It occurs most frequently in the American sector, but evidence in the European sectors and in the Antarctic area exists as well. Fig. 3.22 shows typical SED plumes from TEC observations in North America. The TEC enhancement with a narrow channel appears to have a base in the Northeast US and extend westward in the central US, and northwestward near the northwestern US bordering Canada. It eventually reaches the noon sector near the cusp region, and convects further into the polar cap,

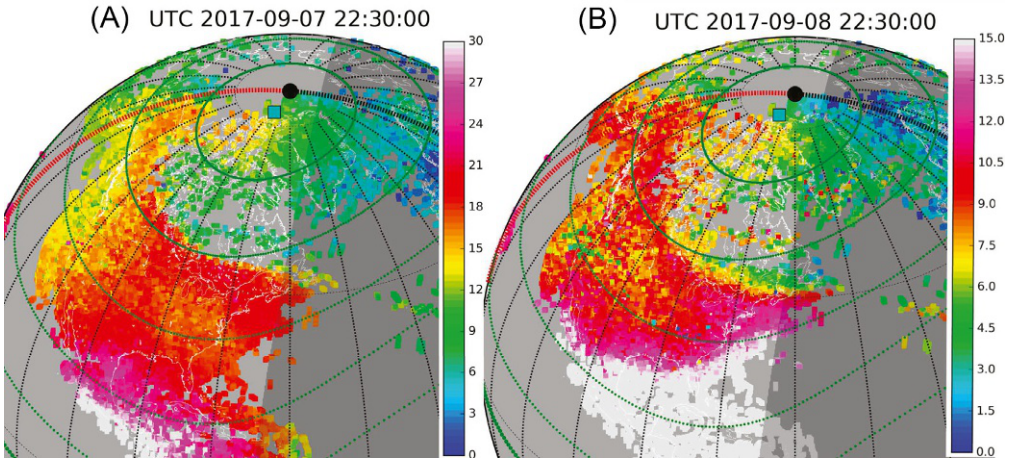

Fig. 3.22 GNSS TEC observations of SED plumes observed at 22:30 UT on September 7, 2017 (A) and on the following day September 8, 2017 (B). Notice the color scale change over the two panels.

contributing to the polar plasma density structures such as Tongue of Ionization (TOI) and patches.

(2) The intensity depends strongly on the level of geomagnetic disturbances. For superstorms (with Dst index less than ~ -250 nT), the SED plume in TEC can elevate above the background by 100 TECu ($1\text{TECu} = 10^{16}$ el/m^2). However, the intensity is also expected to be dependent on background conditions of the ionosphere which provides the source plasma. Fig. 3.22 displays SED plume examples over the same region at the same UT but on two consecutive days (thus influences on season, local time, and UT are minimized). Note that the color scales change by a factor of two. By 22:30 UT on September 2017 when the plume was observed, the IMF Bz drop which had started an hour before reached ~ -10 nT causing ~ -30 nT Dst index. The continuous Bz drop and solar wind speed elevation followed and triggered substantial ionospheric and thermospheric disturbances, including negative phase ionospheric variations with electron density depletion on the following day. 24 h later, the ionosphere was recovering from the impact of another CME causing strong magnetic activities 10 h ago, but Dst remained at ~ -100 nT. The SED plumes appear to be a very repeatable phenomenon, but the second SED was weak with low-electron density elevation when the background electron density in the ionospheric recovery phase was low too, and its northeastern base was more equatorward than it was on the previous day.

3.3.3 Subauroral dynamics and SEDs

Fundamental dynamical processes at subauroral latitudes include intense ionospheric electric fields of various origins and associated plasma drifts, ionosphere-plasmasphere diffusion, and thermospheric neutral wind and composition changes. All these processes result from strong M-I-T coupling.

3.3.3.1 SAPS and ion-neutral coupling

Ionospheric observations at Millstone Hill often indicate a close correlation between the SED occurrence and the fast westward (sunward) convection of ions in the dusk sector. A SED plume is found typically at the equatorward wall of the midlatitude ionospheric trough, whereas the ion fast convection takes place in the SED vicinity but more specifically on the poleward edge of it where the electron density is low. Fig. 3.23 shows this connection using ground-based GNSS TEC and in situ cross-track ion velocity observations from DMSP satellites (Zhang et al., 2017). The ion velocity in this figure is characterized by two sunward enhancements that are located near the trough's equatorward wall and poleward of the wall, respectively, as well as an antisunward enhancement located further poleward. These latter sunward and antisunward ion velocity channels away from the equatorward wall of the main trough are high-latitude convection which

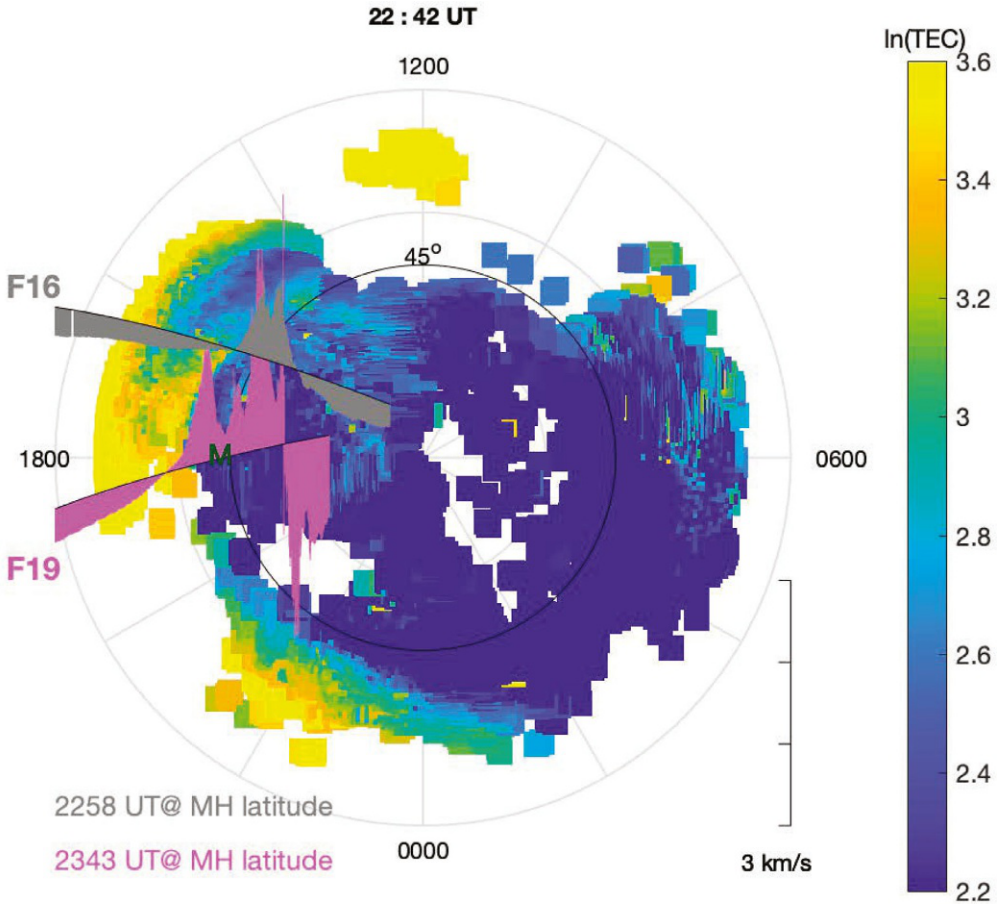

Fig. 3.23 Observations of a SED plume in TEC and SAPS from DMSP F16/F19 cross-track ion drifts. The SAPS channel of sunward ion flow was found near the equatorial wall of midlatitude ionospheric trough region. *After Zhang, S.-R., Erickson, P.J., Zhang, Y., Wang, W., Huang, C., Coster, A.J., Holt, J.M., Foster, J.F., Sulzer, M., Kerr, R., 2017. Observations of ionneutral coupling associated with strong electrodynamic disturbances during the 2015 St. Patrick's Day storm. J. Geophys. Res. Space Phys. 122 (1), 1314–1337. https://doi.org/10.1002/2016JA023307.*

can often expand into subauroral latitudes during storms. The large sunward ion drift near the equatorward wall of the trough is a storm-time feature termed as SAPS.

Storm-time electric fields in the subauroral region, equatorward of auroral electron precipitation, occur frequently and exhibit highly dynamical features as a result of the enhanced coupling of the interplanetary medium to the terrestrial magnetosphere-ionosphere system. SAPS is coined to encompass these subauroral electric fields, including those intense electric field structures in narrow channels shown as polarization jet (PJ)

(Galperin and Zosimova, 1974) and subauroral ion drift (SAID) (Spiro et al., 1979), as well as the broader subauroral regions of enhanced poleward electric fields (Yeh et al., 1991).

SAPS represents a particular signature of magnetosphere-ionosphere coupling of electric fields and currents, in tight feedback loops with the ionosphere in the dusk sector. It overlaps with Region-2 (R2) field-aligned currents (FACs) (Fig. 3.24) which are

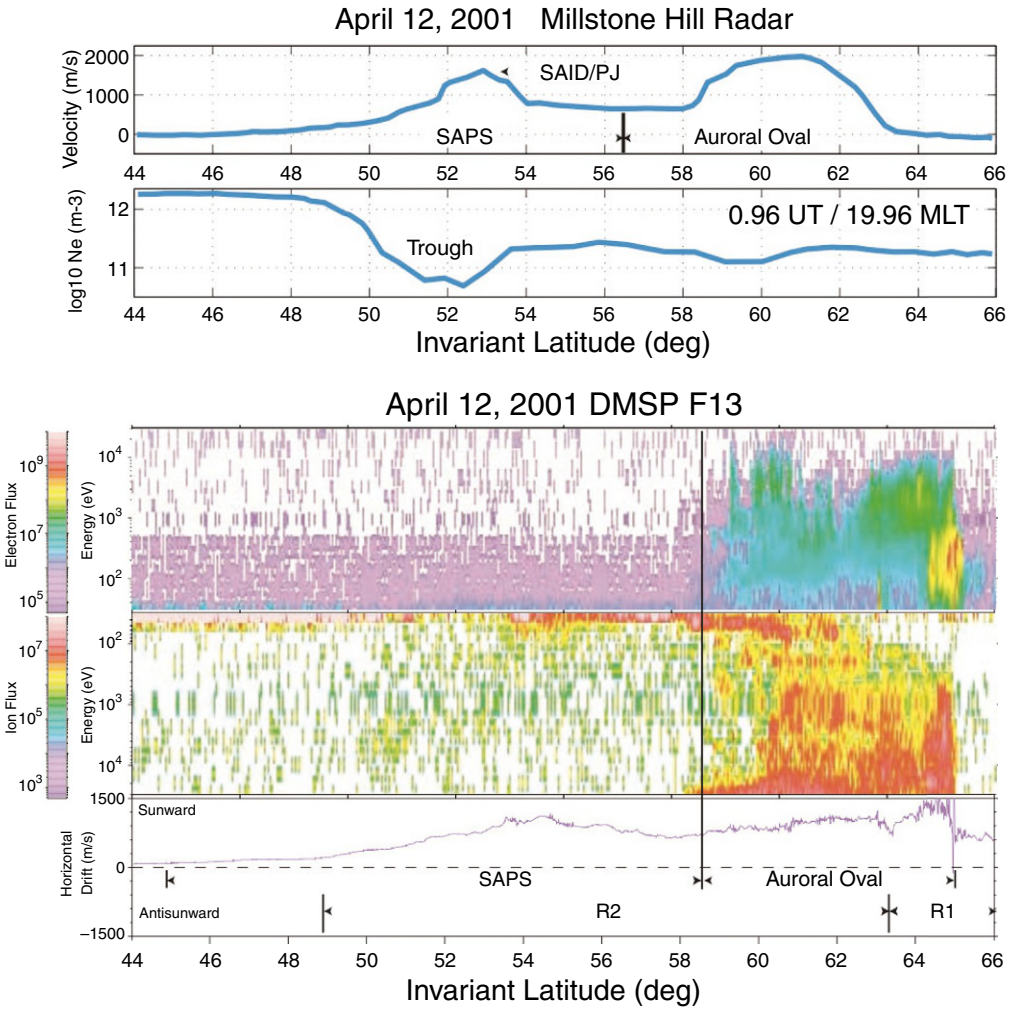

Fig. 3.24 Simultaneous radar and in situ measurements of auroral and SAPS plasma characteristics during a dusk overflight of the Millstone Hill incoherent scatter radar by the DMSP F13 satellite near 01:00 UT (20:00 MLT) on April 12, 2001. The SAPS is seen as a broad region of strong sunward plasma convection centered at 53°N apex latitude, equatorward of the auroral two-cell convection and coincident with a deep ionospheric trough. Region 1 (R1) and region 2 (R2) field-aligned currents have been determined using the DMSP magnetometer data. *After Foster, J.C., Vo, H.B., 2002. Average characteristics and activity dependence of the subauroral polarization stream. J. Geophys. Res. Space Phys. 107 (A12), 1475. https://doi.org/10.1029/2002JA009409.*

believed to be driven by plasma pressure gradients in the inner magnetosphere. A fraction of the ring current and FAC flows into the ionosphere in the main trough region (well equatorward from the electron precipitation auroral region, see Section 3.3.5) of very low conductance. Such a magnetospheric current generator causes a poleward polarization electric field, which is set up to maintain the electric current continuity. An alternative magnetospheric voltage generator, arising from the misalignment of the ion and electron inner boundaries of the plasma sheet, can possibly generate a radially outward polarization electric field in the inner magnetosphere which is poleward when mapping to the ionosphere along the equipotential field lines.

SAPS induced F region ion drifts have been analyzed by using incoherent scatter radars (at Millstone Hill and Poker Flat), SuperDARN systems at midlatitudes, and satellite in situ observations (Erickson et al., 2011; Foster and Vo, 2002; He et al., 2014; Kunduri et al., 2017; Wang et al., 2008). SAPS spans the afternoon through dusk to the early morning sector for all Kp greater than 4, with narrow channels of a few degrees of latitudes. The SAPS ion velocity varies in a large range from a few hundred m/s up to 2 km/s. The magnetic latitude peak location of the SAPS flow channels decreases with both Dst and MLT. The SAPS carries westward ion flow with a flux magnitude between 3×10^{13} and 3×10^{14} $m^{-2}s^{-1}$ in the F region in a manner nearly invariant to the geomagneic activity level (Erickson et al., 2011).

Regardless of how it is generated through either the voltage or the current generator, this polarization electric field is intense (~50 mV/m) because of low conductivity (Wang et al., 2008) in the subauroral ionosphere, and it drives large sunward ion drifts, with speeds much higher than the neutral wind speeds. Although the ion density is low, substantial frictional heating can develop and considerably raise ion and neutral temperatures, leading to excessive plasma loss due to enhanced rates of charge exchange and recombination reactions, which are temperature-dependent (Schunk et al., 1976). This further reduces conductance over the polarization electric region, provides positive feedback to SAPS electric field, and causes the intensification of the associated ion drifts.

Under the SAPS influence (or a similar influence by the expanded auroral convection as will be further discussed in the following Section 3.3.3.2), the ionospheric plasma convect horizontally sunward with a large flux. This sunward flow moves plasma from the nightside into the dayside. In contrast, the nightside ionosphere does not produce a significant amount of fresh plasma by solar irradiation nor transport sufficient plasma into the region to compensate for this SAPS/convection transportation loss, and therefore the SAPS/convection dynamics likely deeps the main trough. On the dayside, the ionospheric plasma may or may not be accumulated over time by the influx, depending on the sunward gradient

$$\partial(\text{flux})/\partial x = V_{\text{SAPS}}\partial N/\partial x + N\partial V_{\text{SAPS}}/\partial x \tag{3.45}$$

where x is in the sunward direction, N is plasma density, and V_{SAPS} is the SAPS velocity. It is obvious that in the interface region where SAPS is terminated, $|\partial V_{SAPS}/\partial x|$ is maximized, and SAPS most likely contributes to the SED development by providing a horizontal influx gradient. Theoretically, it is possible to infer the approximate SAPS/convection influence region on the SED formation by examining the SED sunward gradient.

SAPS also provides strong forcing on the neutrals via an ion drag effect. The intense sunward ion flows, sometimes up to 1–2 km/s, are much higher than the neutral wind speeds. At midlatitudes, the neutral wind speeds are normally 100–200 m/s or somewhat higher than these but well less than 500 m/s even during periods of neutral wind equatorward surge. Thus SAPS drives neutrals which then continue to spin like a flying wheel. Zonal winds will be strongly westward (Wang et al., 2011; Zhang et al., 2015b). These enhanced westward winds at midlatitude may cause a poleward wind disturbance in certain lag time (e.g., 30–60 min) due to Coriolis forcing (Zhang et al., 2015b). This Coriolis effect contributes to the observed poleward winds following a SAPS event (Fig. 3.25). The frictional heating by SAPS (Zhang et al., 2017) can modify thermospheric composition via local upwelling, in a way very similar to heating in the auroral zone (Wang et al., 2012). Thus local increases in O/N_2 can contribute to SED by enhancing plasma density, and O/N_2 depletion in nearby areas can deplete ionospheric density surrounded the SED and reinforce SED.

3.3.3.2 Influences of other dynamical processes

The subauroral ionospheric electrodynamics is easily affected by the expansion or penetration of high-latitude electric fields. Their zonal and meridional components produce the plasma flow with upward and sunward components at ionospheric heights in the afternoon sector and can make a substantial contribution to the SED plume formation and evolution (Deng and Ridley, 2006; Heelis et al., 2009; Huba et al., 2017; Liu et al., 2016; Lu et al., 2012; Zhang et al., 2017; Zou et al., 2014).

Observations indicate that an eastward electric field may be established accompanying either SAPS or the expansion of auroral convection electric field (Fig. 3.25). At mid- and subauroral latitudes where the magnetic field is inclined, the eastward electric field yields perpendicular ion drift pointing poleward (V_p^N in Fig. 3.21) with a large vertical component; at low and equatorial latitudes, this penetration electric field yields a largely upward ion drift; at high latitudes, this electric field yields poleward drift predominantly in the horizontal direction but with a small vertical component (Deng and Ridley, 2006). This eastward electric field induces a vertical ion drift that pushes plasma upward from low altitudes where charge exchange and recombination rates are fast to high altitudes where these rates are reduced substantially due to their dramatic variation in height. Thus, the eastward electric field effectively enhances the column density as well as electron density in the topside, and reduces the density in the bottomside where refresh solar-

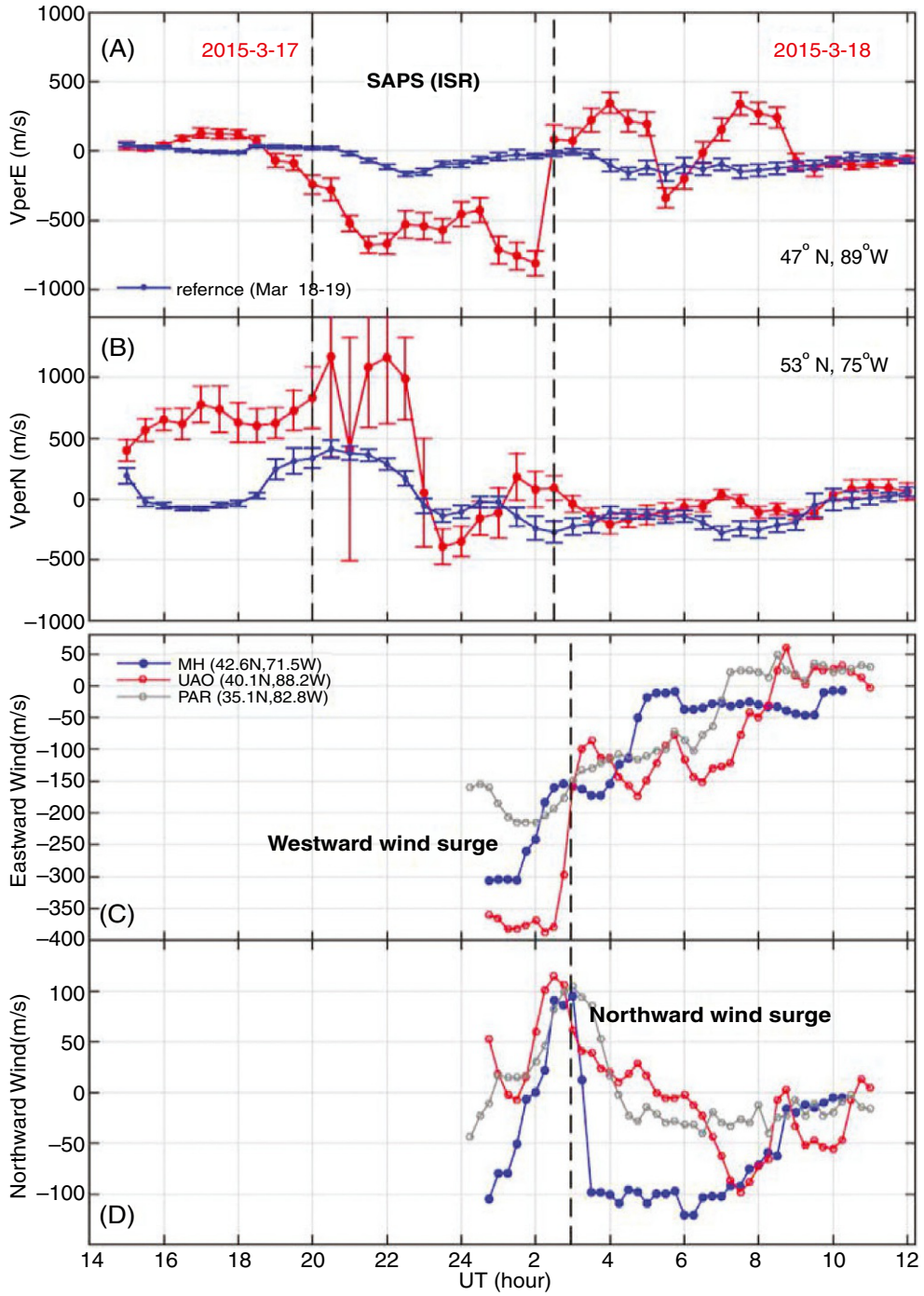

Fig. 3.25 Millstone Hill ISR measurements of plasma drifts (A) **V**perE (perpendicular east) for ∼(89°W, 47°N), (B) **V**perN ($\mathbf{V}_p^N$) (perpendicular north) for ∼(75°W, 53°N), Fabry-Perot Interferometer measurements of (C) eastward neutral winds and (D) meridional neutral winds at Millstone Hill and other nearby midlatitude sites. *Adapted from Figs. 2 and 3 in Zhang, S.-R., Erickson, P.J., Foster, J.C., Holt, J.M., Coster, A.J., Makela, J.J., Noto, J., Meriwether, J.W., Harding, B.J., Riccobono, J., Kerr, R.B., 2015b. Thermospheric poleward wind surge at midlatitudes during great storm intervals. Geophys. Res. Lett. 42 (13), 5132–5140.*

produced plasma could compensate partially for this loss. In short, the vertical component (V_p^z) of V_p^N induced by this electric field can also contribute to the SED development by providing an important plasma source and lifting the F region (Liu et al., 2016). This vertical transport is efficient because, similar to Eq. (3.45), the influx in the ion continuity equation $-\partial(\text{flux})/\partial z = -V_P^z \partial N/\partial z - N\partial V_P^z/\partial z$ will be always positive in the topside with $-\partial N/\partial z > 0$ and $\partial V_P^z/\partial z \sim 0$. The question is, however, the specific shape and magnitude in the gradient of latitudinal profiles of V_P^z variation which is responsible for the characteristic narrow channel of SED. Unless the penetration or expansion of the auroral convection electric field is imposed with a clear boundary, this dynamic forcing alone appears insufficient to account for the key SED plume morphology.

Other factors may affect, contribute to, and perhaps shape the SED formation and evolution. Influences from the storm-time expansion of equatorial ionization anomaly (EIA) to midlatitudes, an equatorward surge of meridional winds (see Section 3.3.2.1), and possibly other processes are among these important factors (Anderson, 1976; Gardner et al., 2018; Horvath and Lovell, 2011; Kelley et al., 2004; Lu et al., 2020; Moldwin et al., 2016). The diversity of these studies clearly demonstrates that the physical mechanism for SED formation remains a very active research frontier.

3.3.4 Polar cap structures and dynamics

The sunward convection entrains the ionospheric plasma in the afternoon sector at subauroral latitudes into the cusp near noon. This region overlaps the open-close field line boundary (OCB) in the magnetosphere. During the period of southward IMF Bz, magnetopause reconnection forcing takes the frozen-in plasma to streamline inward/poleward into the open field line region in the polar cap. At the ionospheric footprint, the poleward (perpendicular to **B**) motion has a vertically upward component that provides uplifting of the plasma to high altitudes where they survive for more time from the chemical loss processes than they would at lower altitudes. If stable IMF Bz southward conditions sustain, the stable antisunward convection in the polar cap carries the plasma originated from the midlatitude plasma such as SED and from particle precipitating effect to travel through the polar cap, forming a tongue of ionization (TOI) structure with elevated ionospheric density elongated along the day-night alignment (Dang et al., 2019; Foster et al., 2005; Hosokawa et al., 2010; Knudsen, 1974; Thomas et al., 2013). The TOI further runs across the nightside OCB where the reconnection forcing at the magnetotail drives the plasma exit from the polar cap and return into auroral latitudes on both dusk and dawn sectors. They continue to flow sunward and complete the large-scale Dungey circulation cycle (Dungey, 1961, 1963; Zhang et al., 2015a) of horizontal plasma transportation at high latitudes (Fig. 3.26).

The TOI occurrence is correlated well with the presence of SED plume; clearly, the SED plume contributes the source plasma to TOI in the polar cap. Of course, even

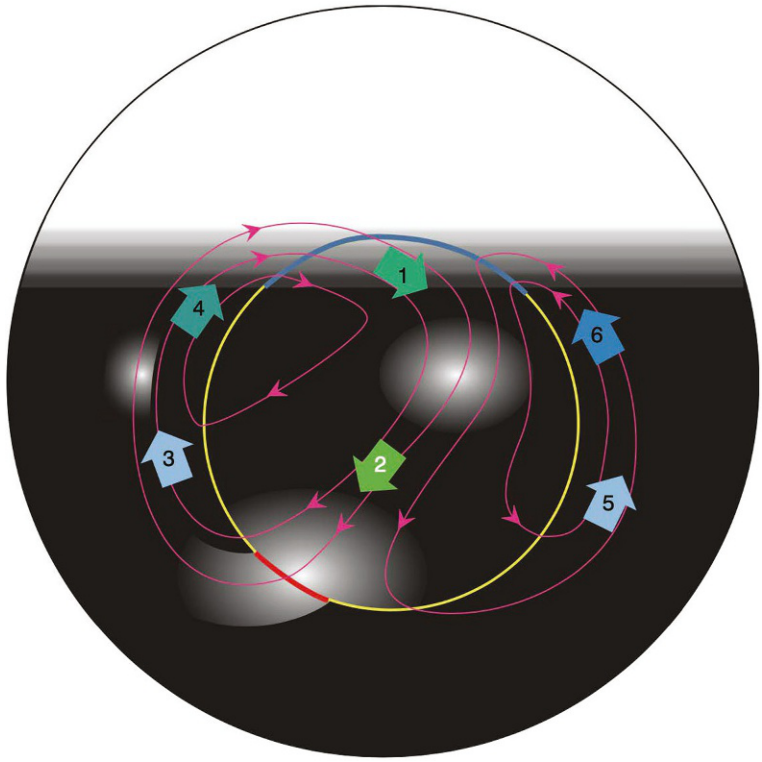

Fig. 3.26 Schematic of the northern polar ionosphere during a substorm growth phase with southward IMF and By $>$ 0. *Blue* and *yellow arc* portions mark the open-close field line boundary (OCB) where plasma entry or exit the polar cap as a result of reconnection forcing at the magnetopause and magnetotail. The dayside *(white)* is solar-produced high-electron area and nightside *(black)* has low-electron density due to a lack of direct solar irradiation. The white spot inside the polar cap is the polar patch, and in the auroral zone is a "blob". *After Zhang, Q.-H., Zhang, B.-C., Lockwood, M., Hu, H.-Q., Moen, J., Ruohoniemi, J.M., Thomas, E.G., Zhang, S.-R., Yang, H.-G., Liu, R.-Y., McWilliams, K.A., Baker, J.B.H., 2013. Direct observations of the evolution of polar cap ionization patches. Science 339 (6127), 1597–1600. https://doi.org/10.1126/science.1231487.*

without SED, TOI could still develop through entraining midlatitude or cusp plasma by the enhanced convection. The IMF conditions play an important role in the polar cap plasma dynamics and structures, affecting plasma entry cross the dayside OCB, transpolar antisunward convection, and exit from the polar cap cross the nightside OCB. When Bz is southward turning or subject to substantial variations, the continuous plasma flow is possibly segmented into patches of small-scale-enhanced plasma density clouds in the polar cap.

Several segmentation processes resulting from IMF variations are plausible. The convection pattern expansion, distortion, speed change, and other variations associated with

transient dayside magnetic reconnection due to IMF changes in Bz and sometimes in By can create inhomogeneity in forcing on the ionospheric plasma (Lockwood and Carlson, 1992; Rodger et al., 1994). The development of plasma flow channels leading to enhanced ion-neutral collision and heating can enhance the chemical loss and therefore "meltdown" plasma within the channel and eventually form separated density structures (Ren et al., 2020). When formed, these patches are often mesoscale usually spanning 200–1000 km in longitude and 2–3 degrees wide in latitude (Rodger et al., 1994; Weber et al., 1984), and can be 200% above the nearby background ionospheric density (Crowley, 1996).

Similar to a TOI, they undergo transpolar antisunward flow, exit from the polar cap and return to the auroral zone. Insider the aurora latitude, they are named as "blobs" (Rodger et al., 1986) (Fig. 3.26).

3.3.5 Main ionospheric trough

The main ionospheric trough, also termed midlatitude ionospheric trough, is a plasma depletion structure in the nighttime F region and topside ionosphere at subauroral latitudes. The main trough occurs for all levels of geomagnetic activity, and its electron density around 300 km can be as low as 10^3 cm^{-3} during quiet geomagnetic conditions, which is significantly lower compared with its adjacent poleward and equatorward regions (Brinton et al., 1978). As is shown in Fig. 3.27, the main trough normally situates between the footprints of the plasmaspheric boundary layer and the equatorward boundary of the auroral oval, spanning a narrow latitudinal extent for only few degrees, but covering an extended longitudinally range for several hours of local time from dusk to dawn (Carpenter and Lemaire, 2004; Moffett and Quegan, 1983; Pierrard and Voiculescu, 2011; Rodger et al., 1992).

There are three major components of a main trough: (1) a sharp poleward edge, which is mainly formed by additional local ionization at both E and F region due to auroral particle precipitation and/or partially by the high-density plasma transportation across the polar cap from the dayside, i.e., boundary blobs (Rodger et al., 1986); (2) a less-steep equatorward edge, which is usually formed by the replenishment of plasma from the nightside plasmasphere (Yizengaw and Moldwin, 2005) and/or built by the sunlit midlatitude plasma that gradually decays as it corotates into the darkness (Voiculescu et al., 2010); (3) the trough minimum region between the two edges mentioned above, where the plasma density depletion can exceed an order of magnitude in the ionospheric F region.

Since first identified by a topside sounder (Muldrew, 1965), the main trough has been extensively studied for several decades via different observational and modeling techniques (see the review by Rodger (2008) and references therein). The strong density gradient in the trough area can significantly affect the propagation of

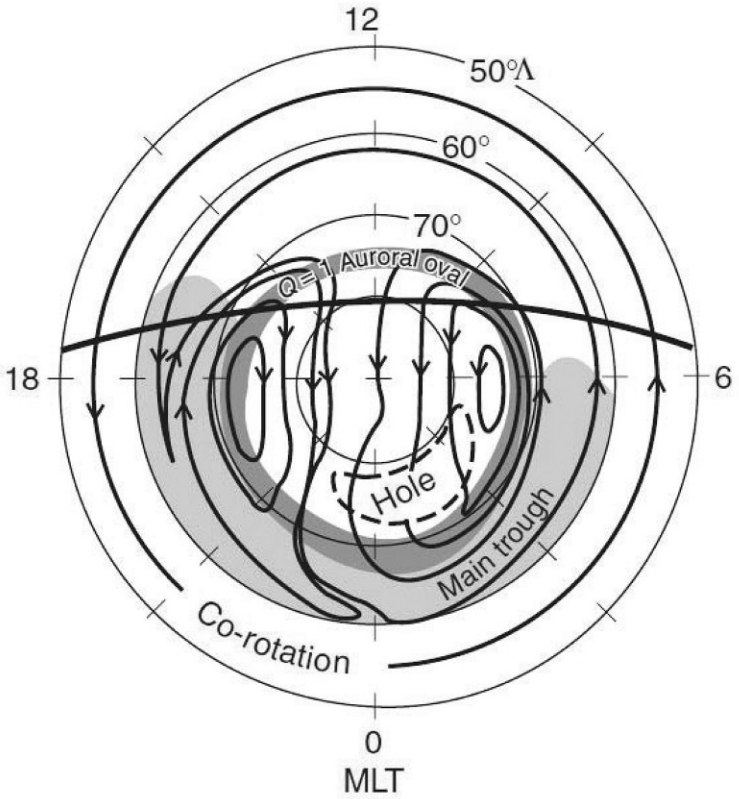

Fig. 3.27 A schematic diagram of the Earth's polar region showing the main trough location in a MLT and invariant latitude. Also shown are the two-cell plasma convection trajectories at 300 km *(solid lines)*, the corotation flow, the quiet-time auroral oval, and the high-latitude ionization hole. *After Brinton, H.C., Grebowsky, J.M., Brace, L.H., 1978. The highlatitude winter F region at 300 km: thermal plasma observations from AE-C. J. Geophys. Res. Space Phys. 83 (A10), 4767–4776. https://doi.org/10.1029/JA083iA10p04767*.

transionospheric radio signals. In addition, the trough edges are often regions of high plasma irregularity occurrence that can impose detrimental effects on modern navigation and communication systems, such as GNSS and Wide Area Augmentation System (WAAS). Thus, the fine structures and dynamic variation of the main trough are of great space weather importance. The content of this section will focus on three objectives: (1) to explain the fundamental formation mechanisms of the main trough, (2) to summarize the major temporal and spatial characteristics of the main trough, and (3) to highlight some of the recent scientific progresses associated with the main trough.

3.3.5.1 Trough formation mechanisms

Stagnation mechanism

The upper atmosphere is partially ionized, and the ion-neutral collision is frequent and cannot be neglected. Thus, in the low and midlatitude region, the neutral thermosphere particles that corotate with Earth also bring the ionospheric plasma into corotation via ion-neutral collisions, which is equivalent to a corotation electric field that directs radially inward in an inertial reference (Baumjohann and Treumann, 1996). On the other hand, the high-latitude ionosphere is dominated by the solar wind-induced convection electric field with a strong duskward component. Fig. 3.28 shows a schematic illustration of the total electric potential given by the sum of convection and corotation electric field in the equatorial plane. A stagnation point (the equipotential contour crosses itself) can be found in the duskside plasmapause where the convection and corotation electric fields are approximately oppositely directed with the same value.

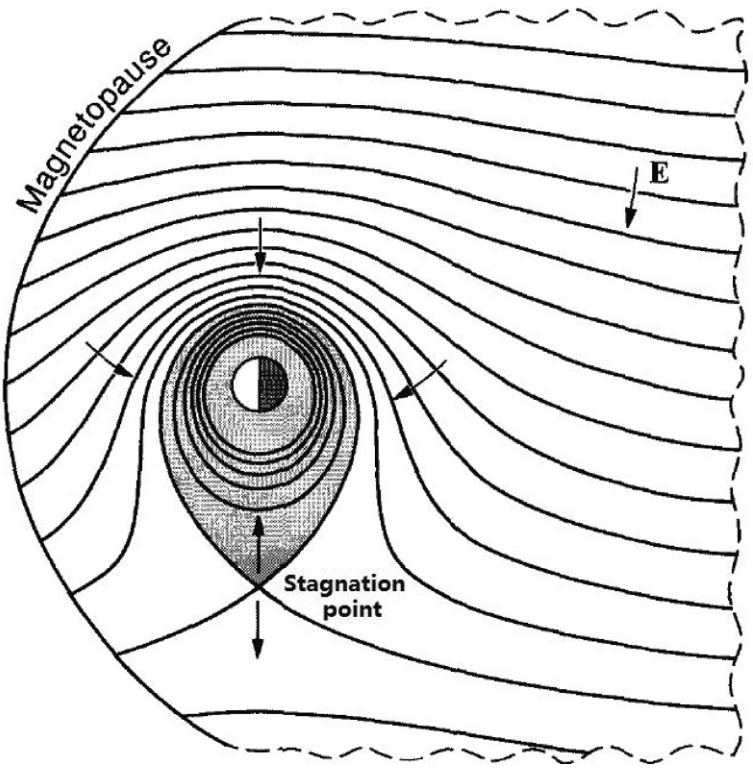

Fig. 3.28 A schematic illustration of the electric equipotential contours in the equatorial plane. The shaded area represents the plasmasphere. *After Berlok, T., Pfrommer, C., 2019. On the Kelvin-Helmholtz instability with smooth initial conditions-linear theory and simulations. Mon. Not. R. Astron. Soc. 485 (1), 908–923.*

The generation of the main trough can be traced to the footprints of the plasmapause around the stagnation point, i.e., the low-speed subauroral ionosphere in the dusk sector to the east of sunset terminator. In this plasma stagnation area, the westward convection returning flow counteracts with the eastward corotation flow. As a result, the plasma in this region has a longer residence time in darkness than at lower latitudes, and the prolonged recombination processes therein cause the plasma density decay to very low levels to form the main trough (Nilsson et al., 2005; Spiro et al., 1978). Eventually, the low-density plasma could slowly drift out of this quasi-stagnation area and extend to the whole night sector that corotates and/or convects toward dawn. Moreover, the convection flow could transport a low influx into the dayside sector, sometimes forming a dayside trough (Pryse et al., 1998; Rodger et al., 1992; Whalen, 1989).

Subauroral ion heating mechanism

During geomagnetically active periods, the morphology and dynamics of the main trough can be greatly complicated by the spatiotemporal variation of electric fields in the vicinity of subauroral ionosphere, and the existence of SAPS, which is extensively discussion in Section 3.3.3.1.

As pointed out earlier, SAPS-driven ion velocities are significantly larger than neutral wind velocities. Thus, the ion temperature in the vicinity of SAPS will be increased considerably due to enhanced ion-neutral frictional heating (Zhang et al., 2017), which in turn accelerates the ion loss process via the following charge exchange reaction (Schunk et al., 1976):

$$N_2 + O^+ = NO^+ + N, \tag{3.46}$$

where the resulted molecular ion, NO^+, has much faster recombination rate with electrons than that of O^+ (Schunk and Nagy, 2000). This leads to rapid depletion of ionization and thus a deep trough can be quickly formed. It should be noted that this plasma loss process can be highly nonlinear. As can be seen from Fig. 3.29, when the relative ion-neutral velocity increases from 1 to 2 km/s, the rate coefficients of the loss process from O^+ to N_2 as mentioned above will rise by one order of magnitude (Rodger, 2008; Schunk et al., 1976). Moreover, the enhanced frictional heating and associated plasma thermal expansion will cause field-aligned plasma upflow, which also contributes to the formation of the main trough (Anderson et al., 1991; Voiculescu and Roth, 2008).

3.3.5.2 Morphology and dynamics of the main trough

Diurnal variation: Although the main trough can drift into the dayside ionosphere, it is basically a nocturnal phenomenon that longitudinally extends from dusk to dawn and is limited mainly between 55 and 65 degrees of geomagnetic latitude (MLAT) to the equatorward side of the auroral oval. The trough minimum position normally occurs at higher latitudes in the afternoon sector and migrates to lower latitudes with a later

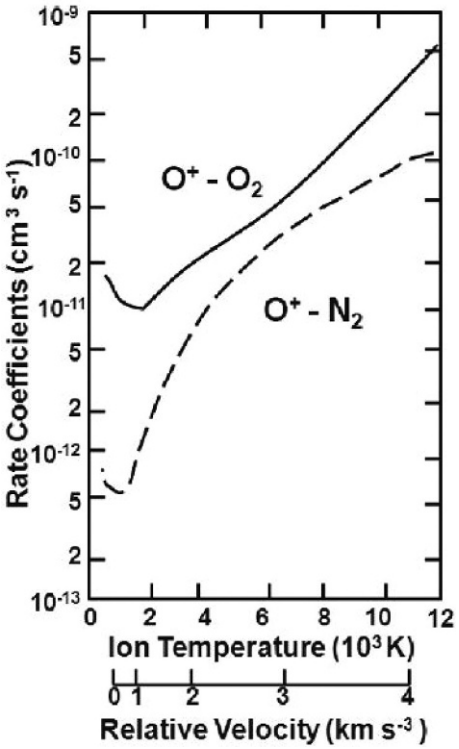

Fig. 3.29 Rate coefficients for the two major loss reactions at F layer as a function of ion temperature and velocity in the rest frame of the neutral particles. *After Rodger, A.S., 2008. The Mid-Latitude Trough—Revisited, Geophysical Monograph Series, vol. 181. American Geophysical Union, Washington, DC, pp. 25–33. https://doi.org/10.1029/181GM04.*

MLT. It usually reaches its equatorward-most position in the early morning hours (02–04 MLT) and then quickly retreats back to higher latitudes (Karpachev, 2003; Lee et al., 2011; Mallis and Essex, 1993; Werner and Prölss, 1997).

Seasonal and hemispheric variation: The main trough is primarily observed in winter and equinoxes. Under the polar night and quietest geomagnetic conditions, the trough can be seen at all local times around midwinter. In summer, however, the trough is less common, exhibiting a very limited occurrence centered around midnight (Horvath and Essex, 2003; Rodger, 2008). A trough tends to occur at higher latitudes with broader width in winter than those in summer (Karpachev, 2003; Voiculescu et al., 2006). In addition, there is also a hemispheric asymmetry, in that the Northern Hemisphere has a higher trough occurrence rate than the Southern Hemisphere during winter and equinoctial periods. This is due to the smaller offset between the geomagnetic and geographic poles in the Northern Hemisphere, which makes the trough zone taken as a whole closer to the darkness in the winter/equinoctial time (Aa et al., 2020).

Longitudinal variation: The location of the main trough exhibits strong longitudinal dependence. Typically, the deepest trough is located to the west of the geomagnetic poles, which is around 130°W in the Northern Hemisphere and around 60°E in the Southern Hemisphere. The trough usually occurs at a higher latitude in the longitudinal sector that contains the magnetic pole (He et al., 2011; Karpachev et al., 2019). Moreover, the trough distribution exhibits clear east-west hemispherical preferences. Fig. 3.30 shows that the trough has a higher occurrence rate in eastern longitudes during the December solstice and in western longitudes during the June solstice. These longitudinal variations are caused by the illumination difference along a fixed MLAT line within the trough due to Earth's rotation and the offsets between the geographic and geomagnetic poles. For instance, in the December solstice, the eastern longitudes along 62 degrees MLAT are closer to the polar night in Northern Hemisphere and far from the polar day in Southern Hemisphere than their western counterparts, thus the trough therein is likely to have a higher occurrence rate.

Geomagnetic and solar cycle dependence: The trough shifts progressively toward lower latitudes with increasing geomagnetic activity due to the expansion of auroral oval (Prölss, 2007; Werner and Prölss, 1997; Zou et al., 2011). The trough tends to have a higher occurrence rate and becomes deeper during geomagnetically active times due to the enhancement of subauroral electric field and associated plasma heating as mentioned above. Conditions for the trough occurrence are more favored in low solar activity periods, and the trough depth were found to increase with the 10.7-cm solar radiation flux F10.7 (Ishida et al., 2014; Karpachev et al., 2019; Yang et al., 2015).

3.4 Conclusion

3.4.1 Conclusion of Section 3.1

F-region plasma density irregularities have been the focus of M-I-T coupling research for over. Every year, new and exciting discoveries are made regarding their generation mechanisms, characteristics and morphology, effects on technology, and overall role in the coupled M-I-T system. By and large, this scientific progress is driven by advances in geospace sensor technology, including in situ and remote techniques, which were discussed earlier, and the proliferation of these sensors throughout the high-latitude region.

There is no sign that interest in the high-latitude regions and its plasma density irregularities is subsiding. In fact, it appears that, at least anecdotally, the opposite is occurring. Without question, there is a clear societal need for future scientific investigations. Commercial airlines that are seeking to shorten long-haul flights using transpolar routes are becoming more reliant on radio communications that are vulnerable to irregularities and associated phenomena. Furthermore, as the high-latitude waterways open up due to the decline in ice coverage, long-range maritime monitoring and navigation will

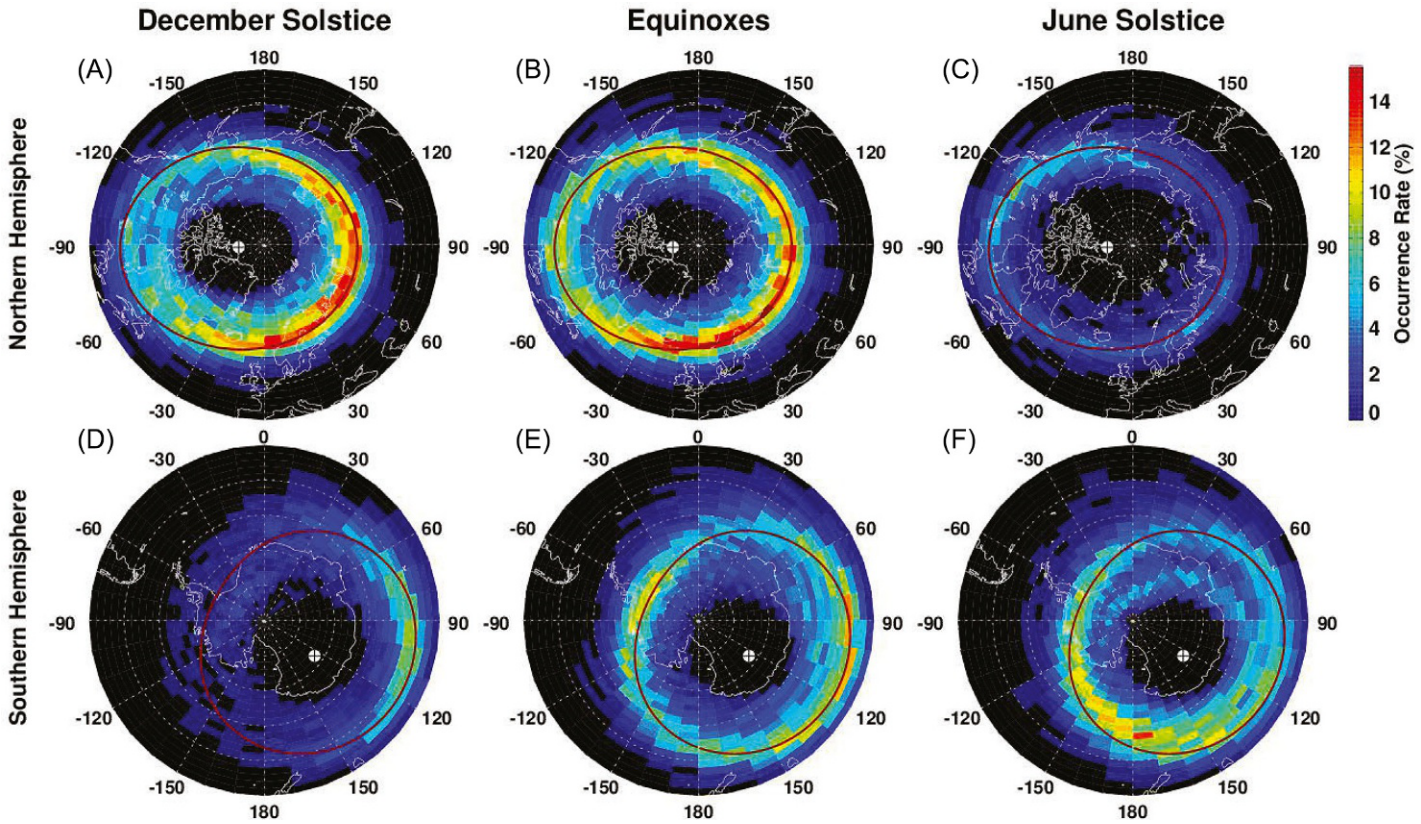

Fig. 3.30 Geographic polar view of the main trough occurrence rate at 400–500 km for both hemispheres under different seasons. The concentric circles are plotted in 10 degrees interval with outermost one representing latitude of 40 degrees. The geomagnetic poles are marked with *crosses*. The $\pm$62 degrees MLAT lines are also plotted in *solid red lines*. *After Aa, E., Zou, S., Erickson, P.J., Zhang, S.-R., Liu, S., 2020. Statistical analysis of the main ionospheric trough using Swarm in situ measurements. J. Geophys. Res. Space Phys. 125 (3), e2019JA027583.*

become more common, requiring a more detailed and reliable understanding of the signal propagation characteristics in the region.

From our perspective, the amount of valuable scientific data that has been generated by the abundance and variety of sensors in the high-latitude regions has, by far, outpaced their assimilation and transformation into new knowledge by inquiring scientists. Undoubtedly, the necessary measurements for resolving the question of the dominant generation mechanism for plasma density enhancements have already been collected—they only have to be pieced together. Other outstanding questions, like those related to the instability mechanisms associated with plasma irregularities, may be out of reach of experiment until more highly resolved and insightful measurement techniques become available.

It is without question that we, as solar-terrestrial physicists, have only scratched the surface on understanding the interconnections within the M-I-T system. Indeed, two major conclusions of our collective efforts and progress in resolving finer spatial scale and faster cadences are that, first, influential M-I-T coupling phenomena are transpiring across multiple spatiotemporal scales. Second, the phenomena have major impacts on the M-I-T from bottomside F-region ionosphere all the way out to the distant reaches of the terrestrial magnetotail.

3.4.2 Concluding remarks and future work of Section 3.2

This review has focused on theories and simulations of high-latitude ionospheric density irregularities and the role these play in altering the terrestrial radio propagation environment, specifically through refractive and diffractive effects collectively referred to herein as "scintillation" resulting in fluctuations in radio signals. Prior reviews concerning observations and theories of ionospheric structures have been discussed and summarized. These are mostly conducted under the framework of linear theory, whereas the present review article focuses on the nonlinear evolution of ionospheric instabilities. Because scintillation occurs from structures at $\sim$100 m scales and above, the features of such density structures and how they affect propagation are inherently the product of nonlinear cascading/steepening processes.

To motivate discussions of GDI and KHI we first summarize salient work on the linear theory of these instabilities. As shown in this section, linear theory is valuable for quick interpretations of data and is also an important validation point for more complicated nonlinear simulations. We review recent nonlinear simulation work and then provide a set of reproducible simulation examples, using the GEMINI model, for the reader to access and run those optionally. These examples illustrate some important properties of the instability nonlinear behavior, namely the sensitivity to parameters like background conductance (precipitation) and inertial capacitance (amount of MI coupling).

Ionospheric instabilities, such as KHI and GDI can cause scintillation-scale structures which cause fluctuations in the radio signals observed on the ground. We review the theory of how the propagation through the turbulent ionosphere can be simulated and mapped to signal fluctuations on the ground. We also emphasize how the physics-based models, such as GEMINI-SIGMA, can simulate the scintillations during different growth stages of instabilities. We briefly discuss the scintillation signatures related to different instabilities and review inverse analysis to retrieve physics of ionosphere from the observed scintillations on the ground. We also touch upon scale-dependent scintillations and HF effects. Finally, we present some of the challenges and unresolved issues in instability and scintillation studies, and make some suggestions for fruitful future work to advance this field.

3.4.3 Concluding remarks of Section 3.3

We have provided an overview on the substantial electron density gradients in the ionosphere with focus on their fundamental morphology. Many of these have been known for several decades, however, it is only until recent years the observational coverage in subauroral and high altitudes has dramatically improved, especially due to the use of GNSS TEC, SuperDARN, ISRs, All-sky Imagers, and other radio and optical technologies. Coupling models with magnetosphere, ionosphere, and thermosphere components are more and more capable due to improved resolution and specification of essential drivers. It is fair to state, however, that there are still very significant knowledge gaps. The SED morphology, its dependency on solar-terrestrial drivers, and its evolution in space and time are not well established. Furthermore, the known physics processes, which could be subject to variability from storm to storm, remain highly debatable. There are also some renewed interests in the main midlatitude trough, particularly, its relationship with the SAPS presence and SED location. We believe research toward improved understanding of the ionospheric large gradients will be staying very active as one of the frontiers of geospace coupling and systems science.

Acknowledgments

Section 3.1

This work is dedicated to Dr. Jean-Pierre St. Maurice, our mentor. We stand on his shoulders. LVG is supported by the NASA Living With a Star Jack Eddy Postdoctoral Fellowship Program, administered by UCAR's Cooperative Programs for the Advancement of Earth System Science (CPAESS) under award #NNX16AK22G.

This material is based upon work supported by the Resolute Bay Observatory, which is a major facility funded by the National Science Foundation through cooperative agreement AGS-1840962 to SRI International. RISR-C is funded by the Canada Foundation for Innovation and led by the University of Calgary's Auroral Imaging Group, in partnership with UofC Geomatic Engineering, University of Saskatchewan, Athabasca University and SRI International (http://aurora.phys.ucalgary.ca/resu/). RISR-C data are available from http://data.phys.ucalgary.ca/ and https://madrigal.phys.ucalgary.ca/.

Section 3.2

KD was supported by NSF grants 1651410 (for work on propagation modeling theory and inverse technique) and NSF CAREER grant AGS-1848207 (for work on scintillation signatures through different types on instability in the cusp and polar cap).

Development of the GEMINI model was supported by NSF CAREER grant AGS-1255181 (supporting MZ) and NASA HDEE grant 80NSSC20K0176 (supporting MH).

AS acknowledges funding support from the Research Council of Norway, grant number 275653.

The material on current and future ISR observations, contributed by LL, is based on work supported by the Resolute Bay Observatory which is a major facility funded by the National Science Foundation through cooperative agreement AGS-1840962 to SRI International. EISCAT is an international association supported by research organisations in China (CRIRP), Finland (SA), Japan (NIPR and ISEE), Norway (NFR), Sweden (VR), and the United Kingdom (UKRI).

We also acknowledge NSF collaborative grants AGS-2027308 (LL) and AGS-2027300 (MZ,KD, and MR) which contributed to development of many of the ideas presented in this article.

Finally, MZ and KD gratefully acknowledge use of the ERAU VEGA supercomputing system for some of the simulations presented in this article.

Section 3.3

This work was supported by AFOSR MURI project FA9559-16-1-0364, ONR grant N00014-17-1-2186, and NSF awards AGS-1952737 and AGS-2033787.

Appendix: Simulation software used for examples in Section 3.2

This section presents results from basic, reproducible simulations that illustrate some important features of the linear and nonlinear evolution of GDI and KHI. The model used to generate the results, GEMINI (Zettergren and Semeter, 2012; Zettergren and Snively, 2015; Zettergren et al., 2015), is freely available to the readers, who can download the source code, compile it, and generate results similar to those presented in this paper (or extend these examples for their own work). These examples can be run by the reader by installing the GEMINI ionospheric model repositories, which can be downloaded from https://github.com/gemini3d/. The examples used for this article (Zettergren and Hirsch, 2020) have additional documentation explaining their use under these directories:

- GDI: INIT/GDI_PERIODIC_LOWRES?
- KHI: INIT/KHI_PERIODIC_LOWRES?

The example scripts for basic simulations will run on a typical laptop or desktop computer running Linux, MacOS or Windows. An HPC will reduce the processing time according to the number of CPUs available; the code scales efficiently up to at least hundreds of cores. Software requirements are

- FORTRAN 2008 COMPILER (GCC OR INTEL FORTRAN)?
- PYTHON OR MATLAB®?

Our testing indicates that an Intel i7 quad-core CPU runs the example GDI simulation in less than 2 h. The example KHI simulation takes about 2.5 h on a 16-core Intel Skylake HPC CPU.

The numerical core of GEMINI is written in object-oriented Fortran 2018. A high-level view of the software library interfaces is shown in Fig. 3.31.

GEMINI uses sparse and linear algebra libraries MUMPS (Amestoy et al., 2019), ScaLAPACK (Blackford et al., 1997) and LAPACK (Anderson et al., 1999), and benefits from using an MPI-2 (Gropp et al., 1999)

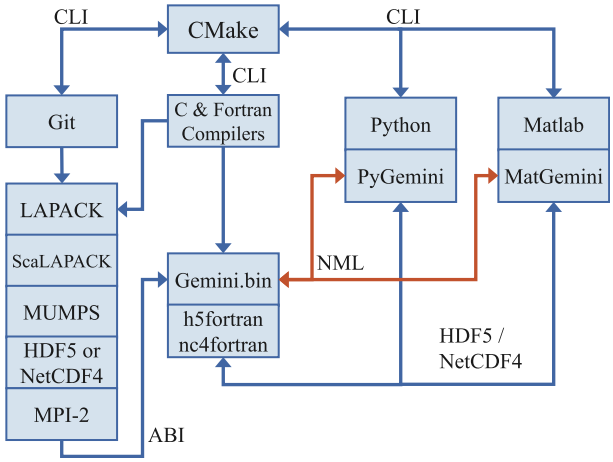

Fig. 3.31 GEMINI3D software suite interconnections.

message passing interface such as OpenMPI, MPICH, Intel MPI, MS-MPI, etc. to enable domain parallelization. GEMINI can also run without an MPI library using a single CPU core. Data input and output files use the HDF5 (Folk et al., 2011) format. Configuration parameters and metadata are communicated via plain-text, Fortran standard Namelist (NML) files.

Care has been taken to remain agnostic of the compiler, operating system, and CPU architecture throughout the GEMINI software stack. This also applies to the Python interface to GEMINI (PyGemini (Hirsch, 2020)) and the MATLAB interface (MatGemini (Hirsch and Zettergren, 2020)). PyGemini and MatGemini each automatically determine the optimal grid—worker partitioning to maximize CPU core usage. Over 100 unit tests and project registration tests are built-in and run automatically upon first install. This helps identify problems with the user's software stack. Gemini3D will attempt to download and build missing or incompatible libraries. Plotting and utility scripts exist independently in Python and MATLAB (Hirsch, 2020; Hirsch and Zettergren, 2020).

The main scripting frontend program "gemini3d.run" generates a Namelist NML file and HDF5 files containing the simulation initialization data. "gemini3d.run" can auto-generate an HPC job file or run the simulation on the local computer. A second program "gemini3d.plot" generates numerous plots per simulation time step.

The script for generating Fig. 3.13 (Zettergren and Hirsch, 2020) is run from MATLAB function:

```
gemscr.postprocess.GDIgrowth?
```

References

Aa, E., Zou, S., Erickson, P.J., Zhang, S.-R., Liu, S., 2020. Statistical analysis of the main ionospheric trough using Swarm in situ measurements. J. Geophys. Res. Space Phys. 125 (3). e2019JA027583.

Aarons, J., 1982. Global morphology of ionospheric scintillations. IEEE Proc. 70, 360–378.

Aarons, J., 1993. The longitudinal morphology of equatorial F-layer irregularities relevant to their occurrence. Space Sci. Rev. 63 (3–4), 209–243. https://doi.org/10.1007/BF00750769.

Aarons, J., 1997. Global positioning system phase fluctuations at auroral latitudes. J. Geophys. Res. Space Phys. 102 (A8), 17219–17231. https://doi.org/10.1029/97JA01118.

Akasofu, S.I., 1968. Polar and Magnetosphere Substorms. vol. 11 Astrophysics and Space Science Library, Springer, https://doi.org/10.1007/978-94-010-3461-6.

Alfonsi, L., Spogli, L., De Franceschi, G., Romano, V., Aquino, M., Dodson, A., Mitchell, C.N., 2011. Bipolar climatology of GPS ionospheric scintillation at solar minimum. Radio Sci. 46 (3). https://doi.org/10.1029/2010RS004571.

Amestoy, P.R., Buttari, A., L'Excellent, J.-Y., Mary, T., 2019. Performance and scalability of the block low-rank multifrontal factorization on multicore architectures. ACM Trans. Math. Softw. 45, 2:1–2:26.

Anderson, D.N., 1976. Modeling the midlatitude F-region ionospheric storm using east-west drift and a meridional wind. Planet. Space Sci. 24 (1), 69–77. https://doi.org/10.1016/0032-0633(76)90063-5.

Anderson, P.C., Heelis, R.A., Hanson, W.B., 1991. The ionospheric signatures of rapid subauroral ion drifts. J. Geophys. Res. Space Phys. 96 (A4), 5785–5792. https://doi.org/10.1029/90JA02651.

Anderson, E., Bai, Z., Bischof, C., Blackford, S., Demmel, J., Dongarra, J., Du Croz, J., Greenbaum, A., Hammarling, S., McKenney, A., Sorensen, D., 1999. LAPACK Users' Guide, third ed. Society for Industrial and Applied Mathematics, Philadelphia, PA.

Bahcivan, H., Tsunoda, R., Nicolls, M., Heinselman, C., 2010. Initial ionospheric observations made by the new resolute incoherent scatter radar and comparison to solar wind IMF. Geophys. Res. Lett. 37 (15), L15103. https://doi.org/10.1029/2010GL043632.

Basu, S., Basu, S., Hanson, W.B., 1981. The role of in-situ measurements in scintillation modelling. In: Symposium on the Eect of the Ionosphere on Radiowave Systems.

Basu, S., Basu, S., MacKenzie, E., Coley, W.R., Hanson, W.B., Lin, C.S., 1984. F region electron density irregularity spectra near auroral acceleration and shear regions. J. Geophys. Res. Space Phys. 89 (A7), 5554–5564. https://doi.org/10.1029/JA089iA07p05554.

Basu, S., Basu, S., MacKenzie, E., Whitney, H.E., 1985. Morphology of phase and intensity scintillations in the auroral oval and polar cap. Radio Sci. 20 (3), 347–356. https://doi.org/10.1029/RS020i003p00347.

Basu, S., Basu, S., MacKenzie, E., Fougere, P.F., Coley, W.R., Maynard, N.C., Winningham, J.D., Sugiura, M., Hanson, W.B., Hoegy, W.R., 1988. Simultaneous density and electric field fluctuation spectra associated with velocity shears in the auroral oval. J. Geophys. Res. Space Phys. 93 (A1), 115–136. https://doi.org/10.1029/JA093iA01p00115.

Basu, S., Basu, S., Weber, E.J., Coley, W.R., 1988. Case study of polar cap scintillation modeling using DE 2 irregularity measurements at 800 km. Radio Sci. 23 (4), 545–553. https://doi.org/10.1029/RS023i004p00545.

Basu, S., Basu, S., MacKenzie, E., Coley, W.R., Sharber, J.R., Hoegy, W.R., 1990. Plasma structuring by the gradient drift instability at high latitudes and comparison with velocity shear driven processes. J. Geophys. Res. Space Phys. 95 (A6), 7799–7818. https://doi.org/10.1029/JA095iA06p07799.

Basu, S., Basu, S., Chaturvedi, P.K., Bryant Jr, C.M., 1994. Irregularity structures in the cusp/cleft and polar cap regions. Radio Sci. 29 (1), 195–207. https://doi.org/10.1029/93RS01515.

Basu, S., Weber, E.J., Bullett, T.W., Keskinen, M.J., MacKenzie, E., Doherty, P., Sheehan, R., Kuenzler, H., Ning, P., Bongiolatti, J., 1998. Characteristics of plasma structuring in the cusp/cleft region at Svalbard. Radio Sci. 33 (6), 1885–1899. https://doi.org/10.1029/98RS01597.

Basu, S., Basu, S., Valladares, C.E., Yeh, H.-C., Su, S.-Y., MacKenzie, E., Sultan, P.J., Aarons, J., Rich, F.J., Doherty, P., Groves, K.M., Bullett, T.W., 2001. Ionospheric effects of major magnetic storms during the international space weather period of September and October 1999: GPS observations, VHF/UHF scintillations, and in situ density structures at middle and equatorial latitudes. J. Geophys. Res. Space Phys. 106 (A12), 30389–30413. https://doi.org/10.1029/2001JA001116.

Baumjohann, W., Treumann, R.A., 1996. Basic Space Plasma Physics. Imperial College, London.

Berlok, T., Pfrommer, C., 2019. On the Kelvin-Helmholtz instability with smooth initial conditions-linear theory and simulations. Mon. Not. R. Astron. Soc. 485 (1), 908–923.

Bernhardt, P.A., Siefring, C.L., 2006. New satellite-based systems for ionospheric tomography and scintillation region imaging. Radio Sci. 41 (5), RS5S23. https://doi.org/10.1029/2005RS003360.

Bhattacharyya, A., Yeh, K.C., Franke, S.J., 1992. Deducing turbulence parameters from transionospheric scintillation measurements. Space Sci. Rev. 61 (3-4), 335–386. https://doi.org/10.1007/BF00222311.

Blackford, L.S., Choi, J., Cleary, A., D'Azevedo, E., Demmel, J., Dhillon, I., Dongarra, J., Hammarling, S., Henry, G., Petitet, A., Stanley, K., Walker, D., Whaley, R.C., 1997. ScaLAPACK Users' Guide. Society for Industrial and Applied Mathematics, Philadelphia, PA.

Briggs, B.H., 1964. Observations of radio star scintillations and spread-F echoes over a solar cycle. J. Atmos. Terr. Phys. 26 (1), 1–23. https://doi.org/10.1016/0021-9169(64)90104-7.

Briggs, B.H., 1975. Ionospheric irregularities and radio scintillations. Contemp. Phys. 16, 469–488. https://doi.org/10.1080/00107517508210825.

Brinton, H.C., Grebowsky, J.M., Brace, L.H., 1978. The high-latitude winter F region at 300 km: thermal plasma observations from AE-C. J. Geophys. Res. Space Phys. 83 (A10), 4767–4776.

Brinton, H.C., Grebowsky, J.M., Brace, L.H., 1978. The high-latitude winter F region at 300 km: thermal plasma observations from AE-C. J. Geophys. Res. Space Phys. 83 (A10), 4767–4776. https://doi.org/10.1029/JA083iA10p04767.

Bristow, W.A., Jensen, P., 2007. A superposed epoch study of SuperDARN convection observations during substorms. J. Geophys. Res. Space Phys. 112 (A6).

Buonsanto, M.J., 1999. Ionospheric storms—a review. Space Sci. Rev. 88, 563–601. https://doi.org/10.1023/A:1005107532631.

Burston, R., Astin, I., Mitchell, C., Alfonsi, L., Pedersen, T., Skone, S., 2009. Correlation between scintillation indices and gradient drift wave amplitudes in the northern polar ionosphere. J. Geophys. Res. Space Phys. 114 (A7). https://doi.org/10.1029/2009JA014151.

Burston, R., Astin, I., Mitchell, C., Alfonsi, L., Pedersen, T., Skone, S., 2010. Turbulent times in the northern polar ionosphere? J. Geophys. Res. Space Phys. 115 (A4). https://doi.org/10.1029/2009JA014813.

Burston, R., Mitchell, C., Astin, I., 2016. Polar cap plasma patch primary linear instability growth rates compared. J. Geophys. Res. Space Phys. 121 (4), 3439–3451. https://doi.org/10.1002/2015JA021895.

Carlson, H.C., 2012. Sharpening our thinking about polar cap ionospheric patch morphology, research, and mitigation techniques. Radio Sci. 47 (4), RS0L21. https://doi.org/10.1029/2011RS004946.

Carlson, H.C., Oksavik, K., Moen, J., Pedersen, T., 2004. Ionospheric patch formation: direct measurements of the origin of a polar cap patch. Geophys. Res. Lett. 31 (8), L08806. https://doi.org/10.1029/2003GL018166.

Carlson, H.C., Pedersen, T., Basu, S., Keskinen, M., Moen, J., 2007. Case for a new process, not mechanism, for cusp irregularity production. J. Geophys. Res. Space Phys. 112 (A11). https://doi.org/10.1029/2007JA012384.

Carlson, H.C., Oksavik, K., Moen, J., 2008. On a new process for cusp irregularity production. Ann. Geophys. 26 (9), 2871–2885. https://doi.org/10.5194/angeo-26-2871-2008.

Carpenter, D., Lemaire, J., 2004. The plasmasphere boundary layer. Ann. Geophys. 22 (12), 4291–4298. https://doi.org/10.5194/angeo-22-4291-2004.

Carrano, C.S., Rino, C.L., 2019. Irregularity parameter estimation for interpretation of scintillation doppler and intensity spectra. In: 2019 United States National Committee of URSI National Radio Science Meeting (USNC-URSI NRSM), pp. 1–2.

Carrano, C.S., Groves, K.M., Caton, R.G., 2012. Simulating the impacts of ionospheric scintillation on L band SAR image formation. Radio Sci. 47. https://doi.org/10.1029/2011RS004956.

Cerisier, J.C., Berthelier, J.J., Beghin, C., 1985. Unstable density gradients in the high-latitude ionosphere. Radio Sci. 20 (4), 755–761. https://doi.org/10.1029/RS020i004p00755.

Chartier, A., Forte, B., Deshpande, K., Bust, G., Mitchell, C., 2016. Three-dimensional modeling of high-latitude scintillation observations. Radio Sci. 51 (7), 1022–1029. https://doi.org/10.1002/2015RS005889.

Chartier, A.T., Mitchell, C.N., Miller, E.S., 2018. Annual occurrence rates of ionospheric polar cap patches observed using Swarm. J. Geophys. Res. Space Phys. 123 (3), 2327–2335. https://doi.org/10.1002/2017JA024811.

Chartier, A.T., Huba, J.D., Mitchell, C.N., 2019. On the annual asymmetry of high-latitude sporadic F. Space Weather 17 (11), 1618–1626. https://doi.org/10.1029/2019SW002305.

Chernyshov, A.A., Spicher, A., Ilyasov, A.A., Miloch, W.J., Clausen, L.B.N., Saito, Y., Jin, Y., Moen, J.I., 2018. Studies of small-scale plasma inhomogeneities in the cusp ionosphere using sounding rocket data. Phys. Plasmas 25 (4), 042902. https://doi.org/10.1063/1.5026281.

Chisham, G., Lester, M., Milan, S.E., Freeman, M.P., Bristow, W.A., Grocott, A., McWilliams, K.A., Ruohoniemi, J.M., Yeoman, T.K., Dyson, P.L., Greenwald, R.A., Kikuchi, T., Pinnock, M., Rash, J.P.S., Sato, N., Sofko, G.J., Villain, J.-P., Walker, A.D.M., 2007. A decade of the Super Dual Auroral Radar Network (SuperDARN): scientific achievements, new techniques and future directions. Surv. Geophys. 28 (1), 33–109. https://doi.org/10.1007/s10712-007-9017-8.

Clausen, L.B.N., Baker, J.B.H., Ruohoniemi, J.M., Milan, S.E., Coxon, J.C., Wing, S., Ohtani, S., Anderson, B.J., 2013. Temporal and spatial dynamics of the regions 1 and 2 Birkeland currents during substorms. J. Geophys. Res. Space Phys. 118 (6), 3007–3016. https://doi.org/10.1002/jgra.50288.

Clausen, L.B.N., Moen, J.I., Hosokawa, K., Holmes, J.M., 2016. GPS scintillations in the high latitudes during periods of dayside and nightside reconnection. J. Geophys. Res. Space Phys. 121 (4), 3293–3309. https://doi.org/10.1002/2015JA022199.

Costa, E., Kelley, M.C., 1977. Ionospheric scintillation calculations based on in situ irregularity spectra. Radio Sci. 12, 797–809. https://doi.org/10.1029/RS012i005p00797.

Costa, E., Fougere, P.F., Basu, S., 1988. Cross-correlation analysis and interpretation of spaced-receiver measurements. Radio Sci. 23 (2), 141–162. https://doi.org/10.1029/RS023i002p00141.

Coster, A.J., Colerico, M.J., Foster, J.C., Rideout, W., Rich, F., 2007. Longitude sector comparisons of storm enhanced density. Geophys. Res. Lett. 34 (18), L18105. https://doi.org/10.1029/2007GL030682.

Cowley, S.W.H., Lockwood, M., 1992. Excitation and decay of solar wind-driven flows in the magnetosphere-ionosphere system. Ann. Geophys., 103–114.

Crowley, G., 1996. Critical review of ionospheric patches and blobs. In: Stone, W.R. (Ed.), The Review of Radio Science 1992–1996. Oxford Univ. Press, New York, pp. 619–648.

Crowley, G., 1996. Critical review of ionospheric patches and blobs. In: Stone, W.R. (Ed.), The Review of Radio Science 1992-1996. Oxford Univ. Press, New York, pp. 619–648. chap. 27.

Dahlgren, H., Perry, G.W., Semeter, J.L., St.-Maurice, J.-P., Hosokawa, K., Nicolls, M.J., Greffen, M., Shiokawa, K., Heinselman, C., 2012. Space-time variability of polar cap patches: direct evidence for internal plasma structuring. J. Geophys. Res. Space Phys. 117 (A9), A09312. https://doi.org/10.1029/2012JA017961.

Dang, T., Lei, J., Wang, W., Wang, B., Zhang, B., Liu, J., Burns, A., Nishimura, Y., 2019. Formation of double tongues of ionization during the 17 March 2013 geomagnetic storm. J. Geophys. Res. Space Phys. 124 (12), 10619–10630. https://doi.org/10.1029/2019JA027268.

Datta-Barua, S., Su, Y., Deshpande, K., Miladinovich, D., Bust, G.S., Hampton, D., Crowley, G., 2015. First light from a kilometer-baseline scintillation auroral GPS array. Geophys. Res. Lett. 42 (10), 3639–3646. https://doi.org/10.1002/2015GL063556.

David, M., Sojka, J.J., Schunk, R.W., Coster, A.J., 2019. Hemispherical shifted symmetry in polar cap patch occurrence: a survey of GPS TEC maps from 2015–2018. Geophys. Res. Lett., 726–734. https://doi.org/10.1029/2019gl083952.

de la Beaujardière, O., Wickwar, V.B., Caudal, G., Holt, J.M., Craven, J.D., Frank, L.A., Brace, L.H., Evans, D.S., Winningham, J.D., Heelis, R.A., 1986. Correction to "Universal time dependence of nighttime F region densities at high latitudes". J. Geophys. Res. Space Phys. 91 (A1), 381. https://doi.org/10.1029/ja091ia01p00381.

de Wit, T.D., Krasnosel'skikh, V.V., Dunlop, M., Lühr, H., 1999. Identifying nonlinear wave interactions in plasmas using two-point measurements: a case study of short large amplitude magnetic structures (SLAMS). J. Geophys. Res. Space Phys. 104 (A8), 17079–17090. https://doi.org/10.1029/1999JA900134.

Deng, Y., Ridley, A.J., 2006. Role of vertical ion convection in the high-latitude ionospheric plasma distribution. J. Geophys. Res. Atmos. 111 (A9), A09314. https://doi.org/10.1029/2006JA011637.

Deshpande, K.B., Zettergren, M.D., 2019. Satellite-beacon ionospheric-scintillation global model of the upper atmosphere (SIGMA) III: scintillation simulation using a physics-based plasma model. Geophys. Res. Lett. 46 (9), 4564–4572.

Deshpande, K.B., Bust, G.S., Clauer, C.R., Rino, C.L., Carrano, C.S., 2014. Satellite-beacon ionospheric-scintillation global model of the upper atmosphere (SIGMA) I: high latitude sensitivity study of the model parameters. J. Geophys. Res. Space Phys. 119, 4026–4043. https://doi.org/10.1002/2013JA019699.

Deshpande, K.B., Bust, G.S., Clauer, C.R., Scales, W.A., Frissell, N.A., Ruohoniemi, J.M., Spogli, L., Mitchell, C., Weatherwax, A.T., 2016. Satellite-beacon ionospheric-scintillation global model of the upper atmosphere (SIGMA) II: inverse modeling with high-latitude observations to deduce irregularity physics. J. Geophys. Res. Space Phys. 121 (9). https://doi.org/10.1002/2016JA022943.

Doe, R.A., Mendillo, M., Vickrey, J.F., Zanetti, L.J., Eastes, R.W., 1993. Observations of nightside auroral cavities. J. Geophys. Res. Space Phys. 98 (A1), 293–310. https://doi.org/10.1029/92JA02004.

Dungey, J.W., 1961. Interplanetary magnetic field and the auroral zones. Phys. Rev. Lett. 6 (2), 47.

Dungey, J.W., 1963. The structure of the exosphere or adventures in velocity space. In: deWitt, C., Hieblot, J., Lebeau, L. (Eds.), Geophysics: the earth's environment. Gordon and Breach, p. 503.

Dyson, P.L., McClure, J.P., Hanson, W.B., 1974. In situ measurements of the spectral characteristics of F region ionospheric irregularities. J. Geophys. Res. Space Phys. 79 (10), 1497–1502. https://doi.org/10.1029/JA079i010p01497.

Earle, G.D., Kelley, M.C., 1993. Spectral evidence for stirring scales and two-dimensional turbulence in the auroral ionosphere. J. Geophys. Res. Space Phys. 98 (A7), 11543–11548. https://doi.org/10.1029/93JA00632.

Erickson, P.J., Beroz, F., Miskin, M.Z., 2011. Statistical characterization of the American sector subauroral polarization stream using incoherent scatter radar. J. Geophys. Res. Space Phys. 116, A00J21. https://doi.org/10.1029/2010JA015738.

Fæhn Follestad, A., Herlingshaw, K., Ghadjari, H., Knudsen, D.J., McWilliams, K.A., Moen, J.I., Spicher, A., Wu, J., Oksavik, K., 2020. Dayside field-aligned current impacts on ionospheric irregularities. Geophys. Res. Lett. 47 (11). https://doi.org/10.1029/2019GL086722. e2019GL086722.

Farley Jr, D.T., 1959. A theory of electrostatic fields in a horizontally stratified ionosphere subject to a vertical magnetic field. J. Geophys. Res. Space Phys. 64 (9), 1225–1233. https://doi.org/10.1029/JZ064i009p01225.

Fejer, B.G., Kelley, M.C., 1980. Ionospheric irregularities. Rev. Geophys. 18 (2), 401–454. https://doi.org/10.1029/RG018i002p00401.

Fejer, B.G., Spiro, R.W., Wolf, R.A., Foster, J.C., 1990. Latitudinal variation of perturbation electric fields during magnetically disturbed periods-1986 sundial observations and model results. Ann. Geophys. 8, 441–454.

Folk, M., Heber, G., Koziol, Q., Pourmal, E., Robinson, D., 2011. An overview of the HDF5 technology suite and its applications. In: AD '11. Proceedings of the EDBT/ICDT 2011 Workshop on Array Databases, Association for Computing Machinery, New York, NY, USA, pp. 36–47, https://doi.org/10.1145/1966895.1966900.

Forte, B., Coleman, C., Skone, S., Häggström, I., Mitchell, C., Da Dalt, F., Panicciari, T., Kinrade, J., Bust, G., 2017. Identification of scintillation signatures on GPS signals originating from plasma structures detected with EISCAT incoherent scatter radar along the same line of sight. J. Geophys. Res. Space Phys. 122 (1), 916–931. https://doi.org/10.1002/2016JA023271.

Foster, J.C., 1993. Storm time plasma transport at middle and high latitudes. J. Geophys. Res. Space Phys. 98 (A2), 1675–1690. https://doi.org/10.1029/92JA02032.

Foster, J.C., Rideout, W., 2007. Storm enhanced density: magnetic conjugacy effects. Ann. Geophys. 25 (8), 1791–1799. https://doi.org/10.5194/angeo-25-1791-2007.

Foster, J.C., Vo, H.B., 2002. Average characteristics and activity dependence of the subauroral polarization stream. J. Geophys. Res. Space Phys. 107 (A12), 1475. https://doi.org/10.1029/2002JA009409.

Foster, J.C., Coster, A.J., Erickson, P.J., Holt, J.M., Lind, F.D., Rideout, W., McCready, M., van Eyken, A., Barnes, R.J., Greenwald, R.A., Rich, F.J., 2005. Multiradar observations of the polar tongue of ionization. J. Geophys. Res. Space Phys. 110 (A9), A09S31. https://doi.org/10.1029/2004JA010928.

Fremouw, E.J., Rino, C.L., 1973. An empirical model for average F-layer scintillation at VHF/UHF. Radio Sci. 8 (3), 213–222. https://doi.org/10.1029/RS008i003p00213.

Fremouw, E.J., Leadabrand, R.L., Livingston, R.C., Cousins, M.D., Rino, C.L., Fair, B.C., Long, R.A., 1978. Early results from the DNA wideband satellite experiment–complex-signal scintillation. Radio Sci. 13 (1), 167–187. https://doi.org/10.1029/RS013i001p00167.

Fremouw, E.J., Secan, J.A., Lansinger, J.M., 1985. Spectral behavior of phase scintillation in the nighttime auroral region. Radio Sci. 20 (4), 923–933. https://doi.org/10.1029/RS020i004p00923.

Frissell, N.A., Katz, J.D., Gunning, S.W., Vega, J.S., Gerrard, A.J., Earle, G.D., Moses, M.L., West, M.L., Huba, J.D., Erickson, P.J., Miller, E.S., Gerzoff, R.B., Liles, W., Silver, H.W., 2018. Modeling amateur radio soundings of the ionospheric response to the 2017 great American eclipse. Geophys. Res. Lett. 45 (10), 4665–4674. https://doi.org/10.1029/2018GL077324.

Fuller-Rowell, T.J., Codrescu, M.V., Moffett, R.J., Quegan, S., 1994. Response of the thermosphere and ionosphere to geomagnetic storms. J. Geophys. Res. Space Phys. 99 (A3), 3893–3914.

Fuller-Rowell, T.J., Millward, G.H., Richmond, A.D., Codrescu, M.V., 2002. Storm-time changes in the upper atmosphere at low latitudes. J. Atmos. Sol. Terr. Phys. 64 (12–14), 1383–1391.

Galperin, Y.I., Zosimova, A.G., 1974. Plasma convection in polar ionosphere. Ann. Geophys. 30 (1), 1–7.

Ganguli, G., Keskinen, M.J., Romero, H., Heelis, R., Moore, T., Pollock, C., 1994. Coupling of micro- processes and macroprocesses due to velocity shear: an application to the low-altitude ionosphere. J. Geophys. Res. Space Phys. 99 (A5), 8873–8889.

Gardner, L.C., Schunk, R.W., Scherliess, L., Eccles, V., Basu, S., Valladeres, C., 2018. Modeling the mid-latitude ionosphere storm-enhanced density distribution with a data assimilation model. Space Weather 16 (10), 1539–1548. https://doi.org/10.1029/2018SW001882.

Gillies, R.G., Hussey, G.C., Sofko, G.J., McWilliams, K.A., 2012. A statistical analysis of SuperDARN scattering volume electron densities and velocity corrections using a radar frequency shifting technique. J. Geophys. Res. Space Phys. 117 (A8), A08320. https://doi.org/10.1029/2012JA017866.

Gillies, R.G., van Eyken, A., Spanswick, E., Nicolls, M., Kelly, J., Greffen, M., Knudsen, D., Connors, M., Schutzer, M., Valentic, T., Malone, M., Buonocore, J., St.-Maurice, J.P., Donovan, E., 2016. First observations from the RISR-C incoherent scatter radar. Radio Sci. 51 (10), 1645–1659. https://doi.org/10.1002/2016RS006062.

Gondarenko, N.A., Guzdar, P.N., 1999. Gradient drift instability in high latitude plasma patches: ion inertial effects. Geophys. Res. Lett. 26 (22), 3345–3348.

Gondarenko, N.A., Guzdar, P.N., 2004a. Density and electric field fluctuations associated with the gradient drift instability in the high-latitude ionosphere. Geophys. Res. Lett. 31 (11), L11802.

Gondarenko, N.A., Guzdar, P.N., 2004b. Plasma patch structuring by the nonlinear evolution of the gradient drift instability in the high-latitude ionosphere. J. Geophys. Res. Space Phys. 109 (A9), A09301.

Gondarenko, N.A., Guzdar, P.N., 2006. Nonlinear three-dimensional simulations of mesoscale structuring by multiple drives in high-latitude plasma patches. J. Geophys. Res. Space Phys. 111 (A8), A08302.

Gondarenko, N.A., Guzdar, P.N., Sojka, J.J., David, M., 2003. Structuring of high latitude plasma patches with variable drive. Geophys. Res. Lett. 30 (4).

Goodwin, L., St.-Maurice, J.P., Richards, P., Nicolls, M., Hairston, M., 2014. F region dusk ion temperature spikes at the equatorward edge of the high-latitude convection pattern. Geophys. Res. Lett. 41 (2), 300–307. https://doi.org/10.1002/2013GL058442.

Goodwin, L.V., Iserhienrhien, B., Miles, D.M., Patra, S., van der Meeren, C., Buchert, S.C., Burchill, J., Clausen, L.B.N., Knudsen, D.J., McWilliams, K.A., Moen, J., 2015. Swarm in situ observations of F region polar cap patches created by cusp precipitation. Geophys. Res. Lett. 42 (4), 996–1003. https://doi.org/10.1002/2014GL062610.

Goodwin, L.V., Nishimura, Y., Zou, Y., Shiokawa, K., Jayachandran, P.T., 2019. Mesoscale convection structures associated with airglow patches characterized using cluster-imager conjunctions. J. Geophys. Res. Space Phys. 124 (9), 7513–7532. https://doi.org/10.1029/2019ja026611.

Goodwin, L.V., Nishimura, Y., Coster, A.J., Zhang, S., Nishitani, N., Ruohoniemi, J.M., Anderson, B.J., Zhang, Q.-H., 2020. Dayside polar cap density enhancements formed during substorms. J. Geophys. Res. Space Phys. 125. https://doi.org/10.1029/2020JA028101. e2020JA028101.

Greenwald, R.A., Baker, K.B., Dudeney, J.R., Pinnock, M., Jones, T.B., Thomas, E.C., Villain, J.-P., Cerisier, J.-C., Senior, C., Hanuise, C., et al., 1995. DARN/SuperDARN. Space Sci. Rev. 71 (1–4), 761–796. https://doi.org/10.1007/BF00751350.

Gropp, W., Thakur, R., Lusk, E., 1999. Using MPI-2: Advanced Features of the Message Passing Interface, second ed. MIT Press, Cambridge, MA.

Guzdar, P.N., Gondarenko, N.A., Chaturvedi, P.K., Basu, S., 1998. Three-dimensional nonlinear simulations of the gradient drift instability in the high-latitude ionosphere. Radio Sci. 33 (6), 1901–1913.

Hasegawa, A., 1975. Macroinstabilities—Instabilities Due to Coordinate Space Nonequilibrium. Springer Berlin Heidelberg, Berlin, Heidelberg, pp. 110–144, https://doi.org/10.1007/978-3-642-65980-5_3.
He, M., Liu, L., Wan, W., Zhao, B., 2011. A study on the nighttime midlatitude ionospheric trough. J. Geophys. Res. Space Phys. 116 (A5), A05315. https://doi.org/10.1029/2010JA016252.
He, F., Zhang, X., Chen, B., 2014. Solar cycle, seasonal, and diurnal variations of subauroral ion drifts: statistical results. J. Geophys. Res. Space Phys. 119 (6), 5076–5086. https://doi.org/10.1002/2014JA019807.
Heelis, R.A., Sojka, J.J., David, M., Schunk, R.W., 2009. Storm time density enhancements in the middle-latitude dayside ionosphere. J. Geophys. Res. Space Phys. 114 (A3), A03315. https://doi.org/10.1029/2008JA013690.
Heppner, J.P., Liebrecht, M.C., Maynard, N.C., Pfaff, R.F., 1993. High-latitude distributions of plasma waves and spatial irregularities from DE 2 alternating current electric field observations. J. Geophys. Res. Space Phys. 98 (A2), 1629–1652. https://doi.org/10.1029/92JA01836.
Hill, G.E., 1963. Sudden enhancements of F-layer ionization in polar regions. J. Atmos. Sci. 20 (6), 492–497. https://doi.org/10.1175/1520-0469(1963)020¡0492:SEOLII¿2.0.CO;2.
Hirsch, M., 2020. gemini3d/pygemini., https://doi.org/10.5281/zenodo.3910039.
Hirsch, M., Zettergren, M.D., 2020. gemini3d/mat_gemini., https://doi.org/10.5281/zenodo.3987705.
Holt, J.M., Rhoda, D.A., Tetenbaum, D., van Eyken, A.P., 1992. Optimal analysis of incoherent scatter radar data. Radio Sci. 27 (3), 435–447. https://doi.org/10.1029/91RS02922.
Horvath, I., Essex, E.A., 2003. The southern-hemisphere mid-latitude day-time and night-time trough at low-sunspot numbers. J. Atmos. Sol. Terr. Phys. 65 (8), 917–940. https://doi.org/10.1016/S1364-6826(03)00113-5.
Horvath, I., Lovell, B.C., 2011. Storm-enhanced plasma density (SED) features, auroral and polar plasma enhancements, and rising topside bubbles of the 31 March 2001 superstorm. J. Geophys. Res. Space Phys. 116 (A4), A04307. https://doi.org/10.1029/2010JA015514.
Hosokawa, K., Shiokawa, K., Otsuka, Y., Nakajima, A., Ogawa, T., Kelly, J.D., 2006. Estimating drift velocity of polar cap patches with All-Sky Airglow Imager at Resolute Bay, Canada. Geophys. Res. Lett. 33 (15), L15111. https://doi.org/10.1029/2006GL026916.
Hosokawa, K., Shiokawa, K., Otsuka, Y., Ogawa, T., St.-Maurice, J.-P., Sofko, G.J., Andre, D.A., 2009a. Relationship between polar cap patches and field-aligned irregularities as observed with an All-Sky Airglow Imager at Resolute Bay and the PolarDARN radar at Rankin Inlet. J. Geophys. Res. Space Phys. 114 (A3), A03306. https://doi.org/10.1029/2008JA013707.
Hosokawa, K., Tsugawa, T., Shiokawa, K., Otsuka, Y., Ogawa, T., Hairston, M.R., 2009b. Unusually elongated, bright airglow plume in the polar cap F region: is it a tongue of ionization? Geophys. Res. Lett. 36 (7), L07103. https://doi.org/10.1029/2009GL037512.
Hosokawa, K., Tsugawa, T., Shiokawa, K., Otsuka, Y., Nishitani, N., Ogawa, T., Hairston, M.R., 2010. Dynamic temporal evolution of polar cap tongue of ionization during magnetic storm. J. Geophys. Res. Space Phys. 115 (A12), A12333.
Hosokawa, K., Taguchi, S., Ogawa, Y., Sakai, J., 2013. Two-dimensional direct imaging of structuring of polar cap patches. J. Geophys. Res. Space Phys. 118, 6536–6543. https://doi.org/10.1002/jgra.50577.
Hosokawa, K., Taguchi, S., Ogawa, Y., 2016. Edge of polar cap patches. J. Geophys. Res. Space Phys. 121, 3410–3420. https://doi.org/10.1002/2015JA021960.
Huang, C., Sazykin, S., Spiro, R., Goldstein, J., Crowley, G., Ruohoniemi, J.M., 2006. Storm-time penetration electric fields and their effects. Eos Trans. AGU 87 (13), 131. 131.
Huba, J.D., Mitchell, H.G., Keskinen, M.J., Fedder, J.A., Satyanarayana, P., Zalesak, S.T., 1988. Simulations of plasma structure evolution in the high-latitude ionosphere. Radio Sci. 23 (4), 503–512.
Huba, J.D., Joyce, G., Fedder, J.A., 2000. Sami2 is another model of the ionosphere (SAMI2): a new low-latitude ionosphere model. J. Geophys. Res. Space Phys. 105 (A10), 23035–23053. https://doi.org/10.1029/2000JA000035.
Huba, J.D., Joyce, G., Krall, J., 2008. Three-dimensional equatorial spread F modeling. Geophys. Res. Lett. 35 (10). https://doi.org/10.1029/2008GL033509.
Huba, J.D., Sazykin, S., Coster, A., 2017. SAMI3-RCM simulation of the 17 March 2015 geomagnetic storm. J. Geophys. Res. Space Phys. 122 (1), 1246–1257. https://doi.org/10.1002/2016JA023341.

Hysell, D.L., Rodrigues, F.S., Chau, J.L., Huba, J.D., 2008. Full profile incoherent scatter analysis at Jicamarca. Ann. Geophys. 26, 59–75. https://doi.org/10.5194/angeo-26-59-2008.

Hysell, D.L., Milla, M.A., Rodrigues, F.S., Varney, R.H., Huba, J.D., 2015. Topside equatorial ionospheric density, temperature, and composition under equinox, low solar flux conditions. J. Geophys. Res. Space Phys. 120, 3899–3912. https://doi.org/10.1002/2015JA021168.

Ishida, T., Ogawa, Y., Kadokura, A., Hiraki, Y., Häggström, I., 2014. Seasonal variation and solar activity dependence of the quiet-time ionospheric trough. J. Geophys. Res. Space Phys. 119, 6774–6783. https://doi.org/10.1002/2014JA019996.

Ivarsen, M.F., Jin, Y., Spicher, A., Clausen, L.B.N., 2019. Direct evidence for the dissipation of small-scale ionospheric plasma structures by a conductive E region. J. Geophys. Res. Space Phys. 124 (4), 2935–2942. https://doi.org/10.1029/2019JA026500.

Jackson, J.D., 2007. Classical Electrodynamics. John Wiley & Sons.

Jaggi, R.K., Wolf, R.A., 1973. Self-consistent calculation of the motion of a sheet of ions in the magnetosphere. J. Geophys. Res. Space Phys. 78 (16), 2852–2866.

Jayachandran, P.T., Hamza, A.M., Hosokawa, K., Mezaoui, H., Shiokawa, K., 2017. GPS amplitude and phase scintillation associated with polar cap auroral forms. J. Atmos. Sol. Terr. Phys. 164, 185–191. https://doi.org/10.1016/j.jastp.2017.08.030.

Jin, Y., Moen, J.I., Miloch, W.J., 2014. GPS scintillation effects associated with polar cap patches and substorm auroral activity: direct comparison. J. Space Weather Space Clim. 4, A23. https://doi.org/10.1051/swsc/2014019.

Jin, Y., Moen, J.I., Miloch, W.J., 2015. On the collocation of the cusp aurora and the GPS phase scintillation: a statistical study. J. Geophys. Res. Space Phys. 120 (10), 9176–9191. https://doi.org/10.1002/2015JA021449.

Jin, Y., Moen, J.I., Miloch, W.J., Clausen, L.B.N., Oksavik, K., 2016. Statistical study of the GNSS phase scintillation associated with two types of auroral blobs. J. Geophys. Res. Space Phys. 121 (5), 4679–4697. https://doi.org/10.1002/2016JA022613.

Jin, Y., Moen, J.I., Oksavik, K., Spicher, A., Clausen, L.B.N., Miloch, W.J., 2017. GPS scintillations associated with cusp dynamics and polar cap patches. J. Space Weather Space Clim. 7, A23. https://doi.org/10.1051/swsc/2017022.

Jin, Y., Miloch, W.J., Moen, J.I., Clausen, L.B.N., 2018. Solar cycle and seasonal variations of the GPS phase scintillation at high latitudes. J. Space Weather Space Clim. 8, A48. https://doi.org/10.1051/swsc/2018034.

Jin, Y., Moen, J.I., Spicher, A., Oksavik, K., Miloch, W.J., Clausen, L.B.N., PoŻoga, M., Saito, Y., 2019. Simultaneous rocket and scintillation observations of plasma irregularities associated with a reversed flow event in the cusp ionosphere. J. Geophys. Res. Space Phys. 124 (8), 7098–7111. https://doi.org/10.1029/2019JA026942.

Karlsson, T., Andersson, L., Gillies, D.M., Lynch, K., Marghitu, O., Partamies, N., Sivadas, N., Wu, J., 2020. Quiet, discrete auroral arcs–observations. Space Sci. Rev. 216 (1), 16. https://doi.org/10.1007/s11214-020-0641-7.

Karpachev, A.T., 2003. The dependence of the main ionospheric trough shape on longitude, altitude, season, local time, and solar and magnetic activity. Geomagn. Aeron. 43 (2), 239–251.

Karpachev, A.T., Klimenko, M.V., Klimenko, V.V., 2019. Longitudinal variations of the ionospheric trough position. Adv. Space Res. 63 (2), 950–966. https://doi.org/10.1016/j.asr.2018.09.038.

Kelley, M.C., 2009. The Earth's Ionosphere: Plasma Physics and Electrodynamics. Elsevier Science.

Kelley, M.C., Carlson, C.W., 1977. Observations of intense velocity shear and associated electrostatic waves near an auroral arc. J. Geophys. Res. Space Phys. 82 (16), 2343–2348. https://doi.org/10.1029/JA082i016p02343.

Kelley, M.C., Fejer, B.G., Gonzales, C.A., 1979. An explanation for anomalous equatorial ionospheric electric fields associated with a northward turning of the interplanetary magnetic field. Geophys. Res. Lett. 6 (4), 301–304.

Kelley, M.C., Baker, K.D., Ulwick, J.C., Rino, C.L., Baron, M.J., 1980. Simultaneous rocket probe, scintillation, and incoherent scatter radar observations of irregularities in the auroral zone ionosphere. Radio Sci. 15 (3), 491–505. https://doi.org/10.1029/RS015i003p00491.

Kelley, M.C., Vickrey, J.F., Carlson, C., Torbert, R., 1982. On the origin and spatial extent of high-latitude F region irregularities. J. Geophys. Res. Space Phys. 87 (A6), 4469–4475. https://doi.org/10.1029/JA087iA06p04469.

Kelley, M.C., Vlasov, M.N., Foster, J.C., Coster, A.J., 2004. A quantitative explanation for the phenomenon known as storm-enhanced density. Geophys. Res. Lett. 31 (19), L19809. https://doi.org/10.1029/2004GL020875.

Kersley, L., Pryse, S.E., Wheadon, N.S., 1988. Small scale ionospheric irregularities near regions of soft particle precipitation: scintillation and EISCAT observations. J. Atmos. Terr. Phys. 50 (12), 1047–1055. https://doi.org/10.1016/0021-9169(88)90094-3.

Keskinen, M.J., 2006. GPS scintillation channel model for the disturbed low-latitude ionosphere. Radio Sci. 41 (04), 1–7.

Keskinen, M.J., Ossakow, S.L., 1981. On the spatial power spectrum of the $\mathbf{E} \times \mathbf{B}$ gradient drift instability in ionospheric plasma clouds. J. Geophys. Res. Space Phys. 86, 6947–6950. https://doi.org/10.1029/JA086iA08p06947.

Keskinen, M.J., Ossakow, S.L., 1982. Nonlinear evolution of plasma enhancements in the auroral ionosphere, 1, Long wavelength irregularities. J. Geophys. Res. Space Phys. 87 (A1), 144–150. https://doi.org/10.1029/JA087iA01p00144.

Keskinen, M.J., Ossakow, S.L., 1983. Theories of high-latitude ionospheric irregularities: a review. Radio Sci. 18 (06), 1077–1091.

Keskinen, M.J., Mitchell, H.G., Fedder, J.A., Satyanarayana, P., Zalesak, S.T., Huba, J.D., 1988. Nonlinear evolution of the Kelvin-Helmholtz instability in the high-latitude ionosphere. J. Geophys. Res. Space Phys. 93 (A1), 137–152.

Kinrade, J., Mitchell, C.N., Yin, P., Smith, N., Jarvis, M.J., Maxfield, D.J., Rose, M.C., Bust, G.S., Weatherwax, A.T., 2012. Ionospheric scintillation over Antarctica during the storm of 5–6 April 2010. J. Geophys. Res. Space Phys. 117 (A5). https://doi.org/10.1029/2011JA017073.

Kinrade, J., Mitchell, C.N., Smith, N.D., Ebihara, Y., Weatherwax, A.T., Bust, G.S., 2013. GPS phase scintillation associated with optical auroral emissions: first statistical results from the geographic south pole. J. Geophys. Res. Space Phys. 118 (5), 2490–2502. https://doi.org/10.1002/jgra.50214.

Kintner, P.M., Seyler, C.E., 1985. The status of observations and theory of high latitude ionospheric and magnetospheric plasma turbulence. Space Sci. Rev. 41 (1-2), 91–129.

Kivanç, Ö., Heelis, R.A., 1997. Structures in ionospheric number density and velocity associated with polar cap ionization patches. J. Geophys. Res. Space Phys. 102 (A1), 307–318. https://doi.org/10.1029/96JA03141.

Kivanc, O., Heelis, R.A., 1997. Structures in ionospheric number density and velocity associated with polar cap ionization patches. J. Geophys. Res. Space Phys. 102 (A1), 307–318. https://doi.org/10.1029/96JA03141.

Kivanç, Ö., Heelis, R.A., 1998. Spatial distribution of ionospheric plasma and field structures in the high-latitude F region. J. Geophys. Res. Space Phys. 103 (A4), 6955–6968. https://doi.org/10.1029/97JA03237.

Knepp, D.L., 1983. Multiple phase-screen calculation of the temporal behavior of stochastic waves. IEEE Proc. 71, 722–737.

Knudsen, W.C., 1974. Magnetospheric convection and the high-latitude F_2 ionosphere. J. Geophys. Res. Space Phys. 79 (7), 1046–1055. https://doi.org/10.1029/JA079i007p01046.

Koustov, A., Hosokawa, K., Nishitani, N., Ogawa, T., Shiokawa, K., 2008. Rankin Inlet PolarDARN radar observations of duskward moving sun-aligned optical forms. Ann. Geophys. 26 (9), 2711–2723. https://doi.org/10.5194/angeo-26-2711-2008.

Kunduri, B.S.R., Baker, J.B.H., Ruohoniemi, J.M., Thomas, E.G., Shepherd, S.G., Sterne, K.T., 2017. Statistical characterization of the large-scale structure of the subauroral polarization stream. J. Geophys. Res. Space Phys. 122 (6), 6035–6048. https://doi.org/10.1002/2017JA024131.

Labelle, J., Sica, R.J., Kletzing, C., Earle, G.D., Kelley, M.C., Lummerzheim, D., Torbert, R.B., Baker, K. D., Berg, G., 1989. Ionization from soft electron precipitation in the auroral F region. J. Geophys. Res. Space Phys. 94 (A4), 3791–3798. https://doi.org/10.1029/JA094iA04p03791.

Lagoutte, D., Cerisier, J.C., Plagnaud, J.L., Villain, J.P., Forget, B., 1992. High-latitude ionospheric electrostatic turbulence studied by means of the wavelet transform. J. Atmos. Terr. Phys. 54 (10), 1283–1293. https://doi.org/10.1016/0021-9169(92)90037-L.

Lamarche, L.J., Makarevich, R.A., 2017. Radar observations of density gradients, electric fields, and plasma irregularities near polar cap patches in the context of the gradient-drift instability. J. Geophys. Res. Space Phys. 122, 3721–3736. https://doi.org/10.1002/2016JA023702.

Lamarche, L., Deshpande, Bharat, K., Zettergren, M.D., Varney, R., 2020. Satellite-beacon ionospheric-scintillation global model of the upper atmosphere (SIGMA) III: Scintillation simulation using a physics-based plasma model. J. Geophys. Res. 46 (9), 4564–4572.

Lee, I.T., Wang, W., Liu, J.Y., Chen, C.Y., Lin, C.H., 2011. The ionospheric midlatitude trough observed by FORMOSAT-3/COSMIC during solar minimum. J. Geophys. Res. Space Phys. 116 (A6), A06311. https://doi.org/10.1029/2010JA015544.

Liang, J., Donovan, E., Reimer, A., Hampton, D., Zou, S., Varney, R., 2018. Ionospheric electron heating associated with pulsating auroras: joint optical and PFISR observations. J. Geophys. Res. Space Phys. 123 (5), 4430–4456.

Liu, J., Wang, W., Burns, A., Solomon, S.C., Zhang, S., Zhang, Y., Huang, C., 2016. Relative importance of horizontal and vertical transports to the formation of ionospheric storm-enhanced density and polar tongue of ionization. J. Geophys. Res. Space Phys. 121 (8), 8121–8133. https://doi.org/10.1002/2016JA022882.

Lockwood, M., Carlson, H.C., 1992. Production of polar cap electron density patches by transient magnetopause reconnection. Geophys. Res. Lett. 19 (17), 1731–1734.

Lockwood, M., Carlson Jr, H.C., 1992. Production of polar cap electron density patches by transient magnetopause reconnection. Geophys. Res. Lett. 19 (17), 1731–1734. https://doi.org/10.1029/92GL01993.

Lorentzen, D.A., Shumilov, N., Moen, J., 2004. Drifting airglow patches in relation to tail reconnection. Geophys. Res. Lett. 31 (2), L02806. https://doi.org/10.1029/2003GL017785.

Lotko, W., 2004. Inductive magnetosphere-ionosphere coupling. J. Atmos. Sol. Terr. Phys. 66 (15–16), 1443–1456.

Lu, G., Goncharenko, L., Nicolls, M.J., Maute, A., Coster, A., Paxton, L.J., 2012. Ionospheric and thermospheric variations associated with prompt penetration electric fields. J. Geophys. Res. Space Phys. 117 (A8), A08312.

Lu, G., Zakharenkova, I., Cherniak, I., Dang, T., 2020. Large-scale ionospheric disturbances during the 17 March 2015 storm: a model-data comparative study. J. Geophys. Res. Space Phys., e2019JA027726.

Lyons, L.R., Nishimura, Y., Zou, Y., 2016. Unsolved problems: mesoscale polar cap flow channels' structure, propagation, and effects on space weather disturbances. J. Geophys. Res. Space Phys. 121 (4), 3347–3352. https://doi.org/10.1002/2016JA022437.

Ma, Y.Z., Zhang, Q.H., Xing, Z.Y., Heelis, R.A., Oksavik, K., Wang, Y., 2018. The ion/electron temperature characteristics of polar cap classical and hot patches and their influence on ion upflow. Geophys. Res. Lett. 45 (16), 8072–8080. https://doi.org/10.1029/2018GL079099.

MacDougall, J.W., Jayachandran, P.T., 2007. Polar patches: auroral zone precipitation effects. J. Geophys. Res. Space Phys. 112 (A5), 1–16. https://doi.org/10.1029/2006JA011930.

Makarevich, R.A., 2014. Symmetry considerations in the two-fluid theory of the gradient-drift instability in the lower ionosphere. J. Geophys. Res. Space Phys. 119. https://doi.org/10.1002/2014JA020292.

Makarevich, R.A., 2016a. Towards an integrated view of ionospheric plasma instabilities: 2. Three inertial modes of a cubic dispersion relation. J. Geophys. Res. Space Phys. 121, 6855–6869. https://doi.org/10.1002/2016JA022864.

Makarevich, R.A., 2016b. Towards an integrated view of ionospheric plasma instabilities: altitudinal transitions and strong gradient case. J. Geophys. Res. Space Phys. 121, 3634–3647. https://doi.org/10.1002/2016JA022515.

Makarevich, R.A., 2019. Toward an integrated view of ionospheric plasma instabilities: 3. Explicit growth rate and oscillation frequency for arbitrary altitude. J. Geophys. Res. Space Phys. 124 (7), 6138–6155. https://doi.org/10.1029/2019JA026584.

Makarevich, R.A., Lamarche, L.J., Nicolls, M.J., 2015. Resolute Bay incoherent scatter radar observations of plasma structures in the vicinity of polar holes. J. Geophys. Res. Space Phys. 120 (9), 7970–7986. https://doi.org/10.1002/2015JA021443.

Mallis, M., Essex, E.A., 1993. Diurnal and seasonal variability of the southern-hemisphere main ionospheric trough from differential-phase measurements. J. Atmos. Terr. Phys. 55 (7), 1021–1037. https://doi.org/10.1016/0021-9169(93)90095-G.

Mannucci, A.J., Wilson, B.D., Yuan, D.N., Ho, C.H., Lindqwister, U.J., Runge, T.F., 1998. A global mapping technique for GPS-derived ionospheric total electron content measurements. Radio Sci. 33 (3), 565–582. https://doi.org/10.1029/97RS02707.

McCrea, I., Aikio, A., Alfonsi, L., Belova, E., Buchert, S., Clilverd, M., Engler, N., Gustavsson, B., Heinselman, C., Kero, J., Kosch, M., Lamy, H., Leyser, T., Ogawa, Y., Oksavik, K., Pellinen-Wannberg, A., Pitout, F., Rapp, M., Stanislawska, I., Vierinen, J., 2015. The science case for the EISCAT_3D radar. Prog. Earth Planet. Sci. 2 (1), 21. https://doi.org/10.1186/s40645-015-0051-8.

Meek, J.H., 1949. Sporadic ionization at high latitudes. J. Geophys. Res. Space Phys. 54 (4), 339–345. https://doi.org/10.1029/JZ054i004p00339.

Mendillo, M., 2006. Storms in the ionosphere: patterns and processes for total electron content. Rev. Geophys. 44 (4), RG4001. https://doi.org/10.1029/2005RG000193.

Meziane, K., Kashcheyev, A., Patra, S., Jayachandran, P.T., Hamza, A.M., 2020. Solar cycle variations of GPS amplitude scintillation for the polar region. Space Weather 18 (8). https://doi.org/10.1029/2019SW002434. e2019SW002434.

Michael, C.M., Yeoman, T.K., Wright, D.M., Milan, S.E., James, M.K., 2020. A ray tracing simulation of HF ionospheric radar performance at African equatorial latitudes. Radio Sci. 55 (2). https://doi.org/10.1029/2019RS006936. e2019RS006936.

Milan, S.E., Yeoman, T.K., Lester, M., Thomas, E.C., Jones, T.B., 1997. Initial backscatter occurrence statistics from the CUTLASS HF radars. Ann. Geophys. 15 (6), 703–718. https://doi.org/10.1007/s00585-997-0703-0.

Milan, S.E., Lester, M., Yeoman, T.K., 2002. HF radar polar patch formation revisited: summer and winter variations in dayside plasma structuring. Ann. Geophys. 20 (4), 487–499. https://doi.org/10.5194/angeo-20-487-2002.

Millward, G.H., Moffett, R.J., Balmforth, H.F., Rodger, A.S., 1999. Modeling the ionospheric effects of ion and electron precipitation in the cusp. J. Geophys. Res. Space Phys. 104 (A11), 24603–24612. https://doi.org/10.1029/1999JA900249.

Mitchell, C.N., Alfonsi, L., De Franceschi, G., Lester, M., Romano, V., Wernik, A.W., 2005. GPS TEC and scintillation measurements from the polar ionosphere during the October 2003 storm. Geophys. Res. Lett. 32 (12). https://doi.org/10.1029/2004GL021644.

Mitchell Jr, H.G., Fedder, J.A., Keskinen, M.J., Zalesak, S.T., 1985. A simulation of high latitude F-layer instabilities in the presence of magnetosphere-ionosphere coupling. Geophys. Res. Lett. 12 (5), 283–286.

Moen, J., Walker, I.K., Kersley, L., Milan, S.E., 2002. On the generation of cusp HF backscatter irregularities. J. Geophys. Res. Space Phys. 107 (A4). https://doi.org/10.1029/2001JA000111. SIA 3-1–SIA 3-5.

Moen, J., Rinne, Y., Carlson, H.C., Oksavik, K., Fujii, R., Opgenoorth, H., 2008. On the relationship between thin Birkeland current arcs and reversed flow channels in the winter cusp/cleft ionosphere. J. Geophys. Res. Space Phys. 113 (A9), A09220. https://doi.org/10.1029/2008JA013061.

Moen, J., Oksavik, K., Abe, T., Lester, M., Saito, Y., Bekkeng, T.A., Jacobsen, K.S., 2012. First in-situ measurements of HF radar echoing targets. Geophys. Res. Lett. 39 (7), L07104. https://doi.org/10.1029/2012GL051407.

Moen, J., Oksavik, K., Alfonsi, L., Daabakk, Y., Romano, V., Spogli, L., 2013. Space weather challenges of the polar cap ionosphere. J. Space Weather Space Clim. 3, A02. https://doi.org/10.1051/swsc/2013025.

Moffett, R.J., Quegan, S., 1983. The mid-latitude trough in the electron concentration of the ionospheric F-layer—a review of observations and modelling. J. Atmos. Terr. Phys. 45, 315–343. https://doi.org/10.1016/S0021-9169(83)80038-5.

Moldwin, M.B., Zou, S., Heine, T., 2016. The story of plumes: the development of a new conceptual framework for understanding magnetosphere and ionosphere coupling. Ann. Geophys. 34 (12), 1243–1253. https://doi.org/10.5194/angeo-34-1243-2016.

Mounir, H., Berthelier, A., Cerisier, J.C., Lagoutte, D., Beghin, C., 1991. The small-scale turbulent structure of the high latitude ionosphere—Arcad-Aureol-3 observations. Ann. Geophys. 9, 725–737.
Mrak, S., Semeter, J., Hirsch, M., Starr, G., Hampton, D., Varney, R.H., Reimer, A.S., Swoboda, J., Erickson, P.J., Lind, F., Coster, A.J., Pankratius, V., 2018. Field-aligned GPS scintillation: multisensor data fusion. J. Geophys. Res. Space Phys. 123 (1), 974–992. https://doi.org/10.1002/2017JA024557.
Muldrew, D.B., 1965. F-layer ionization troughs deduced from Alouette data. J. Geophys. Res. Space Phys. 70 (11), 2635–2650. https://doi.org/10.1029/JZ070i011p02635.
Narita, Y., 2012. Multi-spacecraft Measurements. Springer Berlin Heidelberg, Berlin, Heidelberg, pp. 39–65, https://doi.org/10.1007/978-3-642-25667-7_3.
Narita, Y., Glassmeier, K.-H., Motschmann, U., 2010. Wave vector analysis methods using multi-point measurements. Nonlinear Process. Geophys. 17 (5), 383–394. https://doi.org/10.5194/npg-17-383-2010.
Nicolls, M.J., Heinselman, C.J., 2007. Three-dimensional measurements of traveling ionospheric disturbances with the poker flat incoherent scatter radar. Geophys. Res. Lett. 34 (21), L21104.
Nilsson, H., Sergienko, T.I., Ebihara, Y., Yamauchi, M., 2005. Quiet-time mid-latitude trough: influence of convection, field-aligned currents and proton precipitation. Ann. Geophys. 23 (10), 3277–3288. https://doi.org/10.5194/angeo-23-3277-2005.
Nishida, A., 1968. Coherence of geomagnetic DP2 fluctuations with interplanetary magnetic variations. J. Geophys. Res. Space Phys. 73 (5), 1795–1803.
Nishimura, Y., Lyons, L.R., 2016. Localized reconnection in the magnetotail driven by lobe flow channels: global MHD simulation. J. Geophys. Res. Space Phys. 121 (2), 1327–1338. https://doi.org/10.1002/2015JA022128.
Noja, M., Stolle, C., Park, J., Lühr, H., 2013. Long-term analysis of ionospheric polar patches based on CHAMP TEC data. Radio Sci. 48 (3), 289–301. https://doi.org/10.1002/rds.20033.
Oksavik, K., Moen, J., Carlson, H.C., 2004. High-resolution observations of the small-scale flow pattern associated with a poleward moving auroral form in the cusp. Geophys. Res. Lett. 31 (11). https://doi.org/10.1029/2004GL019838.
Oksavik, K., Moen, J., Carlson, H.C., Greenwald, R.A., Milan, S.E., Lester, M., Denig, W.F., Barnes, R.J., 2005. Multi-instrument mapping of the small-scale flow dynamics related to a cusp auroral transient. Ann. Geophys. 23 (7), 2657–2670. https://doi.org/10.5194/angeo-23-2657-2005.
Oksavik, K., Ruohoniemi, J.M., Greenwald, R.A., Baker, J.B.H., Moen, J., Carlson, H.C., Yeoman, T.K., Lester, M., 2006. Observations of isolated polar cap patches by the European Incoherent Scatter (EISCAT) Svalbard and Super Dual Auroral Radar Network (SuperDARN) Finland radars. J. Geophys. Res. Space Phys. 111 (A5). https://doi.org/10.1029/2005JA011400.
Oksavik, K., Moen, J.I., Rekaa, E.H., Carlson, H.C., Lester, M., 2011. Reversed flow events in the cusp ionosphere detected by SuperDARN HF radars. J. Geophys. Res. Space Phys. 116 (A12). https://doi.org/10.1029/2011JA016788.
Oksavik, K., Moen, J., Lester, M., Bekkeng, T.A., Bekkeng, J.K., 2012. In situ measurements of plasma irregularity growth in the cusp ionosphere. J. Geophys. Res. Space Phys. 117 (A11). https://doi.org/10.1029/2012JA017835.
Oksavik, K., van der Meeren, C., Lorentzen, D.A., Baddeley, L.J., Moen, J., 2015. Scintillation and loss of signal lock from poleward moving auroral forms in the cusp ionosphere. J. Geophys. Res. Space Phys. 120 (10), 9161–9175. https://doi.org/10.1002/2015JA021528.
Opgenoorth, H.J., Hägström, I., Williams, P.J.S., Jones, G.O.L., 1990. Regions of strongly enhanced perpendicular electric fields adjacent to auroral arcs. J. Atmos. Terr. Phys. 52 (6-8), 449–458. https://doi.org/10.1016/0021-9169(90)90044-N.
Ossakow, S.L., Chaturvedi, P.K., Workman, J.B., 1978. High-altitude limit of the gradient drift instability. J. Geophys. Res. Space Phys. 83 (A6), 2691–2693.
Paschmann, G., Daly, P.W., 1998. Analysis Methods for Multi-Spacecraft Data. ISSI Scientific Reports Series SR-001, ESA/ISSI. vol. 1. ISSI Scientific Reports Series.
Perkins, F.W., Zabusky, N.J., Doles, J.H., 1973. Deformation and striation of plasma clouds in the ionosphere, I. J. Geophys. Res. Space Phys. 78 (4), 697–709.

Perkins, F.W., Zabusky, N.J., Doles III, J.H., 1973. Deformation and striation of plasma clouds in the ionosphere: 1. J. Geophys. Res. Space Phys. 78 (4), 697–709.

Perry, G.W., St.-Maurice, J.-P., 2018. A polar-cap patch detection algorithm for the advanced modular incoherent scatter radar system. Radio Sci. 53 (10), 1225–1244. https://doi.org/10.1029/2018RS006600.

Perry, G.W., St.-Maurice, J.-P., Hosokawa, K., 2013. The interconnection between cross-polar cap convection and the luminosity of polar cap patches. J. Geophys. Res. Space Phys. 118 (11), 7306–7315. https://doi.org/10.1002/2013JA019196.

Perry, G.W., Dahlgren, H., Nicolls, M.J., Zettergren, M., St.-Maurice, J.-P., Semeter, J.L., Sundberg, T., Hosokawa, K., Shiokawa, K., Chen, S., 2015. Spatiotemporally resolved electrodynamic properties of a sun-aligned arc over Resolute Bay. J. Geophys. Res. Space Phys., 9977–9987. https://doi.org/10.1002/2015JA021790.

Phelps, A.D.R., Sagalyn, R.C., 1976. Plasma density irregularities in the high-latitude top side ionosphere. J. Geophys. Res. Space Phys. 81 (4), 515–523. https://doi.org/10.1029/JA081i004p00515.

Pierrard, V., Voiculescu, M., 2011. The 3D model of the plasmasphere coupled to the ionosphere. Geophys. Res. Lett. 38 (12), L12104. https://doi.org/10.1029/2011GL047767.

Press, W., Flannery, B., Teukolsky, S., Vetterling, W., 1992. Numerical Recipes in C: The Art of Scientific Computing. Cambridge University Press.

Prikryl, P., Jayachandran, P.T., Mushini, S.C., Pokhotelov, D., MacDougall, J.W., Donovan, E., Spanswick, E., St.-Maurice, J.-P., 2010. GPS TEC, scintillation and cycle slips observed at high latitudes during solar minimum. Ann. Geophys. 28 (6), 1307–1316. https://doi.org/10.5194/angeo-28-1307-2010.

Prikryl, P., Jayachandran, P.T., Mushini, S.C., Chadwick, R., 2011. Climatology of GPS phase scintillation and HF radar backscatter for the high-latitude ionosphere under solar minimum conditions. Ann. Geophys. 29 (2), 377–392. https://doi.org/10.5194/angeo-29-377-2011.

Prikryl, P., Jayachandran, P.T., Chadwick, R., Kelly, T.D., 2015. Climatology of GPS phase scintillation at northern high latitudes for the period from 2008 to 2013. Ann. Geophys. 33 (5), 531–545. https://doi.org/10.5194/angeo-33-531-2015.

Priyadarshi, S., 2015. A review of ionospheric scintillation models. Surv. Geophys. 36 (2), 295–324. https://doi.org/10.1007/s10712-015-9319-1.

Prölss, G.W., 2007. The equatorward wall of the subauroral trough in the afternoon/evening sector. Ann. Geophys. 25 (3), 645–659. https://doi.org/10.5194/angeo-25-645-2007.

Prölss, G.W., 1995. Ionospheric F-region storms. In: Handbook of Atmospheric Electrodynamics, vol. 2. CRC Press, Boca Raton, FL.

Pryse, S.E., Kersley, L., Williams, M.J., Walker, I.K., 1998. The spatial structure of the dayside ionospheric trough. Ann. Geophys. 16 (10), 1169–1179. https://doi.org/10.1007/s00585-998-1169-4.

Ratcliffe, J.A., 1956. Some aspects of diffraction theory and their application to the ionosphere. Rep. Prog. Phys. 19 (1), 188–267. https://doi.org/10.1088/0034-4885/19/1/306.

Ravindran Varrier, N., 2010. Ray Tracing Analysis for the Mid-latitude SuperDARN HF Radar at Blackstone Incorporating the IRI-2007 Model (Master's thesis). Virginia Polytechnic Institute and State University.

Ren, J., Zou, S., Gillies, R.G., Donovan, E., Varney, R.H., 2018. Statistical characteristics of polar cap patches observed by RISR-C. J. Geophys. Res. Space Phys. 123, 6981–6995. https://doi.org/10.1029/2018JA025621.

Ren, J., Zou, S., Kendall, E., Coster, A., Sterne, K., Ruohoniemi, M., 2020. Direct observations of a polar cap patch formation associated with dayside reconnection driven fast flow. J. Geophys. Res. Space Phys. 125 (4). e2019JA027745.

Retterer, J.M., 2010. Forecasting low-latitude radio scintillation with 3-D ionospheric plume models: 2. Scintillation calculation. J. Geophys. Res. Space Phys. 115 (A3). https://doi.org/10.1029/2008JA013840.

Rinne, Y., Moen, J., Oksavik, K., Carlson, H.C., 2007. Reversed flow events in the winter cusp ionosphere observed by the European incoherent scatter (EISCAT) Svalbard radar. J. Geophys. Res. Space Phys. 112 (A10). https://doi.org/10.1029/2007JA012366.

Rino, C.L., 1979a. A power law phase screen model for ionospheric scintillation. I—Weak scatter. Radio Sci. 14, 1135–1145. https://doi.org/10.1029/RS014i006p01135.
Rino, C.L., 1979b. A power law phase screen model for ionospheric scintillation. II—Strong scatter. Radio Sci. 14, 1147–1155. https://doi.org/10.1029/RS014i006p01135.
Rino, C.L., 2010. The Theory of Scintillation with Applications in Remote Sensing. John Wiley & Sons.
Rino, C.L., Carrano, C.S., 2011. The application of numerical simulations in Beacon scintillation analysis and modeling. Radio Sci. 46 (3), RS0D02. https://doi.org/10.1029/2010RS004563.
Rino, C.L., Livingston, R.C., 1982. On the analysis and interpretation of spaced-receiver measurements of transionospheric radio waves. Radio Sci. 17 (4), 845–854. https://doi.org/10.1029/RS017i004p00845.
Rino, C., Breitsch, B., Morton, Y., Jiao, Y., Xu, D., Carrano, C., 2018a. A compact multi-frequency GNSS scintillation model. Navigation 65 (4), 563–569. https://doi.org/10.1002/navi.263.
Rino, C., Carrano, C., Groves, K., Yokoyama, T., 2018b. A configuration space model for intermediate-scale ionospheric structure. Radio Sci. 53 (12), 1472–1480. https://doi.org/10.1029/2018RS006678.
Rino, C., Carrano, C., Groves, K., 2019. Wave field propagation in extended highly anisotropic media. Radio Sci. 54 (7), 646–659. https://doi.org/10.1029/2019RS006793.
Rishbeth, H., Hanson, W.B., 1974. A comment on plasma 'pile-up' in the F-region. J. Atmos. Terr. Phys. 36 (4), 703–706. https://doi.org/10.1016/0021-9169(74)90094-4.
Robinson, R.M., Vondrak, R.R., Friis-Christensen, E., 1987. Ionospheric currents associated with a sun-aligned arc connected to the auroral oval. Geophys. Res. Lett. 14 (6), 656–659. https://doi.org/10.1029/GL014i006p00656.
Rodger, A.S., 2008. The Mid-Latitude Trough—Revisited, Geophysical Monograph Series, vol. 181. In: American Geophysical Union. Washington, DC, pp. 25–33.
Rodger, A.S., Brace, L.H., Hoegy, W.R., Winningham, J.D., 1986. The poleward edge of the mid-latitude trough—its formation, orientation and dynamics. J. Atmos. Terr. Phys. 48, 715–728. https://doi.org/10.1016/0021-9169(86)90021-8.
Rodger, A.S., Moffett, R.J., Quegan, S., 1992. The role of ion drift in the formation of ionisation troughs in the mid- and high-latitude ionosphere—a review. J. Atmos. Terr. Phys. 54, 1–30. https://doi.org/10.1016/0021-9169(92)90082-V.
Rodger, A.S., Pinnock, M., Dudeney, J.R., Baker, K.B., Greenwald, R.A., 1994. A new mechanism for polar patch formation. J. Geophys. Res. Space Phys. 99 (A4), 6425–6436. https://doi.org/10.1029/93JA01501.
Ruohoniemi, J.M., Baker, K.B., 1998. Large-scale imaging of high-latitude convection with super dual auroral radar network HF radar observations. J. Geophys. Res. Space Phys. 103 (A9), 20797–20811. https://doi.org/10.1029/98ja01288.
Ruohoniemi, J.M., Greenwald, R.A., 2005. Dependencies of high-latitude plasma convection: consideration of interplanetary magnetic field, seasonal, and universal time factors in statistical patterns. J. Geophys. Res. Space Phys. 110 (A9), A09204. https://doi.org/10.1029/2004JA010815.
Russell, C.T., Elphic, R.C., 1979. ISEE observations of flux transfer events at the dayside magnetopause. Geophys. Res. Lett. 6 (1), 33–36. https://doi.org/10.1029/GL006i001p00033.
Sakai, J., Taguchi, S., Hosokawa, K., Ogawa, Y., 2013. Steep plasma depletion in dayside polar cap during a CME-driven magnetic storm. J. Geophys. Res. Space Phys. 118 (1), 462–471.
Sato, T., 1959. Morphology of ionospheric F2 disturbances in the polar regions. Rep. Ionos. Space Res. Jpn 13, 91–95.
Schunk, R.W., Nagy, A., 2000. Ionospheres: Physics, Plasma Physics, and Chemistry. Cambridge Atmospheric and Space Science Series, Cambridge University Press.
Schunk, R., Nagy, A., 2009. Ionospheres: Physics, Plasma Physics, and Chemistry. Cambridge University Press.
Schunk, R.W., Banks, P.M., Raitt, W.J., 1976. Effects of electric fields and other processes upon the night-time high-latitude F layer. J. Geophys. Res. Space Phys. 81 (19), 3271. https://doi.org/10.1029/JA081i019p03271.
Schunk, R.W., Demars, H.G., Sojka, J.J., 2005. Propagating polar wind jets. J. Atmos. Sol. Terr. Phys. 67 (4), 357–364. https://doi.org/10.1016/j.jastp.2004.09.005.

Semeter, J., Heinselman, C.J., Thayer, J.P., Doe, R.A., Frey, H.U., 2003. Ion upflow enhanced by drifting F-region plasma structure along the nightside polar cap boundary. Geophys. Res. Lett. 30 (22), 2139. https://doi.org/10.1029/2003GL017747.

Semeter, J., Mrak, S., Hirsch, M., Swoboda, J., Akbari, H., Starr, G., Hampton, D., Erickson, P., Lind, F., Coster, A., Pankratius, V., 2017. GPS signal corruption by the discrete aurora: precise measurements from the Mahali experiment. Geophys. Res. Lett. 44 (19), 9539–9546. https://doi.org/10.1002/2017GL073570.

Shiokawa, K., Katoh, Y., Satoh, M., Ejiri, M.K., Ogawa, T., 2000. Integrating-sphere calibration of all-sky cameras for nightglow measurements. Adv. Space Res. 26 (6), 1025–1028. https://doi.org/10.1016/S0273-1177(00)00052-1.

Shkarofsky, I.P., 1968. Generalized turbulence space-correlation and wave-number spectrum-function pairs. Can. J. Phys. 46, 2133. https://doi.org/10.1139/p68-562.

Siefring, C.L., Bernhardt, P.A., James, H.G., Parris, R.T., 2015. The CERTO beacon on CASSIOPE/e-POP and experiments using high-power HF ionospheric heaters. Space Sci. Rev. 189 (1–4), 107–122. https://doi.org/10.1007/s11214-014-0110-2.

Simon, A., 1963. Instability of a partially ionized plasma in crossed electric and magnetic fields. Phys. Fluids 6 (3), 382. https://doi.org/10.1063/1.1706743.

Singh, M., Rodriguez, P., Szuszczewicz, E.P., 1985. Spectral classification of medium-scale high-latitude F region plasma density irregularities. J. Geophys. Res. Space Phys. 90 (A7), 6525–6532. https://doi.org/10.1029/JA090iA07p06525.

Smith, D.R., Huang, C.Y., Dao, E., Pokhrel, S., Simpson, J.J., 2020. FDTD modeling of high-frequency waves through ionospheric plasma irregularities. J. Geophys. Res. Space Phys. 125 (3). https://doi.org/10.1029/2019JA027499. e2019JA027499.

Sofko, G.J., Greenwald, R., Bristow, W., 1995. Direct determination of large-scale magnetospheric field-aligned currents with SuperDARN. Geophys. Res. Lett. 22 (15), 2041–2044. https://doi.org/10.1029/95GL01317.

Sojka, J.J., Raitt, W.J., Schunk, R.W., 1981a. Plasma density features associated with strong convection in the winter high-latitude F region. J. Geophys. Res. Space Phys. 86 (A8), 6908–6916.

Sojka, J.J., Raitt, W.J., Schunk, R.W., 1981b. A theoretical study of the high-latitude winter F region at solar minimum for low magnetic activity. J. Geophys. Res. Space Phys. 86 (A2), 609–621.

Sojka, J.J., Bowline, M.D., Schunk, R.W., Decker, D.T., Valladares, C.E., Sheehan, R., Anderson, D.N., Heelis, R.A., 1993. Modeling polar cap F-region patches using time varying convection. Geophys. Res. Lett. 20 (17), 1783–1786. https://doi.org/10.1029/93GL01347.

Sojka, J.J., Bowline, M.D., Schunk, R.W., 1994. Patches in the polar ionosphere: UT and seasonal dependence. J. Geophys. Res. Space Phys. 99 (A8), 14959–14970.

Spicher, A., Miloch, W.J., Moen, J.I., 2014. Direct evidence of double-slope power spectra in the high-latitude ionospheric plasma. Geophys. Res. Lett. 41 (5), 1406–1412. https://doi.org/10.1002/2014GL059214.

Spicher, A., Cameron, T., Grono, E.M., Yakymenko, K.N., Buchert, S.C., Clausen, L.B.N., Knudsen, D. J., McWilliams, K.A., Moen, J.I., 2015a. Observation of polar cap patches and calculation of gradient drift instability growth times: a Swarm case study. Geophys. Res. Lett. 42 (2), 201–206. https://doi.org/10.1002/2014GL062590.

Spicher, A., Miloch, W.J., Clausen, L.B.N., Moen, J.I., 2015b. Plasma turbulence and coherent structures in the polar cap observed by the ICI-2 sounding rocket. J. Geophys. Res. Space Phys. 120 (12). https://doi.org/10.1002/2015JA021634. 10,959–10,978.

Spicher, A., Ilyasov, A.A., Miloch, W.J., Chernyshov, A.A., Clausen, L.B.N., Moen, J.I., Abe, T., Saito, Y., 2016. Reverse flow events and small-scale effects in the cusp ionosphere. J. Geophys. Res. Space Phys. 121 (10), 10466–10480. https://doi.org/10.1002/2016JA022999.

Spicher, A., Deshpande, K., Jin, Y., Oksavik, K., Zettergren, M.D., Clausen, L.B.N., Moen, J.I., Hairston, M.R., Baddeley, L., 2020. On the production of ionospheric irregularities via Kelvin-Helmholtz instability associated with cusp flow channels. J. Geophys. Res. Space Phys. 125 (6). https://doi.org/10.1029/2019JA027734. e2019JA027734.

Spiro, R.W., Heelis, R.A., Hanson, W.B., 1978. Ion convection and the formation of the mid-latitude F region ionization trough. J. Geophys. Res. Space Phys. 83 (A9), 4255–4264. https://doi.org/10.1029/JA083iA09p04255.

Spiro, R.W., Heelis, R.A., Hanson, W.B., 1979. Rapid subauroral ion drifts observed by atmosphere explorer C. Geophys. Res. Lett. 6 (8), 657–660. https://doi.org/10.1029/GL006i008p00657.

Spiro, R.W., Wolf, R.A., Fejer, B.G., 1988. Penetrating of high-latitude-electric-field effects to low latitudes during SUNDIAL 1984. Ann. Geophys. 6, 39–49.

Spogli, L., Alfonsi, L., de Franceschi, G., Romano, V., Aquino, M.H.O., Dodson, A., 2009. Climatology of GPS ionospheric scintillations over high and mid-latitude European regions. Ann. Geophys. 27, 3429–3437. https://doi.org/10.5194/angeo-27-3429-2009.

Spogli, L., Alfonsi, L., Cilliers, P.J., Correia, E., De Franceschi, G., Mitchell, C.N., Romano, V., Kinrade, J., Cabrera, M.A., 2013. GPS scintillations and total electron content climatology in the southern low, middle and high latitude regions. Ann. Geophys. 56 (2), R0220.

St.-Maurice, J.-P., Hanson, W.B., 1982. Ion frictional heating at high latitudes and its possible use for an in situ determination of neutral thermospheric winds and temperatures. J. Geophys. Res. Space Phys. 87 (A9), 7580–7602. https://doi.org/10.1029/JA087iA09p07580.

St.-Maurice, J.-P.-P., Torr, D.G.G., 1978. Nonthermal rate coefficients in the ionosphere: the reactions of O+ With N2, O2, and NO. J. Geophys. Res. Space Phys. 83 (7), 969–977. https://doi.org/10.1029/JA083iA03p00969.

Störmer, C., 1955. The Polar Aurora. Oxford University Press.

Theurer, T.E., 2012. Ray Tracing Applications for High-Frequency Radar: Characterizing Artificial Layers and Background Density Perturbations in the Ionosphere (Master's thesis). University of Alaska Fairbanks.

Thomas, E.G., Baker, J.B.H., Ruohoniemi, J.M., Clausen, L.B.N., Coster, A.J., Foster, J.C., Erickson, P.J., 2013. Direct observations of the role of convection electric field in the formation of a polar tongue of ionization from storm enhanced density. J. Geophys. Res. Space Phys. 118 (3), 1180–1189.

Tsunoda, R.T., 1988. High-latitude F region irregularities: a review and synthesis. Rev. Geophys. 26 (4), 719–760. https://doi.org/10.1029/RG026i004p00719.

Valladares, C.E., Carlson Jr, H.C., 1991. The electrodynamic, thermal, and energetic character of intense Sun-aligned arcs in the polar cap. J. Geophys. Res. Space Phys. 96 (A2), 1379–1400. https://doi.org/10.1029/90JA01765.

van der Meeren, C., Oksavik, K., Lorentzen, D., Moen, J.I., Romano, V., 2014. GPS scintillation and irregularities at the front of an ionization tongue in the nightside polar ionosphere. J. Geophys. Res. Space Phys. 119 (10), 8624–8636. https://doi.org/10.1002/2014JA020114.

van der Meeren, C., Oksavik, K., Lorentzen, D.A., Rietveld, M.T., Clausen, L.B.N., 2015. Severe and localized GNSS scintillation at the poleward edge of the nightside auroral oval during intense substorm aurora. J. Geophys. Res. Space Phys. 120 (12), 10607–10621. https://doi.org/10.1002/2015JA021819.

van der Meeren, C., Oksavik, K., Lorentzen, D.A., Paxton, L.J., Clausen, L.B.N., 2016. Scintillation and irregularities from the nightside part of a Sun-aligned polar cap arc. J. Geophys. Res. Space Phys. 121 (6), 5723–5736. https://doi.org/10.1002/2016JA022708.

Vickrey, J.F., Kelley, M.C., 1982. The effects of a conducting E layer on classical F region cross-field plasma diffusion. J. Geophys. Res. Space Phys. 87 (A6), 4461–4468.

Vickrey, J.F., Rino, C.L., Potemra, T.A., 1980. Chatanika/Triad observations of unstable ionization enhancements in the auroral F-region. Geophys. Res. Lett. 7 (10), 789–792. https://doi.org/10.1029/GL007i010p00789.

Villain, J.P., Hanuise, C., Beghin, C., 1986. ARCAD3-SAFARI coordinated study of auroral and polar F-region ionospheric irregularities. Ann. Geophys. 4, 61–68.

Voiculescu, M., Roth, M., 2008. Eastward sub-auroral ion drifts or ASAID. Ann. Geophys. 26 (7), 1955–1963. https://doi.org/10.5194/angeo-26-1955-2008.

Voiculescu, M., Virtanen, I., Nygrén, T., 2006. The F-region trough: seasonal morphology and relation to interplanetary magnetic field. Ann. Geophys. 24 (1), 173–185. https://doi.org/10.5194/angeo-24-173-2006.

Voiculescu, M., Nygrén, T., Aikio, A., Kuula, R., 2010. An olden but golden EISCAT observation of a quiet-time ionospheric trough. J. Geophys. Res. Space Phys. 115 (A10), A10315. https://doi.org/10.1029/2010JA015557.

Copernicus GmbH Walker, I., Moen, J., Kersley, L., Lorentzen, D., 1999. On the possible role of cusp/cleft precipitation in the formation of polar-cap patches. Ann. Geophys. 17 (10), 1298–1305. https://doi.org/10.1007/s00585-999-1298-4.

Walsh, B.M., Foster, J.C., Erickson, P.J., Sibeck, D.G., 2014. Simultaneous ground- and space-based observations of the plasmaspheric plume and reconnection. Science 343 (6175), 1122–1125. https://doi.org/10.1126/science.1247212.

Wang, H., Ridley, A.J., Lühr, H., Liemohn, M.W., Ma, S.Y., 2008. Statistical study of the subauroral polarization stream: its dependence on the cross-polar cap potential and subauroral conductance. J. Geophys. Res. Space Phys. 113 (A12), A12311.

Wang, H., Lühr, H., Häusler, K., Ritter, P., 2011. Effect of subauroral polarization streams on the thermosphere: a statistical study. J. Geophys. Res. Space Phys. 116 (A3), 5785.

Wang, W., Talaat, E.R., Burns, A.G., Emery, B., Hsieh, S.Y., Lei, J., Xu, J., 2012. Thermosphere and ionosphere response to subauroral polarization streams (SAPS): model simulations. J. Geophys. Res. Space Phys. 117 (A7), A07301.

Wang, Y., Zhang, Q.-H., Jayachandran, P.T., Lockwood, M., Zhang, S.-R., Moen, J., Xing, Z.-Y., Ma, Y.-Z., Lester, M., 2016. A comparison between large-scale irregularities and scintillations in the polar ionosphere. Geophys. Res. Lett. 43 (10), 4790–4798. https://doi.org/10.1002/2016GL069230.

Wang, Y., Zhang, Q.-H., Jayachandran, P.T., Moen, J., Xing, Z.-Y., Chadwick, R., Ma, Y.-Z., Ruohoniemi, J.M., Lester, M., 2018. Experimental evidence on the dependence of the standard GPS phase scintillation index on the ionospheric plasma drift around noon sector of the polar ionosphere. J. Geophys. Res. Space Phys. 123 (3), 2370–2378. https://doi.org/10.1002/2017JA024805.

Warrington, E.M., Rogers, N.C., Jones, T.B., 1997. Large HF bearing errors for propagation paths contained within the polar cap. IEE Proc. Microwaves Antenn. Propag. 144 (4), 241–249. https://doi.org/10.1049/ip-map:19971187.

Watson, C., Jayachandran, P.T., Macdougall, J.W., 2016. Characteristics of GPS TEC variations in the polar cap ionosphere. J. Geophys. Res. A Space Phys. 121, 4748–4768. https://doi.org/10.1002/2015JA022275.Received.

Weber, E.J., Buchau, J., Moore, J., Sharber, J., Livingston, R., Winningham, J.D., Reinisch, B., 1984. F layer ionization patches in the polar cap. J. Geophys. Res. Space Phys. 89 (A3), 1683–1694. https://doi.org/10.1029/JA089iA03p01683.

Weber, E.J., Buchau, J., Moore, J.G., Sharber, J.R., Livingston, R.C., Winningham, J.D., Reinisch, B.W., 1984. F layer ionization patches in the polar cap. J. Geophys. Res. Space Phys. 89 (A3), 1683–1694.

Weiss, L.A., Weber, E.J., Reiff, P.H., Sharber, J.R., Winningham, J.D., Primdahl, F., Mikkelsen, I.S., Seifring, C., Wescott, E.M., 1993. Convection and electrodynamic signatures in the vicinity of a sun-aligned arc: results from the polar acceleration regions and convection study (Polar ARCS). In: Lysak, R.L. (Ed.), Aurora1 Plasma Dynamics. Geophys. Monog., vol. 80. American Geophysical Union (AGU), p. 69.

Werner, S., Prölss, G.W., 1997. The position of the ionospheric trough as a function of local time and magnetic activity. Adv. Space Res. 20 (9), 1717–1722. https://doi.org/10.1016/S0273-1177(97)00578-4.

Wernik, A.W., Gola, M., Liu, C.H., Franke, S.J., 1990. High-latitude irregularity spectra deduced from scintillation measurements. Radio Sci. 25, 883–895. https://doi.org/10.1029/RS025i005p00883.

Wernik, A.W., Secan, J.A., Fremouw, E.J., 2003. Ionospheric irregularities and scintillation. Adv. Space Res. 31, 971–981. https://doi.org/10.1016/S0273-1177(02)00795-0.

Whalen, J.A., 1989. The daytime F layer trough and its relation to ionospheric-magnetospheric convection. J. Geophys. Res. Space Phys. 94 (A12), 17169–17184. https://doi.org/10.1029/JA094iA12p17169.

Wickwar, V.B., Cogger, L.L., Carlson, H.C., 1974. The 6300 ÅO1D airglow and dissociative recombination. Planet. Space Sci. 22 (5), 709–724. https://doi.org/10.1016/0032-0633(74)90141-X.

Yang, N., Le, H., Liu, L., 2015. Statistical analysis of ionospheric mid-latitude trough over the Northern Hemisphere derived from GPS total electron content data. Earth Planets Space 67, 196. https://doi.org/10.1186/s40623-015-0365-1.

Yeh, K.C., Liu, C.-H., 1982. Radio wave scintillations in the ionosphere. IEEE Proc. 70, 324–360.

Yeh, H.-C., Foster, J.C., Rich, F.J., Swider, W., 1991. Storm time electric field penetration observed at mid-latitude. J. Geophys. Res. Space Phys. 96 (A4), 5707–5721.

Yizengaw, E., Moldwin, M., 2005. The altitude extension of the mid-latitude trough and its correlation with plasmapause position. Geophys. Res. Lett. 32 (9), L09105. https://doi.org/10.1029/2005GL022854.
Yizengaw, E., Moldwin, M.B., Galvan, D.A., 2006. Ionospheric signatures of a plasmaspheric plume over Europe. Geophys. Res. Lett. 33 (17), L17103. https://doi.org/10.1029/2006GL026597.
Yokoyama, T., 2017. A review on the numerical simulation of equatorial plasma bubbles toward scintillation evaluation and forecasting. Prog. Earth Planet. Sci. 4 (1), 37. https://doi.org/10.1186/s40645-017-0153-6.
Zabusky, N.J., Doles III, J.H., Perkins, F.W., 1973. Deformation and striation of plasma clouds in the ionosphere: 2. Numerical simulation of a nonlinear two-dimensional model. J. Geophys. Res. Space Phys. 78 (4), 711–724.
Zettergren, M.D., Hirsch, M., 2020. gemini3d/gemini-examples., https://doi.org/10.5281/zenodo.3992594.
Zettergren, M., Semeter, J., 2012. Ionospheric plasma transport and loss in auroral downward current regions. J. Geophys. Res. Space Phys. 117 (A6), A06306. https://doi.org/10.1029/2012JA017637.
Zettergren, M.D., Snively, J.B., 2015. Ionospheric response to infrasonic-acoustic waves generated by natural hazard events. J. Geophys. Res. Space Phys. 120 (9), 8002–8024.
Zettergren, M.D., Semeter, J.L., Dahlgren, H., 2015. Dynamics of density cavities generated by frictional heating: formation, distortion, and instability. Geophys. Res. Lett. 42 (23), 10–120.
Zhang, Y., Paxton, L.J., 2015. Auroral Dynamics and Space Weather, Geophysical Monograph Series, vol. 215. In: American Geophysical Union (AGU). Washington, DC. https://doi.org/10.1002/9781118978719.
Zhang, Q.-H., Zhang, B.-C., Lockwood, M., Hu, H.-Q., Moen, J., Ruohoniemi, J.M., Thomas, E.G., Zhang, S.-R., Yang, H.-G., Liu, R.-Y., McWilliams, K.A., Baker, J.B.H., 2013. Direct observations of the evolution of polar cap ionization patches. Science 339 (6127), 1597–1600. https://doi.org/10.1126/science.1231487.
Zhang, Q.H., Lockwood, M., Foster, J.C., Zhang, S.-R., Zhang, B.C., McCrea, I.W., Moen, J., Lester, M., Ruohoniemi, J.M., 2015a. Direct observations of the full Dungey convection cycle in the polar ionosphere for southward interplanetary magnetic field conditions. J. Geophys. Res. Space Phys. 120 (6), 4519–4530.
Zhang, Q.-H., Zong, Q.-G., Lockwood, M., Heelis, R.A., Hairston, M., Liang, J., McCrea, I., Zhang, B.-C., Moen, J., Zhang, S.-R., Zhang, Y.-L., Ruohoniemi, J.M., Lester, M., Thomas, E.G., Liu, R.-Y., Dunlop, M.W., Liu, Y.C.-M., Ma, Y.-Z., 2016. Earth's ion upflow associated with polar cap patches: global and in situ observations. Geophys. Res. Lett. 43 (5), 1845–1853. https://doi.org/10.1002/2016GL067897.
Zhang, Q.-H., Ma, Y.-Z., Jayachandran, P.T., Moen, J., Lockwood, M., Zhang, Y.-L., Foster, J.C., Zhang, S.-R., Wang, Y., Themens, D.R., et al., 2017a. Polar cap hot patches: Enhanced density structures different from the classical patches in the ionosphere. Geophys. Res. Lett. 44 (16), 8159–8167. https://doi.org/10.1002/2017GL073439.
Zhang, S.-R., Erickson, P.J., Foster, J.C., Holt, J.M., Coster, A.J., Makela, J.J., Noto, J., Meriwether, J.W., Harding, B.J., Riccobono, J., Kerr, R.B., 2015b. Thermospheric poleward wind surge at midlatitudes during great storm intervals. Geophys. Res. Lett. 42 (13), 5132–5140.
Zhang, S.-R., Erickson, P.J., Zhang, Y., Wang, W., Huang, C., Coster, A.J., Holt, J.M., Foster, J.F., Sulzer, M., Kerr, R., 2017. Observations of ion-neutral coupling associated with strong electrodynamic disturbances during the 2015 St. Patrick's Day storm. J. Geophys. Res. Space Phys. 122 (1), 1314–1337. https://doi.org/10.1002/2016JA023307.
Zhu, L., Shunk, R.W., Sojka, J.J., 1997. Polar cap arcs: a review. J. Atmos. Sol. Terr. Phys. 59 (10), 1087–1126.
Zou, S., Moldwin, M., Coster, A., Lyons, L., Nicolls, M., 2011. GPS TEC observations of dynamics of the mid-latitude trough during substorms. Geophys. Res. Lett. 38 (14), L14109. https://doi.org/10.1029/2011GL048178.
Zou, S., Moldwin, M.B., Ridley, A.J., Nicolls, M.J., Coster, A.J., Thomas, E.G., Ruohoniemi, J.M., 2014. On the generation/decay of the storm-enhanced density plumes: role of the convection flow and field-aligned ion flow. J. Geophys. Res. Space Phys. 119 (10), 8543–8559. https://doi.org/10.1002/2014JA020408.

Further reading

Mailyan, B., Shi, Q.Q., Kullen, A., Maggiolo, R., Zhang, Y., Fear, R.C., Zong, Q.-G., Fu, S.Y., Gou, X. C., Cao, X., Yao, Z.H., Sun, W.J., Wei, Y., Pu, Z.Y., 2015. Transpolar arc observation after solar wind entry into the high-latitude magnetosphere. J. Geophys. Res. Space Phys. 120 (5), 3525–3534. https://doi.org/10.1002/2014JA020912.